

**Structural Study of the Ventral Disc of *Giardia*
*lamblia***

by

Joanna Ruth Brown

Hons. B.Sc., University of Edinburgh, 2005

M.Sc., University of Strathclyde, 2007

A thesis submitted to the Faculty of the Department of Chemistry and Biochemistry of the University
of Colorado in partial fulfillment of the requirement for the degree of

Doctor of Philosophy

Department of Chemistry and Biochemistry

2014

This thesis entitled:

Structural Study of the Ventral Disc of *Giardia lamblia*

written by Joanna Ruth Brown

has been approved for the Department of Chemistry and Biochemistry by

Professor Andreas Hoenger, Ph.D, Thesis Advisor and Committee Chair

Associate Professor Dylan Taatjes, Ph.D.,

Date:

The final copy of this thesis has been examined by the signatories, and we find that both the content and the form meet the acceptable presentation standards of scholarly work in the above mentioned discipline.

Brown, Joanna Ruth (Ph.D., Chemistry and Biochemistry)

Structural Study of the Ventral Disc of *Giardia lamblia*

Thesis directed by Professor Andreas Hoenger

ABSTRACT

Giardia lamblia is single celled eukaryotic parasite. It infects humans, and is one of the most common parasitic infections contracted in the USA. Attachment to the host's intestinal epithelium is essential to the feeding form of *Giardia*, the trophozoite. Central to attachment is the microtubule cytoskeleton, the principle structure of which is the ventral disc. The ventral disc is a large array of highly decorated microtubules that forms a domed right-handed spiral. The use of large area montages of multiple tomograms of negatively stained, extracted, ventral discs has provided information on the exact path of each microtubule in the array. This study has provided new information on the total number, length and organization of MTs within this large structure. It was also discovered that the ventral disc is composed of six structurally distinct regions, which vary in terms of microtubule spacing, microtubule curvature, microribbon height, and crossbridge length and morphology. The microtubules of the ventral disc are continuous and pass through multiple regions along their length. The protein decoration along a single microtubule can undergo multiple structural transitions and rearrangements. Cryo-electron tomography and subvolume averaging were used to obtain 3D density maps from four of the newly identified ventral disc regions.

These experiments revealed the presence of smaller protein densities present in all four regions of the ventral disc. These densities are located on both the outside and inside surface of the MT and were found to localize to specific protofilaments. The arrangement and size of these densities was found to vary both within and between the ventral disc regions. One density located on the inner surface of the microtubule, known as *Giardia* microtubule inner protein 5 (GMIP5), did not vary within or between the regions. It was found that this density occurred at every 8nm repeat along the microtubules and was approximately the size of a tubulin monomer. This structural information obtained was used to narrow the list of possible protein components of GMIP5 from seventeen proteins to only six. These six proteins include: alpha-2 annexin, alpha-3 annexin, alpha-5 annexin, alpha-17 annexin, DAP5374 and DAP13766.

DEDICATION

I would like to dedicate this work to my wonderful husband, Dr. Peter Brown.

ACKNOWLEDGEMENTS

I would like to thank and acknowledge the dedicated women who work in the Boulder Lab for 3D EM of Cells. Their efforts are enormous and often under-recognized. I would like to thank Mary Morphew for help and advice with sample preparation. More than this, I would like to thank Mary for her off-beat and honest sense of humor and fun. I admire her strength of character and endurance. Dr. Eileen O'Toole is one of the nicest people I have ever met. I would like to thank her for her words of encouragement when times were tough for me. I also appreciate her patience and the time she took away from her own work to teach me. Thanks to Eileen for all her honesty and understanding. Thanks to Cynthia Paige for her unique perspective and sense of optimism and her willingness to help in any situation.

Above all others, I would like to sincerely thank Cindi Schwartz. She was my partner in all *Giardia* related "crime". I think that together we have accomplished much more than we could have alone. Cindi taught me almost everything I know about electron microscopy, from sample preparation to image processing. She offered me her time, help, advice and best of all, friendship. I could not have completed my PhD without her, and, I owe her more thanks than I can put into words.

Of course, I also have to sincerely thank Dr. David Mastronarde and John Heumann. David, who took time out of his very busy schedule to add functionality to IMOD that was essential to my research. His work is exemplary and is appreciated, not only by me, but by a large community of users world-wide. John was essential to the completion of all

the sub-volume averaging work. He worked hard to create new aspects of PEET to help interpret and analyze our data. I would also like to thank him for taking the time to explain a lot of the mathematical aspects to me. He was very patient with me and taught me the basics of linux, which was a life-saver!

I would like to thank my parents, Patricia and William, for their support when times were tough for me in graduate school. They have encouraged me and believed in me since I was a child and I hope I have made them proud. Special thanks to mum, who read through this work with the eagle eye of an English teacher, and braved the scientific jargon!

I must also put in an acknowledgement fellow graduate students and friends. Thanks to Jon Langberg for listening to my grad school woes. Thanks to Zach Poss, Jen Gifford and Tina Zhao for fun and support during first year and beyond. A big thank you to Cami Poss for being a great friend with such a kind heart.

Last, but definitely not least, I have to thank my husband Dr. Peter Brown. He is my rock. He's put up with me when I was frustrated with work, and loved me even when I was grumpy. He has offered his support and advice since his arrival in Colorado. He has offered me help with all aspects of grad school and has shared his extensive scientific knowledge and expertise whenever possible. He took time out of his schedule to help me extensively with various pieces of written work (poor Pete!). With his help, I've become a much better writer, hopefully making the proof reading of this thesis less agonizing for

those who had to check it over. Thanks and lots of love to you, Petey!

ABBREVIATIONS LIST

1. Microtubule - MT
2. Megabases - MB
3. Microribbon - MR
4. Electron microscopy - EM
5. Cryo-electron microscopy - cryo-EM
6. Electron tomography - ET
7. Protofilament - PF
8. Microtubule associated protein - MAP
9. Disc associated protein - DAP
10. Median body protein - MBP
11. Enhanced green fluorescent protein - EGFP
12. Microtubule inner protein - MIP
13. Contrast transfer function - CTF
14. Dense Band - DB
15. Field Emission Gun - FEG
16. Energy filtered transmission electron microscopy - EFTEM
17. Overlap Zone - OZ
18. Dense bands nucleation zone - DNZ
19. Dorsal overlap zone - DOZ
20. Ventral groove - VG
21. Ventral overlap zone - VOZ

22. Dimethyl sulphoxide - DMSO

23. Liquid nitrogen - LN₂

24. Wild-type – WT

TABLE OF CONTENTS

CHAPTER 1: Introduction to <i>Giardia lamblia</i>	1
Discovery of <i>Giardia lamblia</i>	1
Disease and epidemiology	2
Giardiasis	2
Occurrence in the USA	3
Occurance world-wide	3
Drug Treatment and Resistance	5
Taxonomy and Evolutionary Significance	6
<i>Giardia</i> species	9
The Genetics of <i>Giardia</i>	10
Sequencing of the genome of <i>Giardia lamblia</i>	10
The nuclei	11
The Life-Cycle of <i>Giardia</i>	11
Cysts and Infection	11
Excystation	13
The Trophozoite Cell	13
Encystation	15
The Microtubule Cytoskeleton	15
The Four Pairs of Flagella	15
The Anterior Flagella	16
The Posterior-lateral Flagella	16
The Ventral Flagella	17
The Caudal Flagella and Funis	17
The Median Body	18
The Ventral Disc	18
Advances in Knowledge of Ventral Disc Structure	19
Microtubule polarity and the locations and structures of microtubule ends	19
Discovery of GMIPs and GMAPs	20
Attachment to the Host	24
Attachment force	24

Proposed Mechanisms of Attachment	25
Hydrodynamic model	25
The Suction-cup model	27
The Ventral Disc and Trophozoite Replication	28
Protein Composition of the Ventral Disc	29
Discovery of new disc associated proteins	29
Regions of the Ventral Disc	31
Median Body Protein	32
CHAPTER 2: Introduction to Modern Electron Microscopy and	
Image Processing	35
Advances in Microscope and Detector Technology	35
Beam generation from the FEG tip	35
Energy filtering reduces noise	37
CCD detectors allow real-time image collection and digitization	37
Fucture of EM with direct electron cameras	38
Electron Tomography	38
A tilt series of projection images	39
3-D reconstruction	41
Maintaining correct handedness	43
Montaging Allows Large Area Imaging at Higher Resolution	44
Acquiring a Montage	44
Reconstruction of a montage of tomograms	44
Cryo-Electron Tomography	45
Sample preparation for cryo-electron microscopy	45
Limitations of cryo-electron microscopy	46
Contrast Transfer Function Correction	49
Subvolume Averaging	51
Limitations of Subvolume Averaging	52
CHAPTER 3: Architecture and Organization of the Ventral Disc Array	56

Introduction	56
Brief Materials and Methods	60
Advantages and Limitations of Extraction of the Cytoskeletons and Preparation by Negative Stain	60
Results	62
Supernumerary Microtubules	62
The Architecture and Organization of the Main Body of the Ventral Disc	65
Large Scale Architecture of the Ventral Disc MTs	65
Structural features of the ventral disc: the overlap zone	67
Structural features of the ventral disc: the ventral groove	68
Structural features of the ventral disc: the disc margin	68
Number, Length and Organization of MTs within the Ventral Disc Array	69
The Organization, Localization and Morphology of MT Minus- and Plus-ends in the Ventral Disc	72
Nucleation sites relate to the location of termination	74
Summary of Results and Discussion	75
CHAPTER 4: Regions of the Ventral Disc	77
Introduction	77
Results	78
Location of the Regions	79
Characteristic Regional Spacing and Morphology	81
Dense Bands Nucleation Zone	83
Dorsal Overlap Zone	83
Disc Body	84
Ventral Groove	84
Ventral Overlap Zone	85
Margin	86
Patterns of MT curvature within the Ventral Disc	86
Curvature across the ventral disc array	88
Description of the Curvature Profiles of Each Ventral Disc Region	92

Highly Curved MTs in the dorsal overlap zone (Figure 4.6)	92
Curvature in the disc body (Figure 4.7)	93
Curvature of the ventral groove MTs (Figure 4.8)	95
Curvature in the ventral overlap zone (Figure 4.9)	97
Curvature in the margin (Figure 4.10)	98
Regional Transition Along Individual MTs	100
Results Summary and Discussion	101
CHAPTER 5: Structures of the Regional Repeating Units of the Ventral Disc	106
Introduction	106
Results	108
MT spacing and curvature	111
MR height	111
Crossbridge length and morphology	111
Side arms	112
Subvolume Averaging of the Dorsal and Ventral Overlap Zone	112
Subvolume Averaging Specifications	113
Comparison and the Repeating Unit Structures of the Dorsal Overlap Zone and the Ventral Overlap Zone	122
The Microribbons	122
The Crossbridges	122
The Side Arms	123
The Paddle	125
Intra-region variation	125
GMAPs	126
GMIPs	127
Summary of Observed Differences in the Decorating Densities	128
Identification of the Core Repeating Unit of the Ventral Disc	130
Structural features in the common core repeating unit	131
Results Summary and Discussion	136

GMIP5	139
CHAPTER 6: Final Conclusions and Discussion	142
If I had another five years... ideas for further research	144
Construction of curvature class averages	144
Investigation of the MBP Morpholino phenotype	145
Investigating GMIP5 candidate proteins	146
CHAPTER 7: Materials and Methods	148
Culture of WBC6-M <i>Giardia lamblia</i> trophozoite cells	148
Modified TY-S-33 media	148
Culture of trophozoite cells	149
Freezing and storage of trophozoite cells	150
Preparation of extracted cytoskeletons	150
PIPES, HEPES, EGTA, MgSO ₄ (PHEM) buffer	150
Detergent extraction of cytoskeletons	150
Preparation of grids for negative stain of extracted cytoskeletons	151
Preparation of carbon coated formvar grids	151
Preparing negative stained extracted cytoskeletons	152
Preparation of plunge frozen grids of extracted cytoskeletons	153
Imaging in the TEM	154
Acquisition of a 4x4 montage	154
Acquisition of a single axis cryo tomogram	155
Reconstructions of Tomograms using IMOD	156
Building a 4x4 montaged tomogram	156
Building a cryo tomogram	157
CTF correction	157
Erasing gold	158
Modeling using IMOD	158
Modeling the ventral disc	158

Modeling for subvolume averaging	159
Subvolume averaging using PEET	160
Generation of a preliminary averaged volume for each overlap zone surface in each tomogram	160
Production of a grand average volume from the overlap zone from multiple tomograms	161
Calculating the internal resolution of the grand average volumes using Fourier shell correlation	164
Production of the Binary Common Core Structure	164
REFERENCES	165

LIST OF FIGURES

CHAPTER 1

Figure 1.1: Rates of <i>Giardia lamblia</i> infection across the USA by state in 2008	4
Figure 1.2: Phylogenetic tree showing the position of <i>Giardia lamblia</i> relative to other organisms	8
Figure 1.3: Life-cycle of <i>Giardia lamblia</i>	12
Figure 1.4: Morphology of <i>Giardia lamblia</i> trophozoite	14
Figure 1.5: Morphology of minus-ends in the ventral disc	21
Figure 1.6: High resolution isosurface representation of the structure of the repeating unit of the ventral disc	23
Figure 1.7: The Hydrodynamic model of attachment	26
Figure 1.8: Stages of trophozoite attachment	28
Figure 1.9: Classification of DAPs discovered by the Dawson Lab	32
Figure 1.10: Morphology of ventral disc in cells treated to reduce expression of MBP	34

CHAPTER 2

Figure 2.1: Schematic diagram of the modern electron microscope	36
Figure 2.2: Tomographic reconstruction of the tilt series data containing a missing wedge	41
Figure 2.3: Types of electron scattering that result from the interaction of the beam electrons with the atoms of the specimen	48
Figure 2.4: Images of carbon film collected using different defocus values	50

CHAPTER 3

Figure 3.1: Extracted ventral disc of a <i>Giardia lamblia</i> trophozoite	58
Figure 3.2: Extracted ventral disc of a <i>Giardia lamblia</i> trophozoite	59

Figure 3.3: Location and organization of the snMTs	63
Figure 3.4: Architecture of the ventral disc	66
Figure 3.5: A closer look at the location and morphology of the nucleation sites of the ventral disc MTs	73

CHAPTER 4

Figure 4.1: Regions of the ventral disc	80
Figure 4.2: 24 nm tomographic slice from six ventral disc regions and the power spectra from those regions showing the repeating structures in reciprocal space	82
Figure 4.3: The method by which curvature of the ventral disc MTs were determined	87
Figure 4.4: MT curvature at different regions of the ventral disc represented in a heat map	88
Figure 4.5: Variations in curvature along individual MTs	91
Figure 4.6: Histogram of curvature values of the DOZ	92
Figure 4.7: Histogram of curvature values of the dense bands	94
Figure 4.8: Histogram of curvature values of the ventral groove	96
Figure 4.9: Histogram of curvature values of the VOZ	97
Figure 4.10: Histogram of curvature values in the Margin	99
Figure 4.11: Regional transitions of the ventral disc MTs	100

CHAPTER 5

Figure 5.1: Tomographic slices from cryo-ET data of the overlap zone	109
Figure 5.2: 3-D density map of the DOZ produced by subvolume averaging	115
Figure 5.3: 3-D density map of the VOZ produced by subvolume averaging	117
Figure 5.4: Isosurface representation of the DOZ repeating unit structure in crosssection	120
Figure 5.5: Isosurface representation of the VOZ repeating unit structure in	

crosssection	121
Figure 5.6: Binary 3-D density map of the common core structure of the ventral disc	133

CHAPTER 7

Figure 7.1: PEET setup tab used for the grand average run for each region	162
Figure 7.2: PEET run tab used for the grand average run for each region	163

LIST OF TABLES

CHAPTER 3

Table 3.1: A summary of the key results from Chapter 4 and how they relate to the current literature on the ventral disc structure	76
---	----

CHAPTER 4

Table 4.1: Kappa values, their corresponding color in the heat map (Figure 4.4) and description of curvature	89
Table 4.2: Structural and organizational characteristics used to define each ventral disc region	102
Table 4.3: Organization of the DAPs based on their GFP localization patterns to regions of the ventral disc	104

CHAPTER 5

Table 5.1: Summary of the structural differences that exist between the DOZ, disc body, VOZ and margin	129
Table 5.2: Using structural information to narrow down the GMIP5 candidate proteins	141

CHAPTER 1: INTRODUCTION TO *GIARDIA LAMBLIA*

Discovery of *Giardia lamblia*

Giardia lamblia was first discovered in 1681 by Anton van Leeuwenhoek [1,2]. He is believed to have observed trophozoite cells swimming in a sample of his own stool. He famously described the cells as “very prettily moving animalcules, some rather larger, others somewhat smaller than a blood corpuscle and all of one and the same structure...their bodies were somewhat longer than broad and their belly, which was flatlike, furnished with sundry little paws...” [3,4]. Initially, the pathogenicity of *Giardia* was not fully recognized, though van Leeuwenhoek suspected that the organisms he had observed might be related to recurring bouts of diarrhea he was reported to be experiencing.

In 1859, Vilem Lambl, after whom one of the *Giardia* species is named, rediscovered and documented the morphology of the trophozoite cells he found in the stool sample of pediatric patients he was overseeing in Prague [5].

Disease and epidemiology

Giardiasis

The excysted trophozoite form of *Giardia* will cause giardiasis in approximately one third of infected hosts. Symptoms usually manifest one to three weeks after initial ingestion of the cysts [6]. Although not fatal, the symptoms are unpleasant and can persist for 6 weeks or longer if not treated. Symptoms of giardiasis include: diarrhea, dehydration hematuria, stomach cramps, vomiting, bloating, excessive gas, sulphurous ructus and a feeling of general malaise [7]. As well as experiencing these symptoms, infected individuals may encounter problems with nutrient uptake, resulting in weight loss. Lactose malabsorption [8], reduced carbohydrate absorption [9,10], vitamin A deficiency [11], and B12 deficiency [11,12,13] have all been observed in infected individuals, particularly children. It is also thought that parasitic protozoa, including *G. lamblia*, may play a significant role in irritable bowel syndrome [14].

A positive diagnoses of *Giardia* infection involves the discovery of trophozoite cells or ovoid cysts in the feces of an infected individual. These markers can often be difficult to find and identify [15], though, infection can be confirmed with an ELISA test that is now widely available [16]. In addition to uncomfortable symptoms that can persist for extended periods [17], treated and untreated individuals can fail to eliminate the infection, with 10% [18] to 40 % [6] of treated individuals remaining infected after a course of treatment. Approximately 20 to 25 % [6] of hosts will become asymptomatic carriers who are infected and colonized by trophozoites. While failing to exhibit the

classic symptoms of giardiasis, these carriers continue to shed cysts into the environment that can infect other individuals. A single infected host can shed up to 10 billion cysts daily [19]. Asymptomatic carriers can experience a recurrence of giardiasis symptoms and a flare up of infection at a later date [7].

Occurrence in the USA

Giardia is the most common intestinal parasitic disease contracted in the USA [20]. It is found in all areas of the country (Figure 1.1), though the exact number of cases is not precisely known. *Giardia* infections are thought to be regularly unreported to a physician, and sometimes misdiagnosed.

Giardiasis is common in the Rocky Mountain region, including the state of Colorado, where it is colloquially known as “Beaver Fever”. Hikers, and other people enjoying the outdoors, can become infected with *Giardia* by ingesting water contaminated with animal feces and cysts. The cysts often originate from zoonotic reservoirs, such as beavers. Cysts are insensitive to regularly used water purification treatments such as chlorination, iodation and UV radiation. They can be filtered from water if material with a small enough pore size is selected and can be inactivated by heating the water to 100 °C [6].

Occurrence world-wide

As in the USA, the data on global rates of infection with *Giardia* is not comprehensive. *Giardia* seems to be ubiquitous in the human population and infections occur worldwide. It is estimated that 33% of the population of developed nations have contracted giardiasis

at some point in their lives [21]. Infection rates are notably high in Eastern Europe and parts of Russia, but infection has been reported in travelers to India, Africa and the Middle East [6].

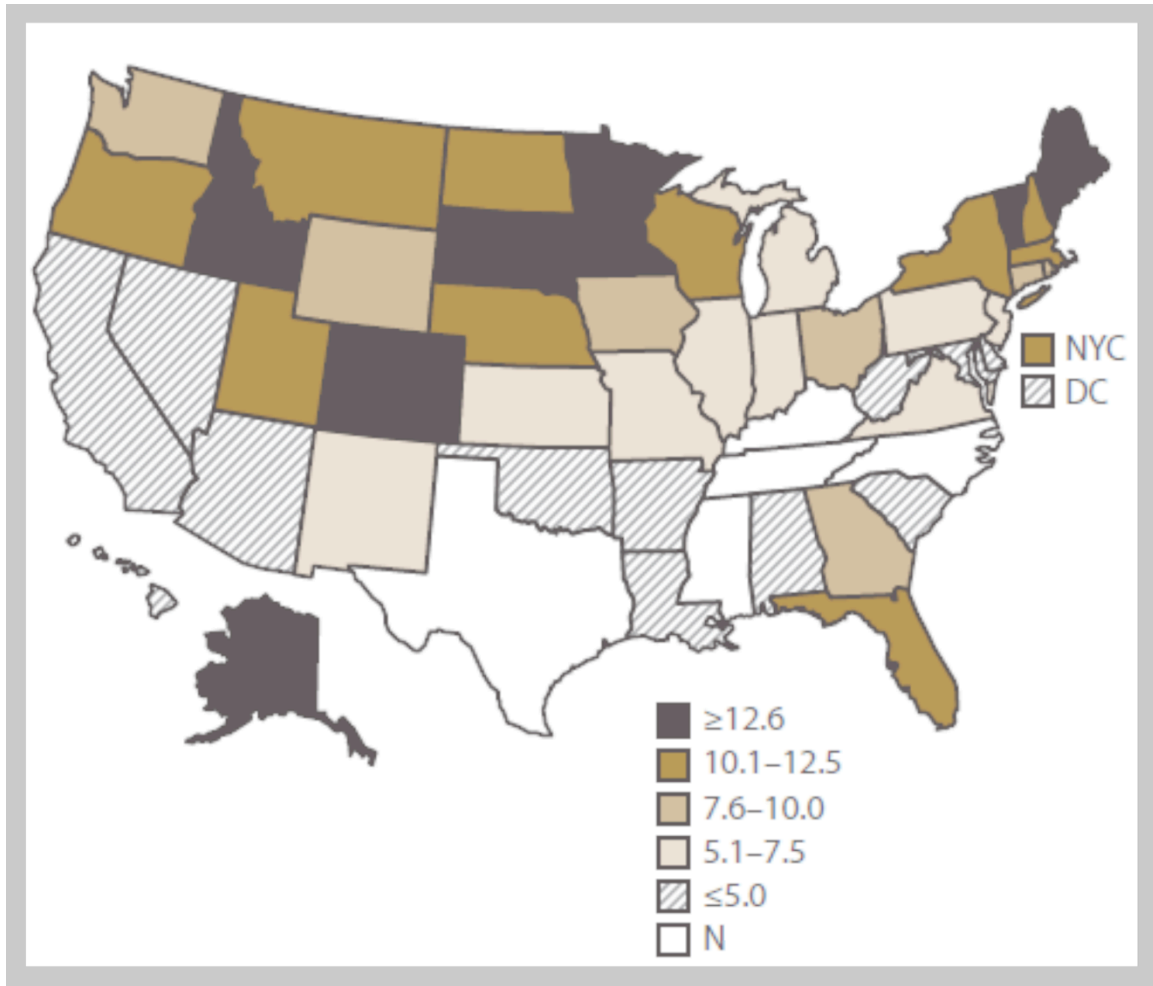


Figure 1.1: Rates of *Giardia lamblia* infection across the USA by state in 2008. Adapted from the CDC website. The numbers in the key represent the number of cases per 100,000 people. N = not a reported disease in that state.

Giardia infection is especially prevalent in areas where water treatment and sanitation standards are poor [6,22]. In developing nations almost 2% of the adult population and 6-8% of children in developing nations are constantly infected at any given time [21]. In areas where access to sufficient food is already difficult, *Giardia* can have a devastating

impact far beyond the uncomfortable symptoms of giardiasis. The colonization of the intestinal track by *Giardia* cells is thought to reduce the host's ability to absorb nutrients [6] and may damage the epithelial lining of the host gut [23]. The resulting malnutrition can have significant detrimental effect on a young child's physical and cognitive development [11,24]. Clearly, further research into the biology of this organism and development of new treatments would benefit many millions of people worldwide.

Drug Treatment and Resistance

Giardia infection is currently treated with the nitroimidazole class of drugs, which include metronidazole, tinidazole, oridazole and albendazole. These drugs are toxic to a wide range of anaerobes and microaerophilic micro-organisms [25,26]. Many individuals infected with *Giardia* fail to fully clear the infection, even when treated with metronidazole, the drug of choice for treatment of an anaerobic infection. These individuals will often become the chronic carriers described above [17].

Metronidazole, the drug of choice for treatment of a *Giardia* infection, has a range of negative side effects. These side effects and adverse drug reactions can include nausea, diarrhea, a metallic mouth taste, allergic reactions, headache, dizziness, vomiting, glossitis, stomatitis, dark urine and paraesthesia [27]. High doses and long term treatment with metronidazole have been associated with the development of leukopenia, neutropenia, and an increased risk of peripheral neuropathy or CNS toxicity [27]. Metronidazole has also appeared on the US National Toxicology Program's list of compounds reasonably expected to be a human carcinogen [28], though a definite link to

cancer has not been established.

Additionally, strains of *Giardia lamblia* that show resistance to the nitronidazole class of drugs have started to emerge in recent years [29,30,31,32]. It is clear that identification of new drug targets and development of *Giardia* specific drug treatments would be advantageous to many people and would prevent this disease from becoming untreatable if resistance continues to emerge.

Taxonomy and Evolutionary Significance

Advances in gene sequencing technology have revolutionized the classification of organisms in the tree of life. Traditionally, organisms were classified by morphological similarities. *Giardia*'s full taxonomic classification based on morphological classification is *Eukaryota Protista Sarcomastigophora Zoomastigophora Diplomonada Hexamitidae Giardia lamblia* [33].

Modern classification of organisms uses the information obtained from multiple lines of investigation including genetic, structural and biochemical [33,34]. According to this new system, *Giardia* is classified *Eukaryota, Bikonta, Cabozoa, Excavata, Metamonada, Trichozoa, Eopharyngia, Trepomonadea, Diplozoa, Gardiida, Gardiidae* [33,34].

Regardless of how it is classified, *Giardia* is generally agreed to be an ancient organism

[33] and amongst the earliest divergent eukaryotes [35]. It is missing many of the hallmark subcellular compartments or organelles associated with eukaryotes. It appears to lack mitochondria, peroxisomes, and may lack Golgi apparatus with classical morphology [33,35]. Until recently it was hypothesized that *Giardia* had diverged from the main root of the eukaryotic tree before the evolution or acquisition of mitochondria [36].

However, the discovery of nuclear genes believed to have mitochondrial ancestry [36,37,38] suggests that this was not, in fact, the case. It is now hypothesized that adaption to an anaerobic environment promoted the loss of mitochondria or the conversion of mitochondria into mitochondria remnant organelles known as mitosomes [36].

Study of organisms, like *Giardia*, which are divergent from the commonly studied model organisms (Figure 1.2), can provide information on the evolution of cellular systems [39]. *Giardia* is particularly useful for the study of the evolution of the cytoskeleton. By studying the common and divergent features in distantly related organisms we can begin to understand the evolutionary timeframe of the development of cytoskeletal features [39]. We can also study the way in which ubiquitous structures, such as the microtubule (MT), can be adapted to many diverse functions as part of larger cellular elements.

There are MT cytoskeletal structures with which we are generally familiar, that are common to many or all eukaryote organisms. These structures include the mitotic

spindle, used to separate the chromosomes in mitosis [40,41,42,43,44]: primary cilia, used for sensing the extracellular environment [45]; and motile cilia and flagella [46,47,48].

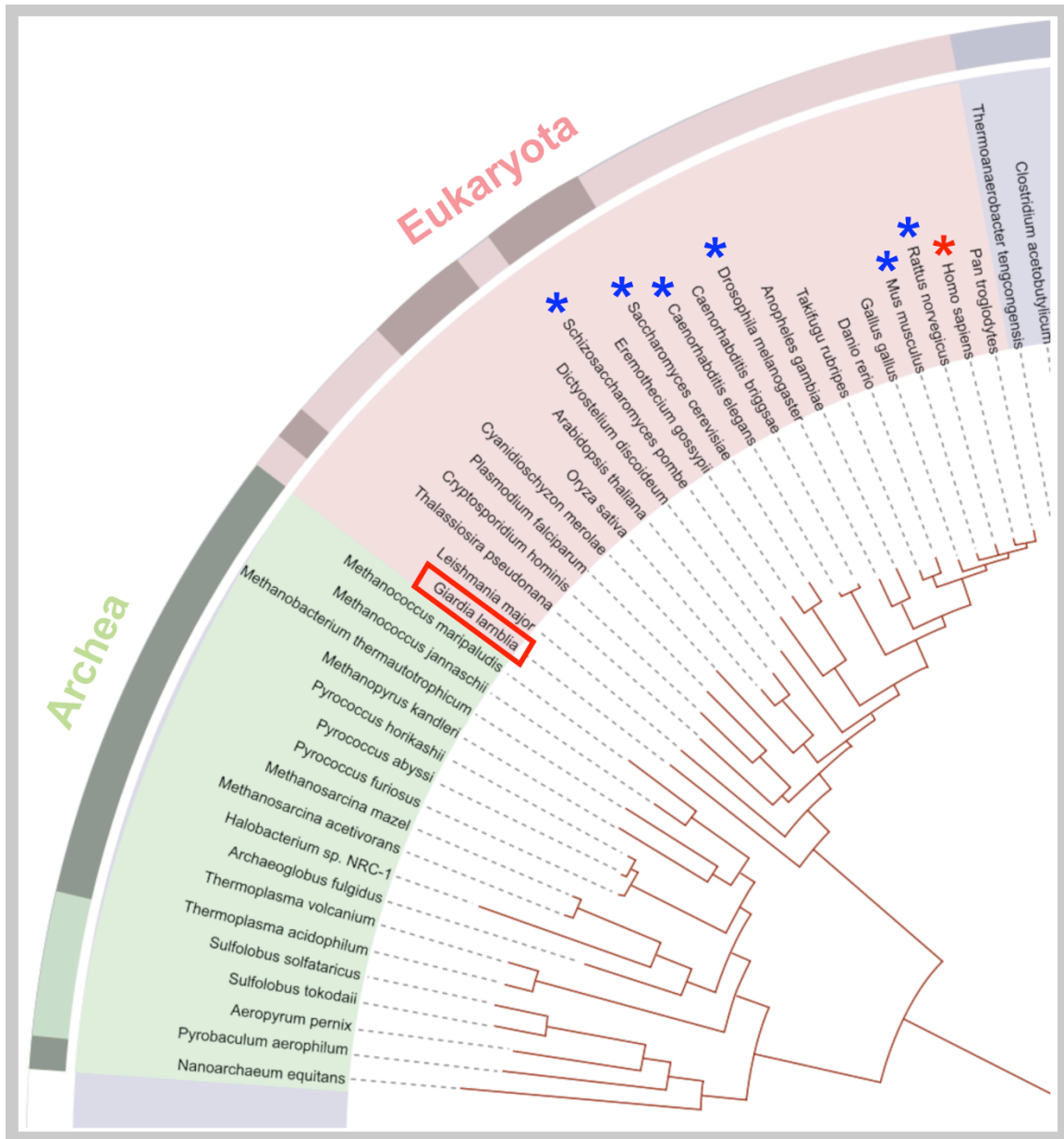


Figure 1.2: Phylogenetic tree showing the position of *Giardia lamblia* relative to other organisms. *Giardia lamblia* is highlighted with a red box. Other commonly studied model organisms are marked by an asterisk, with humans marked in red. This shows the evolutionary separation of *Giardia lamblia* from the other commonly studied organism. Adapted from Letunic, I. and Bork, P., 2006 [49].

Even more diverse MT based structures can be observed in the Excavata kingdom. This

kingdom contains many of the free living and parasitic protists (including *Giardia lamblia*) and is estimated to contain as much diversity as exists between plants, animals and fungi [39,50]. This diversity is exemplified in many unique cytoskeletal structures that carry out a wide range of functions. Examples include the axostyle, which is a sheet or spiraling bundle of MTs contained in the center of the cell [51,52], used for motility and found in a large number of excavates [51,52,53,54,55,56]; the subpellicular MTs array, which is a “corset” of crosslinked MTs, found in *Trypanosoma Brucei*, that define cell shape [57,58,59,60]; and of course the large array of MTs that form the ventral disc in *Giardia* [61,62,63] that facilitates attachment of the cells to their host [64,65].

The study of these diverse MT cytoskeletal features not only provides evolutionary information, but the unique proteins associated with them have the potential to provide new drug targets for treatment of parasitic diseases.

***Giardia* Species**

There are 6 distinct species of *Giardia*: *Giardia agilis*, *Giardia ardeae*, *Giardia lamblia*, *Giardia muris*, *Giardia microti*, and *Giardia psittaci*. *Giardia lamblia* is also known as *Giardia intestinalis* and *Giardia duodenalis*. Despite being a zoonotic parasite, each species and strain has an infection preference for a host or group of related hosts [66,67]. *G.lamblia* is the principle species that infects human beings.

The Genetics of *Giardia*

Sequencing of the genome of *Giardia lamblia*

Giardia lamblia species is divided into eight gene assemblages [68]. Uncertainty still exists as to whether genetic exchange occurs between these eight subgroups or if they should be classified as different species [68,69,70]. The two major genotypes that infect humans are assemblages A and B [66]. The most well studied strain, WBC6, is part of assemblage A.

The genome of WBC6 strain, representing assemblage A, has been completely sequenced. The project was carried out by a number of collaborators from multiple different institutions. The genome is approximately 11.7 mega basepairs in size [70]. It is similar in size to the yeast genome [71], and the largest of bacterial genomes. It is about 2 to 3 hundred times smaller than most mammalian genomes [70].

The sequenced genome was searched for open reading frames and promotor sequences in order to identify sites likely to contain genes. 6470 regions were identified as genes [70]. *E.coli* cells contain approximately 4500 genes [72]. It was discovered that the majority of genes are missing introns commonly found in mammalian genomes [70]. In fact, approximately 77% of the genome is comprised of coding sequences [70]. To put this in context, less than 2% of the human genome is coding sequence. The genes are also packed very close together with the average distance between genes numbers in the hundreds of base pairs [70].

The nuclei

Like other diplomonades, *Giardia* is a binucleate organism. Unlike many other eukaryotic cells, that spend the majority of their time in G1, *Giardia* cells rest in G2 phase [1,73]. The G1 nuclei are each diploid and the G2 nuclei are tetraploid [73]. In a growing culture the cells cycle between 4N and 8N and the cysts are 8N [73]. A single copy of the genome is divided into 5 chromosomes [74]. During cell division the two nuclei divide at approximately the same time [75] and each daughter cell receives one copy of each of the parent nuclei [74]. The nuclei are attached to the ventral disc by unidentified filamentous structures [62,76] and are often associated with the extracted cytoskeletons (personal observation). Both nuclei are transcriptionally active [77].

The Life-Cycle of *Giardia*

Cysts and Infection

Giardia has a two-stage life-cycle where it exists as either a cyst or a trophozoite cell (Figure 1.3). The cysts are the dormant form of *Giardia* that are necessary for initial invasion of the host. The cysts are approximately 5 μm by 8 μm [78] ellipsoids; they are non-motile and have a thick (0.3 μm) proteinaceous coat [78] that confers protection against environmental factors. It is known that the cysts can survive for long periods in cold water. Inside the cysts are two daughter *Giardia* cells that paused in the final stages of mitosis. The cells are poised and ready to complete cytokinesis upon excystation [78].

The cysts rely on the fecal-oral route for transmission to invade a new host. The host must ingest as few as 10 cysts for an infection to be established [2]. The cyst wall allows them to pass through the acidic conditions of the stomach undamaged.

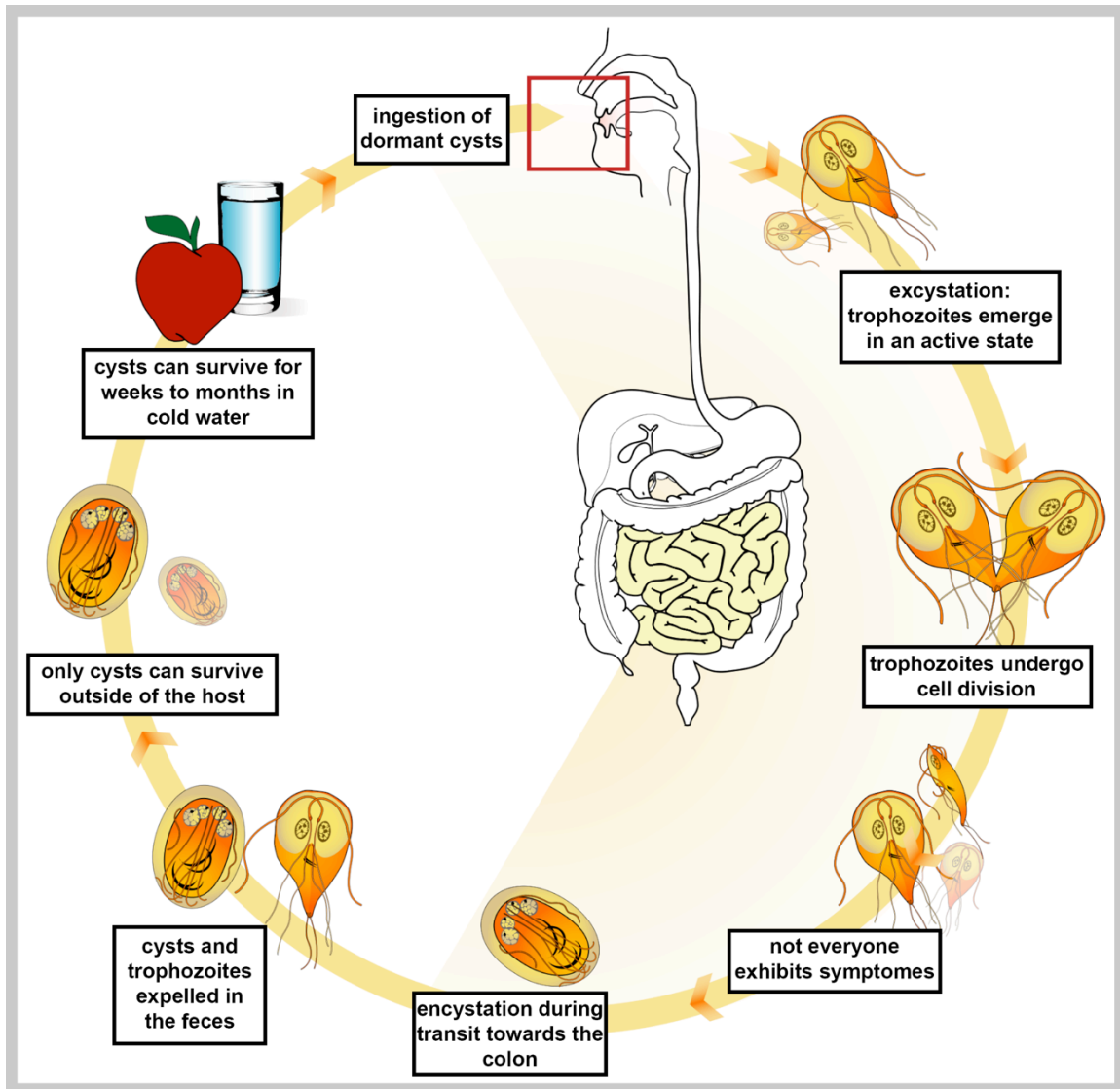


Figure 1.3: Life-cycle of *Giardia lamblia*. The two distinct life stages are represented, with the host stage shown with an orange background and the environmental stage with a white background. Starting from 12 o'clock, the cysts are ingested by the host. Excystation occurs, releasing two mature trophozoites, or feeding cells from each cyst. The trophozoites divide and colonize the small intestine of the host organism. At this point many infected individuals experience the symptoms of giardiasis, though some infections remain asymptomatic. Some trophozoites are induced to encyst. The trophozoite partially completes cell division before the cellular contents are packaged within the cyst wall. The cysts enter the environment in the host's feces. The dormant cysts survive well in the environment including in cold water, until they are ingested by a new host. Adapted from www.commonswiki.org/wiki/File:Giardia_life_cycle_en.svg, this diagram was created by user "LadyofHats" and was released into the public domain in 2008.

Excystation

Environmental signals, such as exposure to acidic conditions and digestive enzymes including chymotrypsin and trypsin, and pancreatic fluid, stimulate the excystation process [79]. Approximately 30 minutes after encountering excystation signals, cytokinesis is completed to produce two daughter trophozoite cells [78] that emerge from a single pole of the cyst [79] through a break in the cyst wall [78].

The Trophozoite Cell

The trophozoite is the active, motile, feeding and replicating [76] form of *Giardia*. The trophozoite cells have a distinctive morphology (Figure 1.4). The cells are approximately 10 to 12 μm in length and 5 to 8 μm at the widest point of the “tear-drop” shaped cell [78]. The ventral surface of the cell is defined by the presence of the ventral flagella and the ventral disc, just under the plasma membrane. The ventral surface always faces towards the host’s cell surfaces, where it is in close contact during attachment [80]. The dorsal surface of the cell faces away from the host cell and into the intestinal lumen.

The trophozoite cell feeds by endocytosing the contents of the intestinal lumen. Vacuoles near the dorsal surface of the cell contain many types of hydrolase enzymes necessary for the breakdown of DNA, RNA and proteins, including immunoglobulins [78]. *Giardia* trophozoites also take up ferritin [78], as their anaerobic metabolism [81,82] is mediated by iron-dependent enzymes [83].

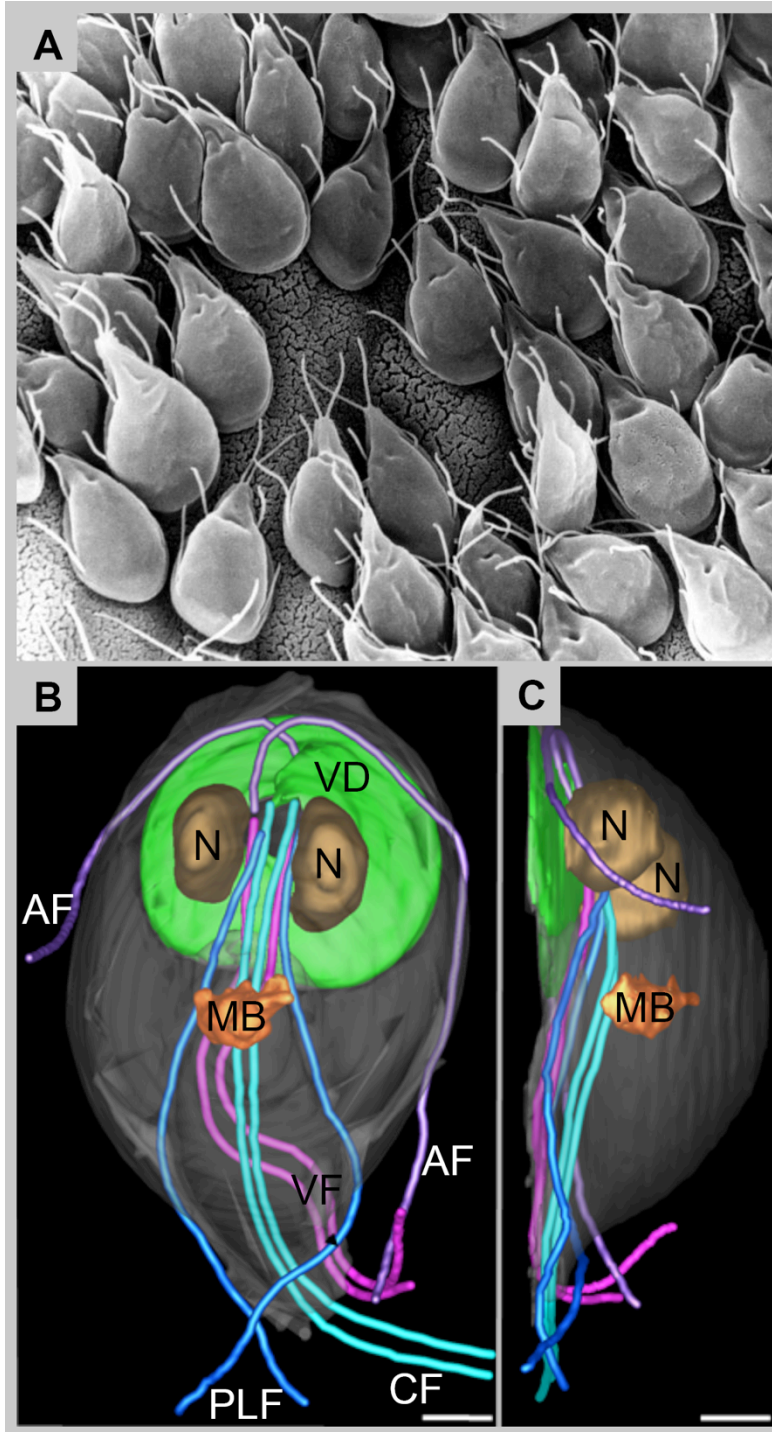


Figure 1.4: Morphology of *Giardia lamblia* trophozoite. Panel A: Scanning Electron Micrograph of trophozoite cells adhered to gerbil intestinal epithelium. Adapted from Erlandsen, S. (1988). **Panel B:** Model view of a trophozoite cell imaged using 3view, a SEM slice and view technique. The cytoskeleton is shown in color, AF = anterior flagella (purple) VF = Ventral flagella (pink) PLF = posterior-lateral flagella (blue) CF = caudal flagella (cyan) MB = median body (orange) N = nuclei (brown) VD = ventral disc (green). **Scale bar = 2 μ m. Panel C:** Side view of the model shown in B. Scale bar = 2 μ m. Both B and C are adapted from Schwartz, C. et al, 2012 [84].

Encystation

Trophozoite cells that experience conditions commonly found in the lower intestine and colon of host are stimulated to encyst. The presence of lactate, primary bile salts, glycocholate, and myristic acid, in a solution of pH7.8, produce optimum conditions for encystation *in vitro* [78]. It takes approximately 44 to 70 hours for complete formation of the cyst wall [78]. During that time, mitosis and nuclear division are completed. A mature cyst is octoploid, with four nuclei present inside the cyst wall [78].

The Microtubule Cytoskeleton

The intracellular morphology of the trophozoite is defined largely by the unique MT cytoskeleton it contains (Figure 1.4). The MT cytoskeleton is organized into several distinctive structures including the ventral disc, four pairs of flagella, the median body and the funis [1].

The Four Pairs of Flagella

Giardia has four pairs of flagella, all with the eukaryotic arrangement of 9 pairs of doublet MTs surrounding a central pair [1,85]. The eight basal bodies of all the flagella are clustered together in the center of the ventral disc [1,85]. Unique to *Giardia* is the fact that all the flagella extend through the cytoplasm [85,86] before exiting the main body of the cell and becoming membrane bound [85].

The flagella do not appear to have transition zones as observed in organisms like *Chlamydomonas reinhardtii* (Cindi Schwartz, unpublished data). The Y-shaped links, which tether the doublet MTs to the membrane, and the transition fibers are normally located just above the basal bodies [87] in eukaryotic flagella. In *Giardia*, the basal bodies are separated from these features by long intracellular portions of the flagella. The Y-shaped links and transition fibers are found in the flagella pockets, in a pinwheel like arrangement, (Cindi Schwartz, unpublished data) far from the basal bodies.

Each pair of flagella exit the main body of the cell at characteristic points [85] and each pair exhibit a distinct motility [85]. The ventral, posterior-lateral, and caudal flagella all extend from their basal bodies, over the ventral disc (over the region known as the ventral groove) before taking different paths to exit the cell.

The Anterior Flagella

The anterior flagella exit the cell at the left and right side in the anterior portion (widest part of the tear drop) of the cell body [85]. They cross over as they associate with the ventral disc. The exterior portion of the anterior flagella move in circular motion [88]. Like all the other pairs of flagella, no movement has been observed in the internal regions.

The Posterior-lateral flagella

The posterior-lateral flagella exit the cell on the left and right sides of the posterior part of the main cell body. They may move in a manner similar to the anterior flagella [88],

though there is some doubt whether they move at all. Both the anterior and posterior-lateral flagella have electron dense matter, flanking the posterior side of their cytoplasmic regions [1,85]. These areas are known as “dense rods” or “ribosome exclusion zones”. The function and composition of this matter is unknown.

The Ventral flagella

The ventral flagella exit the main body of the cell on the ventral surface, just behind the ventral disc. The internal regions have long thin structures associated with them, that, when surrounded by the plasma membrane form fin-like projections [85]. These fins form a region known as the ventral groove extending from the ventral disc to the ventral flagellar pockets. The ventral flagella beat constantly in a sinusoidal pattern whether the cells is swimming, skimming along a surface, or attached [80,88].

The Caudal flagella and Funis

The caudal flagella extend straight from the ventral groove of the ventral disc to the rear of the cell. They exit almost at the posterior tip of the cell. Movement of the caudal flagella has been associated with dorsal/lateral tail flexion and may also involve the funis [85]. The funis is a central cage of MT that surrounds the caudal flagella. Associated with the central cage are MTs that extend out in a fishbone-like arrangement (personal observation). The arrays of MTs extending out are anchored to both the dense rods that flank the posterior-lateral flagella and to a layer of fibrous material, known as the epiplasm, located just under the cytoplasmic membrane [89]. It is thought that the caudal flagella and funis function together to bring about tail flexion [89].

The Median Body

The median body is a somewhat disordered array of stacked MTs unique to *Giardia* [1]. A recent SEM ultrastructural investigation has found that the number and locations of median bodies can vary from cell to cell [90]. The function of the median body is still unknown, but it has been hypothesized that it might act as a reservoir of MT cytoskeletal components, as it has been found to contain beta-giardin [90], which are known to also localize to the ventral disc (Scots paper). The median body was previously thought to be free in the cell but now appear to have connections to the plasma membrane, the ventral disc and the caudal flagella [90]. However, the median body or bodies are either loosely connected to the rest of MT cytoskeleton, or the connections are easily broken during extraction, as they not observed in extracted cytoskeletons.

The Ventral Disc

The ventral disc is a large MT array that forms a right-handed overlapping spiral. The ventral disc was studied extensively in the 1970s and 1980s by David Holberton, at the University of Hull. Holberton used electron micrographs of resin embedded with chemically fixed *Giardia* trophozoites [63] and extracted negatively stained ventral discs [61,91], coupled with biochemical studies [63,91,92,93,94,95] to do some of the foundational work on the ventral disc.

Holberton demonstrated that the ventral disc is composed of MTs, each with a long ribbon-like structure attached to it and extending up towards the dorsal surface of the cell [62]. He called those structures microribbons (MRs). Importantly, Holberton also

demonstrated that the giardins, the proteins thought to be the principle components of the MRs [94,96], can self-assemble into flat filamentous structures unassisted and without the presence of MTs *in vitro* [91,95]. Holberton also established the existence of protein crossbridges [61] connecting adjacent MRs [61,63,96]. He was the first to describe a small structure called a “side-arm” that extends from the marginal sides of the MTs, describing it as connected to the plasma membrane. However, these connections may have been an artifact of sample preparation by chemical fixation as they have not been found in high pressure frozen, resin embedded samples (Cindi Schwartz, personal communication).

Advances in Knowledge of Ventral Disc Structure

Recent work of C. Schwartz et al took advantage of advances in electron microscopy (EM) technology to obtain new and detailed information on the structure of the ventral disc [84]. It was discovered that all the disc MTs have the same polarity; that the MRs are not a single sheet, but actually consist of three trilaminar sheets; and that the ventral disc MTs are decorated by many protein densities that localize to both the inner and outer surface [84].

Microtubule polarity and the locations and structures of microtubule ends

Tomography of freeze substituted, plastic-embedded cells revealed that the minus ends of the disc MTs are located at the dense bands (DBs) and on the center edge [84] (Figure

1.5, Panel A). The DBs are structures of unknown material that function as MT organizing centers for the ventral disc. They are located just in front of the basal bodies and are arranged into two sets. These two sets each have an arrangement like three descending steps. The MT minus ends at the DBs have the characteristic structure of capped MT ends [84,97] and those on the center edge had blunt ends. No MT with opposite polarity were observed [84].

Plastic section tomography and models obtained from slice-and-view blockface imaging [98,99,100] show that the MRs arrangement at the minus ends varies [84]. The MT at the minus ends located at the DBs do not have MRs; very short MRs are first observed on the MTs as they fan out to form the dorsal OZ [84]. The arrangement of MRs at the minus end on the center edge are somewhat different: here the MRs often extend past the MT minus end and exist for a short distance with no MT bound to them [84] (Figure 1.5, Panel B).

Discovery of GMIPs and GMAPs

Cryo-electron tomography (cryo-ET) of extracted frozen-hydrated trophozoite cytoskeletons coupled with sub-volume averaging revealed a structure of the repeating unit that forms the majority of the ventral disc [84] (Figure 1.6). This data expands on what was previously observed by Holberton. The MT is highly decorated with a large quantity of protein densities [84]. The individual identities and functions of each

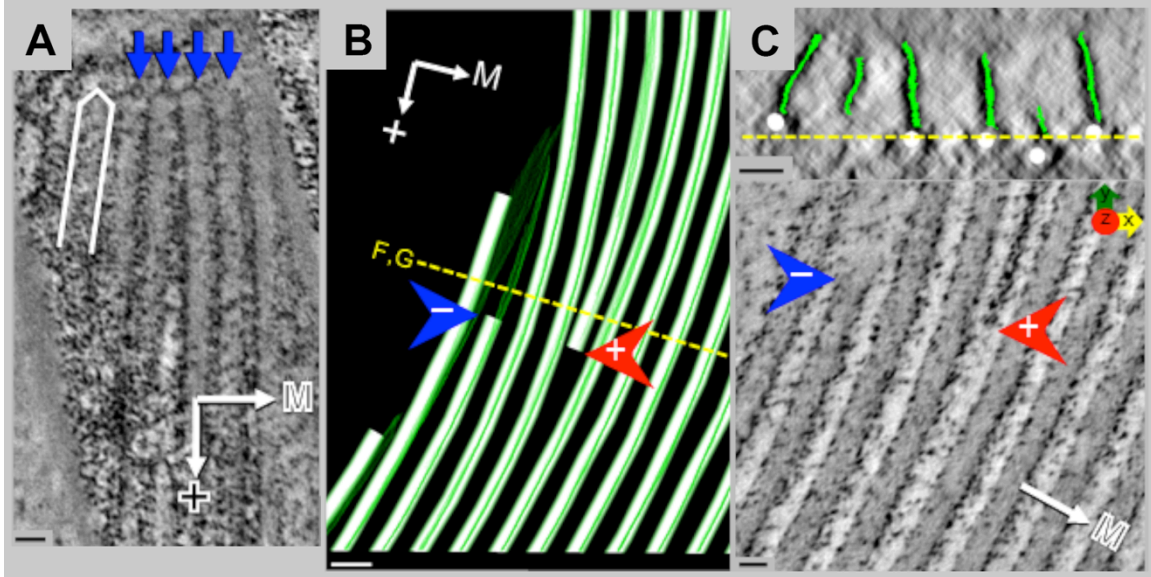


Figure 1.5: Morphology of minus ends in the ventral disc. Panel A: Capped minus end morphology at the dense bands (DBs) which are a major MT organizing center in the ventral disc. A MT minus is outlined in white and others are indicated by blue arrows. The M indicates the direction of the disc margin (outer edge) and the plus sign shows the polarity of the MTs. **Scale bar = 25nm. Panel B:** Model view of a small section of the ventral disc showing the morphology of MT minus ends on the center edge. The ventral disc is oriented dorsal side down. The MT is shown in light green and the MR is shown in dark green. The MR can be seen extending over the blunt minus end of the MTs, indicated by the blue arrow. A MT terminating in the body of the disc is indicated by the red arrow. The plus end is also blunt. The yellow line F,G shows the position of the cross section in C. **Scale bar = 50 nm. Panel C:** The top panel shows the cross-section through the model in panel B, across the F,G line. The MRs are marked in green. The morphology of the MT ends modeled in panel B are shown in the tomographic slice. M indicates the direction of the disc margin. **Scale bar = 25 nm.** Adapted from Schwartz, C. et al, 2012 [84].

observed density are as yet unknown. The structure clearly shows that the MRs are formed from three parallel sheets [84]. A few large densities, including the side-arm, side rail and bridge, and the paddle can be observed binding to multiple protofilaments (PFs) on the outer surface of the MT [84] (Figure 1.6). Three additional densities termed GMAP1, GMAP2 and GMAP3 were observed binding specifically to individual PFs in a regular arrangement [84]. Again, the function of these densities is not known.

The ventral disc is a hyperstable array that does not depolymerize, except during mitosis [76]. The MTs of the disc are insensitive to microtubule depolymerizing drugs [101,102].

This effect is not caused by the low sequence homology of *Giardia* tubulin to classically studied bovine tubulin, as the treatments effectively depolymerize and prevent the assembly of the mitotic spindle [101,102]. It may be that the extensive decoration of the ventral disc MTs with GMIPs and GMAPs provides very effective stabilization of the polymerized tube, maintaining the array.

Three densities were also observed bound to specific PFs on the inner surface of the MTs. These densities have been named GMIP5, GMIP7 and GMIP8. Microtubule inner proteins (MIPs) were first discovered in 2006 by two groups: the McIntosh Lab at the University of Colorado [103] and the Downing Group at the University of California, Berkeley [104]. Examples have been observed in the doublet MTs of sea urchin axonemes [105], *Chlamydomonas* flagella [105] and the cilia of multicellular organisms [103,104]. The identity and function of a MIP has yet to be determined.

The discovery of the presence of MIPs in the ventral disc MTs provides a piece of structural information about ventral disc assembly. The ventral disc does not depolymerize except during mitosis, so, we can reasonably assume that the MIPs are built into the array as the MT are first polymerizing. This begins to hint at highly regulated and complex process of assembly of the ventral disc, that is thus far, very poorly understood.

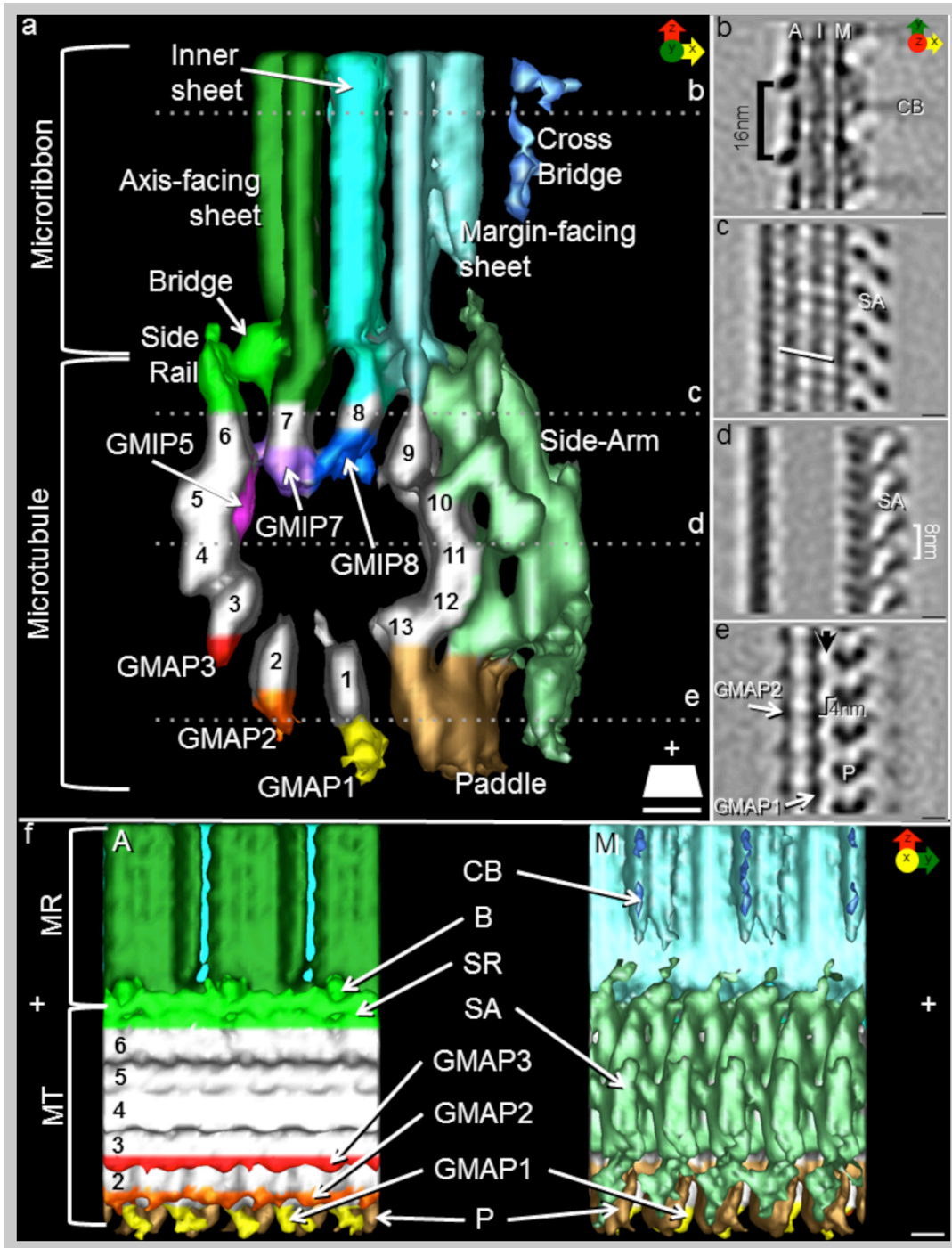


Figure 1.6: High-resolution isosurface representation of the structure of the repeating unit of the ventral disc. Panel a: View of the repeating unit in cross-section, viewed from the minus end. The PFs of the microtubule are colored in light grey and numbered 1 to 13. The MT associated structures have been colored and labeled. **The 3-D scale bar is 5 nm on each side.** Panels b to e: the averaged data at planes b-e as shown in panel a with the major structural features labeled. A = axis facing sheet, I = inner sheet, M = margin-facing sheet, CB = cross-bridge, SA = side-arm, and P = paddle. **Scale bar = 5 nm.** Panel f: The side views of 5 repeating units. The left image is an isosurface representation of the center facing side. The right image is the margin facing side. **Scale bar = 5 nm.** Figure adapted from Schwartz, C. et al, 2012 [84].

Attachment to the Host

The ability to resist peristaltic flow and avoid clearance from the preferred colonization site in the small intestine [1] is the principal challenge faced by *Giardia* trophozoites. In order to avoid clearance, *Giardia* has evolved the ability to attach to the surface of the hosts intestinal epithelial cells, on top of the microvilli [106,107]. In a mature infection, the intestinal epithelium will appear completely covered in attached trophozoites (Figure 1.4, Panel A). Attachment of the trophozoites can be disrupted by changes in temperature, pH, and ionic strength, or lack of serum in the medium [106,108]. However, it is not known if this disruption is a result of the parasite's response to these changes in condition or occurs involuntarily by interrupting an essential process or interaction.

Attachment force

Giardia cells generate significant attachment force to a surface. An attached cell can resist a detachment force of 1.5 nN [109]. Forces of 2.43 ± 0.33 nN or 12,500 x g are required to remove 90% of a trophozoite population from a surface [109]. Investigators carried out centrifugation experiments using attachment surfaces with different chemical properties: positive charges were added to glass cover slips using a poly-L-lysine coating; hydrophobicity was generated by coating with (tridecfluoro-1,1,2,2-tetrahydrooctyl)trichlorosilane (similar to Teflon); and polyethylene glycol was used to generate a surface that would inhibit protein absorption [109]. Interestingly, *Giardia* cells attached well to all of these surfaces and there was very little variation in the force necessary to remove 90% of the population from the different surfaces [109]. This work

points towards a physical mechanism, rather than chemical-interaction based mechanism, for the generation of the principal attachment force. Instead, it has been proposed that chemical interactions might mediate a preference for different host cells lines [1,107].

Proposed Mechanisms of Attachment

There have been two principal physical models proposed as the mechanism by which attachment force is generated: the hydrodynamic model and the suction-cup model. The MT cytoskeleton, and ventral disc in particular, are central to both of these models.

Hydrodynamic model

The hydrodynamic model was originally proposed as a mechanism for attachment by Holberton in 1974 [65] and has been further researched by the Elmendorf group at Georgetown University. In this model the ventral disc is proposed to function as a rigid structure used to maintain a domed space under the surface of the cell. The ventral flagella beat constantly to create fluid flow in through a proposed gap in the lateral crest at the overlap zone. Fluid then flows around the disc and exits this space through a channel created between the two ventral shields. The constant flow of fluid under the ventral disc is hypothesized to generate negative pressure that would result in the adherence of the cell to a surface [65]. Fluid flow under the ventral disc has been observed by tracking the path of quantum dots contain in the *Giardia* medium. (Heidi Elmendorf: International Conference on Anaerobic Protists, 2012, unpublished data).

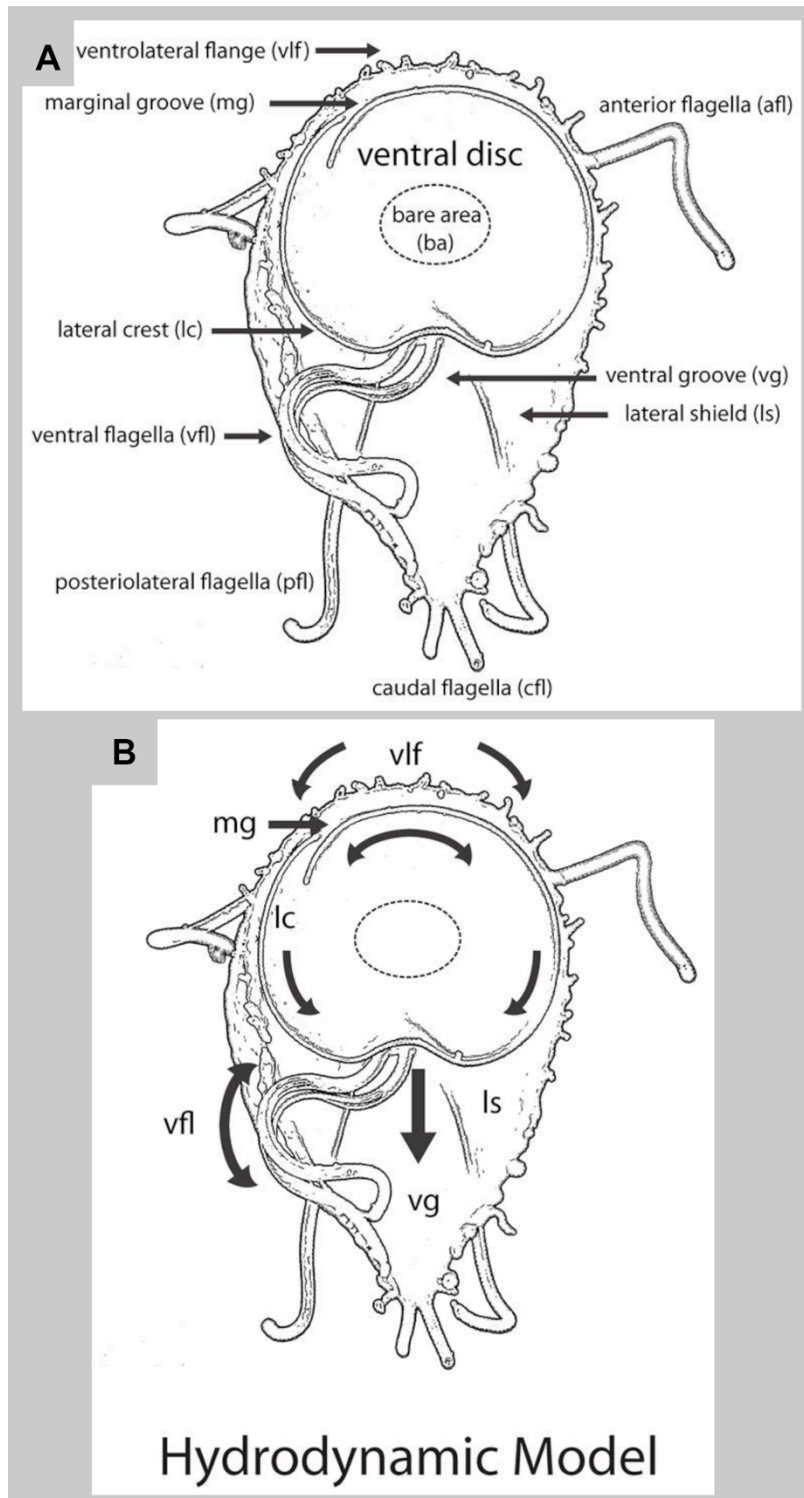


Figure 1.7: The Hydrodynamic model of attachment. Panel A: The ventral surface of the cell is shown with all the morphological features labeled. **Panel B:** Negative pressure is generated by fluid flow under the ventral disc, labels are the same as in panel A. Water is pulled in through the marginal groove (mg), travels around the edge of the disc and out through the ventral groove (vg). The ventral flagella (vfl) bead in a sinusoidal motion generating the force for fluid flow. Adapted from House, S.A. et al, 2011 [80].

However, it was demonstrated that the knockdown of PF16, a protein found in the central pair of the ventral flagella, slowed the frequency of the flagella beat [80]. If the hydrodynamic model were correct, a decrease in fluid flow rate should reduce the force of attachment. Centrifugation experiments carried out to measure the ability of trophozoites to resist detachment forces found there was no significant reduction in the attachment of cells treated with Morpholinos that blocked the translation of PF16 mRNA [80].

The suction- cup model

The suction cup model is again based on the generation of negative pressure. However, instead of constant fluid flow, the negative pressure comes from an increase in volume in an area of completely sealed off space. The Dawson Group has demonstrated that attachment of *Giardia lamblia* occurs in multiple stages [80] (Figure 1.8). Free swimming cells find an attachment surface by an unknown mechanism. First, attaching trophozoites will swim/skim along a surface, with the ventral flange, parts of the ventral shield and the lateral crest (Figure 1.7, Panel A) in partial contact [80]. Next, a lateral crest seal is achieved, where the entire lateral crest is in contact with the surface [80]. Attachment then processes to full lateral shield contact, where both the left and right lateral shields are in close contact with the surface [80]. Attachment is completed with bare area contact [80], completing the generation of negative pressure in a sealed area, like a suction cup.

Though the mechanism by which the attachment force is generated is still not clear, there

is no doubt that the ventral disc plays a central role in both of the leading models proposed. This means the ventral disc is essential to the parasitic life cycle of *Giardia*.

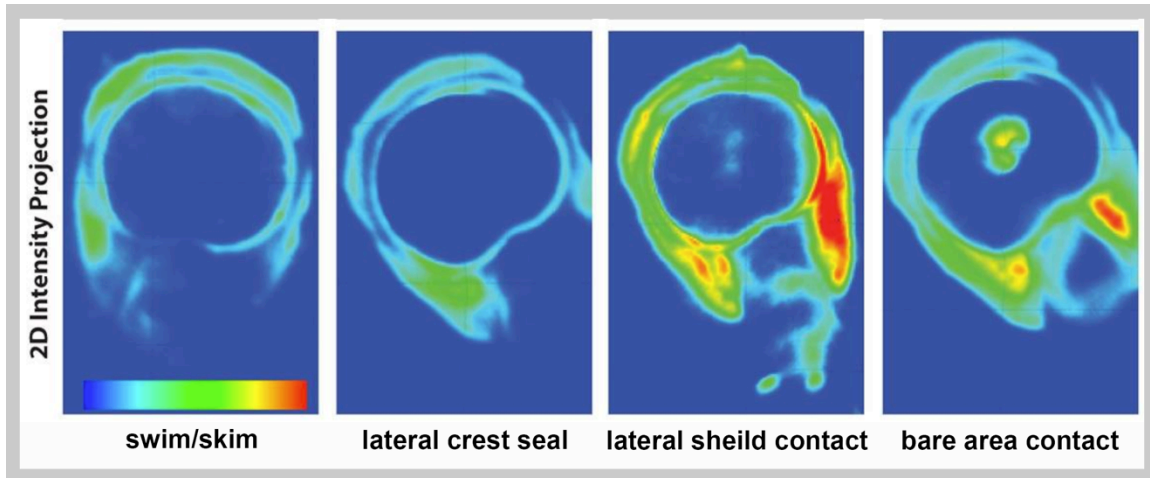


Figure 1.8: Stages of trophozoite attachment. TIRF microscopy was used to image the ventral surface in very close contact to the glass slide. Close contact is indicated by color, with red representing tight seal. Dark blue indicates no contact. The four stages of attachment including: **swim/skim** where the trophozoite makes light contact with the surface and still has forward motion; **lateral crest seal** is formed where the cytoplasm just under the edge of the ventral disc and lateral crest forms a complete contact, forward motion ceases; **lateral shield contact** is where more cytoplasm comes into contact with the surface on their side of the ventral groove; **bare area** makes contact in the center of the disc. Adapted from House, S.A. et al, 2011 [80].

The Ventral Disc and Trophozoite Replication

Attachment is central to the life-cycle of the trophozoite. Mitosis and cell division represents a rare time when the cell will detach from the epithelial lining of the gut of the host [76]. The ventral disc of the parent cell will disassemble as two new daughter ventral discs are built on the dorsal surface of the cell [76]. The mechanism and regulatory processes of ventral disc assembly are still unknown.

The basal bodies of the flagella are involved in the formation of mitotic spindles of the

two nuclei. The nuclei undergo semi open mitosis [76]. The basal bodies of the flagella form the MT organizing centers outside of the nuclear envelopes, which do not fully break down [76]. It is not clear how the flagella reorganize during or after cell division, to tightly associate with the ventral disc in the manner observed in the mature cells.

Protein Composition of the Ventral Disc

Even though the process of assembly of the ventral disc is still unclear, the protein components that associate to the ventral disc MTs are starting to be discovered. Until recently only 15 proteins had been identified which localized to the ventral disc. This list of 15 proteins can be divided into three types: the annexins, also known as alpha-giardins [110,111,112,113]; three striated fiber assemblins, a group which includes beta-giardin, delta-giardin and SALP1, which are thought to compose the MRs [114]; and a single novel protein, unique to *Giardia*, called gamma-giardin [115] also thought to be involved in the structure of MRs. Additionally, ERK1 kinase [116], aurora kinase [117] and two Nek kinases [118], all classically associated with cell cycle control [119,120], have been shown to associate with the ventral disc in a cell-cycle stage dependent manner. The transient association of these four proteins makes them unlikely candidates for being major structural elements of the ventral disc.

Discovery of new disc associated proteins

The Dawson Lab made a significant advancement in the understanding of ventral disc composition. Using a combination of “shotgun” proteomics and fluorescence tagging

experiments, they were able to add 18 new proteins to the list of components [121]. They used a modified version of Holberton's extraction protocol [61] to isolate the MT cytoskeletons of the *Giardia* trophozoites [121]. The cytoskeletons were then subjected to trypsin digestion to produce peptide fragments. The peptide fragments were then separated based on mass-to-charge ratio, using liquid chromatography tandem mass spectrometry [121]. Information from the sequenced *Giardia* genome was used to identify the proteins that were likely to be present, based on the combination peptide fragments. 102 proteins were identified and 58 candidates were chosen for GFP tagging [121]. Protein hits annotated as, or homologous to, known nuclear or metabolic proteins were excluded [121].

Taking advantage of Gateway technology (Invitrogen) [122] a library of putative disc associated proteins (DAPs) in pENTR plasmids (Invitrogen) was generated. These entry plasmids were then rapidly recombined with pDEST plasmids (Invitrogen) to create fusion constructs where the DAP protein was linked to a C-terminal EGFP tag. Using confocal fluorescence microscopy, 18 new proteins were identified that localized to the ventral disc and lateral crest when tagged with EGFP. Five of these DAPs are unique to *Giardia*, with no orthologs having been discovered in other organisms thus far [121]. If the unique DAPs are eventually found to be essential to the structure and function of the ventral disc array, they will surely be attractive targets for the development of new anti-giardal compounds. In addition to DAPs, the Dawson lab also discovered numerous other proteins that localized to specific areas on other cytoskeletal components [121]. It is likely that these DAPs account for the densities observed in the ventral disc repeating unit

structure [84]. Unfortunately, it has not yet been possible to annotate this structure and discover which density corresponds to each DAP.

Regions of the Ventral Disc

Most interestingly, the DAPs did not localize to the whole disc in a uniform manner. Instead, each protein shows a specific pattern of localization to different areas or regions of the disc. This allowed the newly discovered DAPs to be separated into classes by their localization: localization to the whole ventral disc (including and excluding the ventral groove), the disc margin and lateral crest, and the supernumerary MTs snMTs [121] (Figure 1.9). The variance in localization strongly indicates that the ventral disc array is not uniform in structure and not composed of a single identical repeating unit.

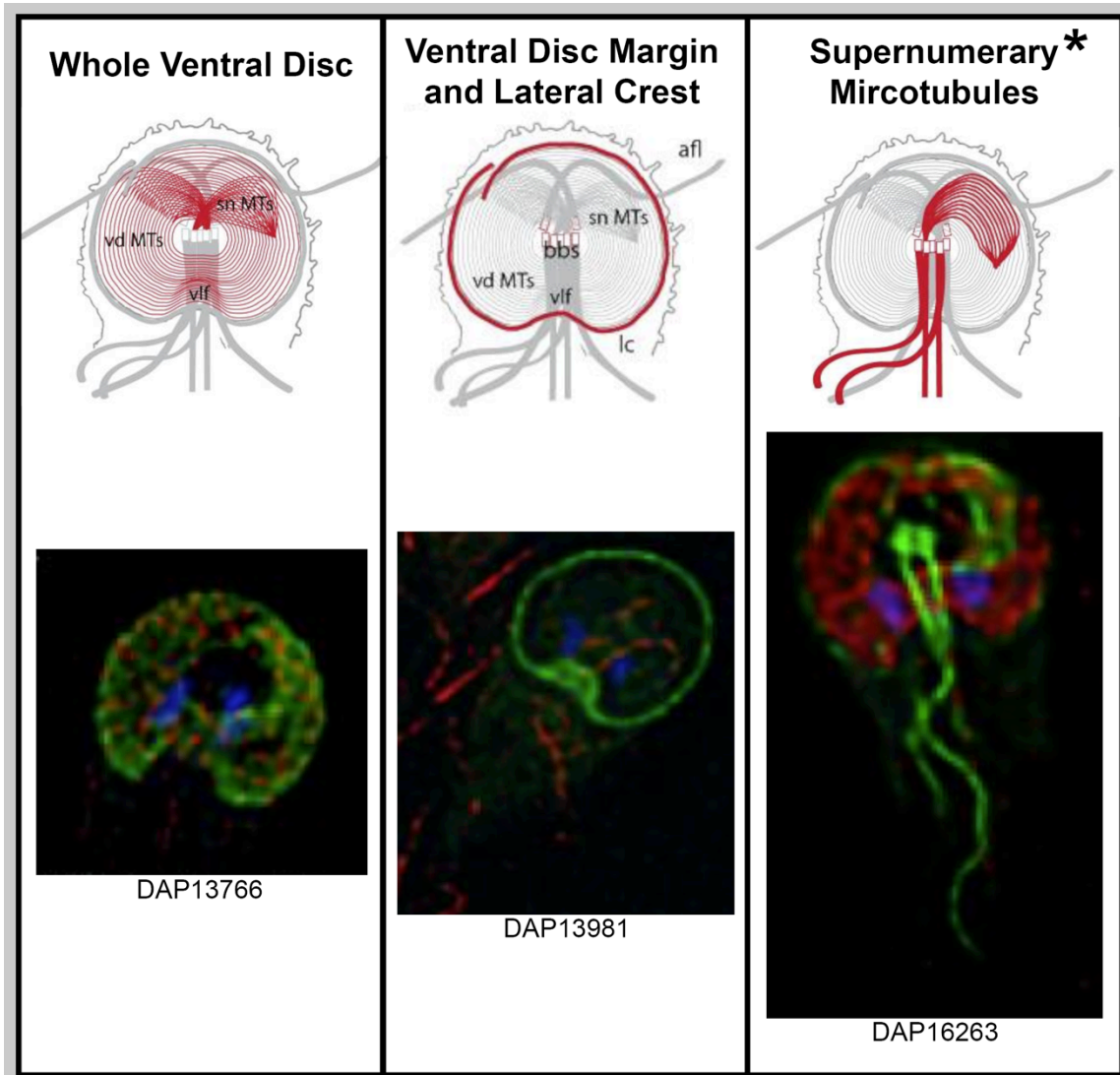


Figure 1.9: Classification of DAPs discovered by the Dawson Lab. In each diagram the location of each class of DAPs is shown in red. vd MTs = ventral disc microtubules, sn MTs = supernumerary microtubules, vlf = ventral flagella, bbs = basal bodies, afl = anterior flagella, lc = lateral crest. The lower images are examples of the localization of each class of DAP. Green is the DAP-GFP fusion protein, red is anti-alpha tubulin, and blue is DAPI-stain, marking the position of the nuclei. * Although the DAPs in this class are currently thought to be localizing to the snMTs, evidence will be presented in chapter 3 that demonstrates this structure, in fact, the overlap zone. Adapted from Hagen, K.D. et al, 2011 [121].

Median Body Protein

Median body protein (MBP) is a DAP that is unique to *Giardia* [121]. It localizes to the

most of the ventral disc, but particularly strongly to the overlap zone [121]. It was originally thought to localize to the median body, hence its misleading name. When MBP is partially knocked down with Morpholinos, the ventral disc loses its domed shape and becomes flattened [123]. The overlap zone also changes in structure to what is referred to as an “open” conformation [123] (Figure 1.10). Importantly, these structural changes in the ventral disc result in impaired attachment of the trophozoite cells [123]. Unique DAPs, like MBP, that are important to ventral disc structure and function represent attractive new targets for anti-giardial compounds that could be both highly specific for *Giardia lamblia* infection and highly effective.

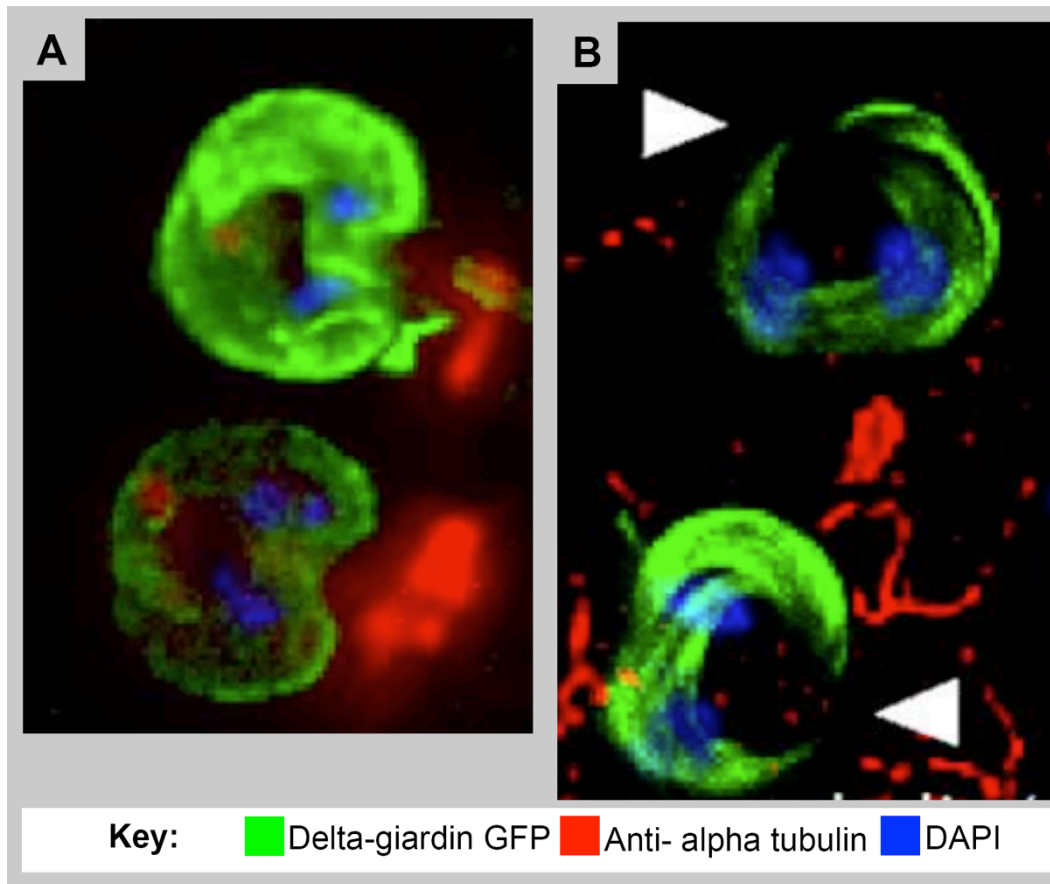


Figure 1.10: Morphology of ventral discs in cells treated to reduce expression of MBP. Panel A: Trophozoite cells treated with mis-sense morpholinos as a negative control. **Panel B:** Trophozoite cells treated with anti-MBP morpholinos to reduce MBP expression. The ventral discs show an open morphology, indicated by the white arrows. However, a corresponding increase in diameter of the disc is not observed. It might be that the phenotype is more complicated than a simple opening of the overlap zone. Adapted from Woessner, D.J., 2012 [123].

This recent work by the Dawson Lab inspired the high-resolution structural examination of the ventral disc that forms the main body of this thesis. It seemed that accurate information about the detailed structure of the arrangement of the ventral disc array and its component parts were not present in the current literature. This information is essential in order to place the newly discovered DAPs in context within the ventral disc structure and to eventually determine their individual functions within the array.

CHAPTER 2: INTRODUCTION TO MODERN ELECTRON MICROSCOPY AND IMAGE PROCESSING

Advances in the field of electron microscopy over the last 25 years have allowed this research to build on and advance our understanding of ventral disc structures that were originally identified by Holberton in the 1970s and 80s [61,62,63,64,65,91,92,93,94,95,124,125,126]. Improvements have occurred in many areas of microscopy including sample preparation, instrumentation, automation, and image processing.

Advances in Microscope and Detector Technology

The basic set up of the electron microscope (Figure 2.1) has not altered much in recent years. However, individual elements of the scopes, such as the electron emission source and electron detectors, have been improved so that higher resolution information can be obtained.

Beam generation from the FEG tip

Modern electron microscopes set up for high resolution imaging use a field emission gun (FEG) tip to generate the electron beam [127]. The electron beam produced is narrower in diameter, up to three orders of magnitude brighter, and consists of a smaller range of electron energies than the beam produced by conventional tungsten or lanthanum

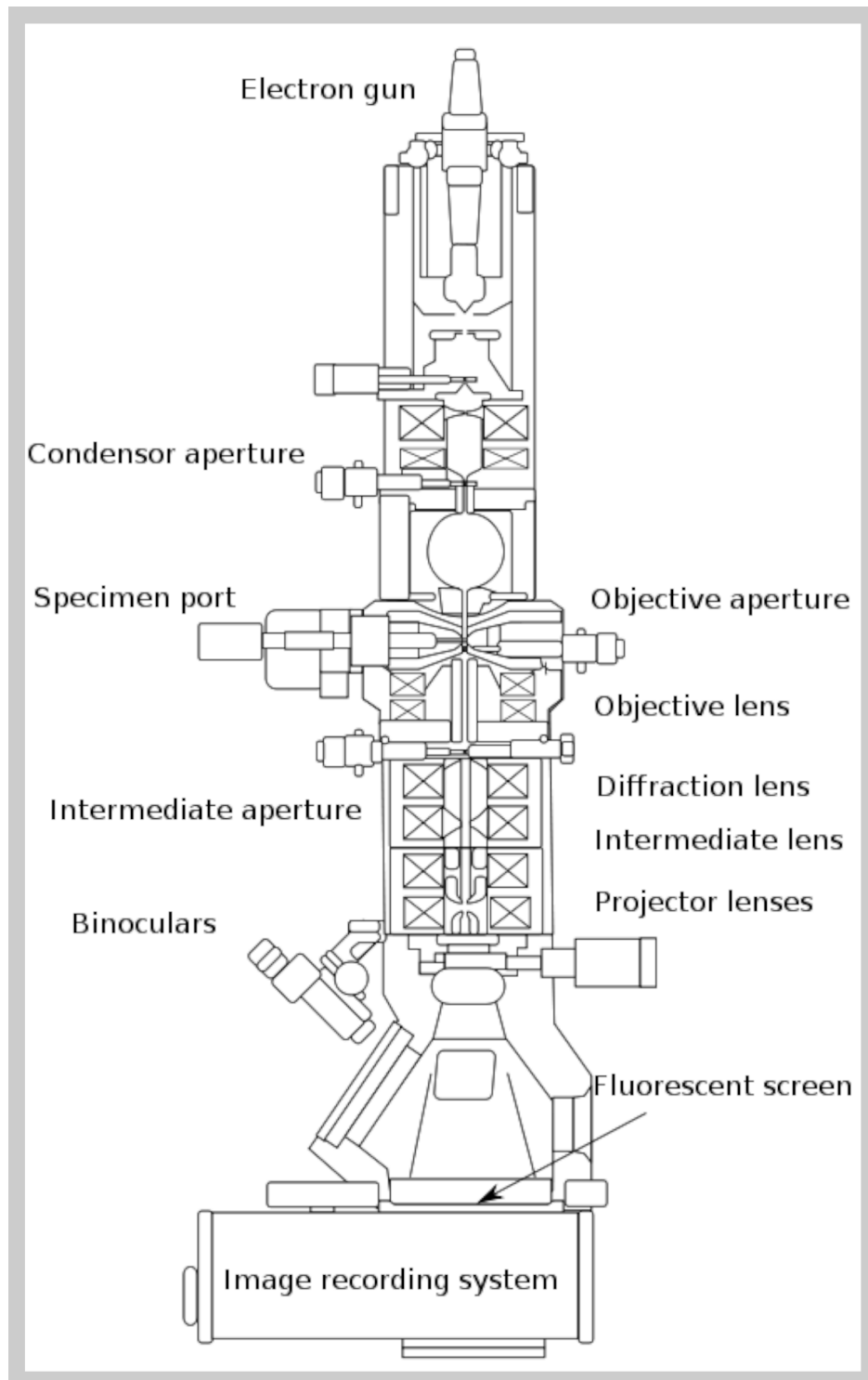


Figure 2.1: Schematic diagram of the modern electron microscope.

hexaboride filaments. The greater coherence of the beam generated by a FEG tip greatly enhances the signal-to-noise ratio and produces clearer Thon rings in the power spectrum.

Energy filtering reduces noise

An energy filter located between the sample and detector allows electrons carrying information that is not useful to image construction to be removed, helping to enhance the signal-to-noise ratio of low contrast samples [128,129,130,131]. The energy filter is used to select for electrons in the zero-loss peak. These electrons have been elastically scattered by the sample and their phase shifts carry the useful information that will form the image [128,129,130,131]. Plasmon resonance electrons and electrons from the atomic core-loss peak are filtered out as they do not carry useful information for imaging and contribute towards noise in the sample.

CCD detectors allow real-time image collection and digitization

The development of charged-coupled device (CCD) detectors have removed the need for the use of film in TEM. In the TEM beam, electrons first interact with a scintillator to produce photons that can be detected by the CCD [132]. Fiber optics then delivers the photons to an array of single pixel sensors formed by an integrated circuit etched onto a silicon surface. The potential well in each pixel collects incoming photons, converting them to electrical charge [133]. Each pixel can only hold a finite amount of charge so that the array can be saturated and no more information can be obtained from continued exposure [133]. After image collection pixels are read out sequentially as charge is

transferred through the array. The charge is converted to digital information proportional to the sum of the electrons present at each pixel [132,133].

The use of CCD detectors allows images to be displayed on a computer monitor in real time, increasing the efficiency of collection. The images are already digital and therefore can be directly transferred for image processing, without an intermediate scanning step that was necessary when micrographs were collected on film.

Future of EM with direct electron cameras

Direct electron detectors eliminate the need for the scintillator that converts the beam electrons to photons. Direct electron detectors are also able to directly count individual incoming electrons rather than converting the sum of the charge to binned digital information [134]. These cameras have higher quantum efficiencies that produce better contrast at low spatial frequencies [134]. This means that cryo-imaging can be carried out closer to focus and better resolution can be achieved [134]. These new detectors represent the future of high-resolution imaging.

Electron Tomography

Electron tomography is the computational 3D reconstruction of a specimen from a series

of aligned projection images. In the electron microscope, there is such a large depth of focus [135] that a single image is essentially the result of the sum of the electron interactions with all levels of the sample along its Z-axis. It is not possible to determine the orientation of the sample on the grid or if there are multiple objects obscuring each other in Z [133] in the final image. Computing a tomogram overcomes this problem and allows the object or area of interest to be rotated and sliced computationally, allowing it to yield more useful structural information. In order to reconstruct a 3D volume, the object must be imaged from different orientations. In tomography, this is done by acquiring a tilt series.

A tilt series of projection images

Acquiring a tilt series involves tilting the stage around a central tilt axis that is perpendicular to the optical axis of the beam [135]. Imaging is carried out sequentially at regular tilt angle intervals; usually small intervals from 1° up to 5° apart [133]. In order to do this, a stable tilting stage is needed and the microscope must be well aligned so that the imaging area remains eucentric, to prevent magnification and defocus changes from occurring down the central axis at different angles of tilt. Ideally, the sample would be imaged through 180° [133], as is the case in of a X-ray based computed tomography (CT) scan and medical imaging. This is not possible in the electron microscope due to the thickness of the sample [133], plus its supporting grid and holder. The maximum angles of tilt that can be used to obtain useful information are +/- 70° [135,136,137], though going beyond +/- 60° is not appropriate for most samples because they are too thick and receive too much damage from the increase in total dose needed to acquire the extra

images.

This means that every tilt series and reconstructed tomogram, will have a portion of the projection information missing [138]. In Fourier space, the missing information forms a characteristic shape, named the “missing wedge” [133,135,138]. This missing information causes a loss of resolution along the Z-axis in the real space reconstruction [133,135,138] (Figure 2.2).

Software, such as SerialEM, allows the automatic acquisition of a tilt series [139]. After initial set up by the user, SerialEM tilts the stage automatically, tracks the stage position to make sure the area of interest is still in the field of view and that the position of the tilt axis is maintained, adjusts the Z-height so that target defocus is maintained, measures drift and controls beam intensity and dose [139].

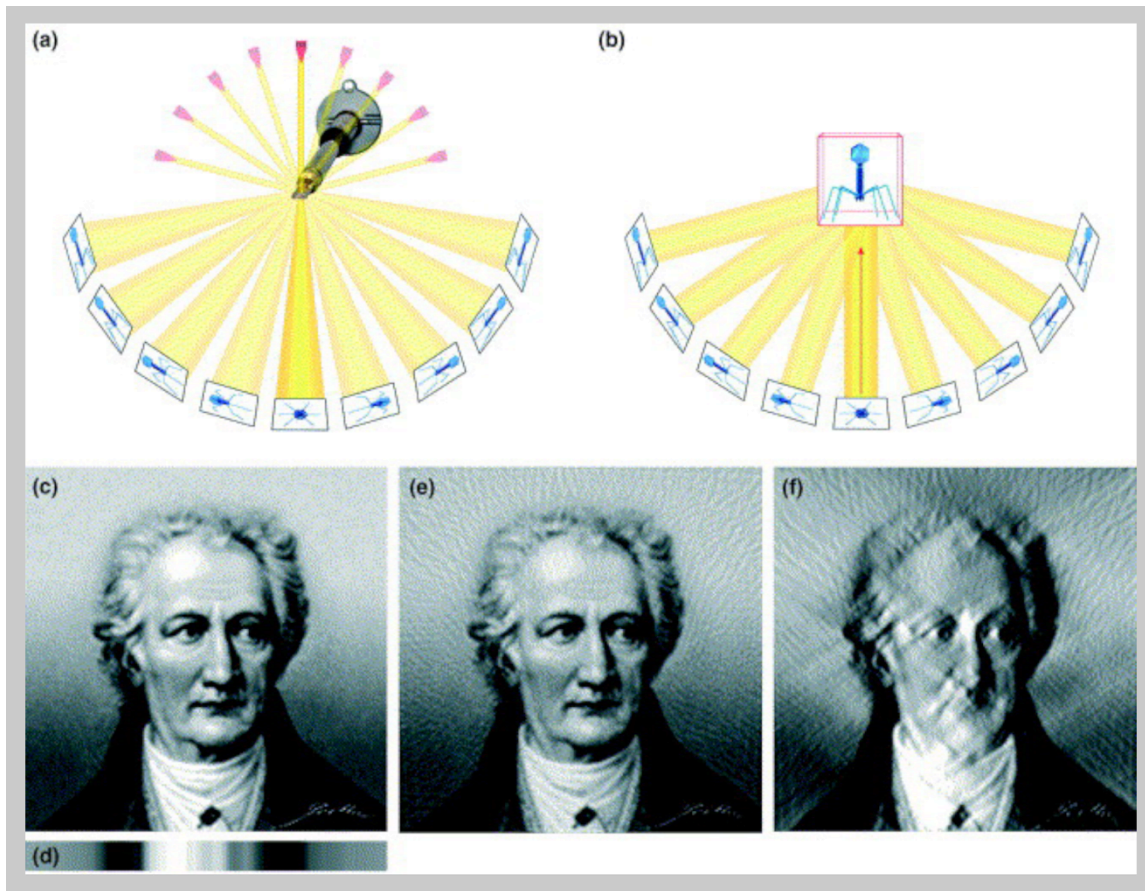


Figure 2.2: Tomographic reconstruction of tilt series data containing a missing wedge. (a): By tilting the sample projection images are collected from different angles. This procedure provides views and information about the sample that cannot be obtained from a single projection image. **(b):** A 3D tomographic reconstruction is computed from the aligned tilt stack of information. **(c to d):** An image of the famous writer and politician Johann Wolfgang von Goethe used to illustrate the effect of the missing wedge on the reconstructed tomogram. **(c):** A 2D image of Goethe representing a slice from a 3D object, oriented perpendicular to the tilt axis in the EM. **(d):** A projection of the 2D object shown in c. The distribution of densities represented, in light and dark, result from the summation of all vertically aligned components in image c. **(e):** A computationally reconstructed image of Goethe obtained from back projecting a tilt series of image c, if projections were obtained over 180° at increments of 2° . This reconstruction is missing comparatively little data and could only be improved by decreasing the increment size between images. **(f):** A reconstruction of Goethe representative the imaging limitation generally imposed in the EM. The projections represent images from $+60^\circ$ to -60° , with the same increment as in e. Because of the missing wedge of data the quality of the reconstruction is anisotropically degraded. Structural elements of Goethe composed mostly vertical information, such as the shoulders, nose and ears are still sharp. However, horizontal structures, like the mouth and brows, are poorly defined. Adapted from McIntosh, J.R. et al, 2005 [138].

3-D reconstruction

Digital projection images can be reconstructed computationally into 3-D volumes using

specialized software. The Boulder Lab for 3D EM of Cells developed IMOD [139] for this purpose. This software is a powerful tool for aligning the tilt stack of projection images and calculating and constructing the best estimate of the 3D arrangement of the specimen.

The first stage of image processing is the computational removal of X-rays from the images of the tilt stack. High energy X-rays will cause saturation of the CCD pixels and “bloom” into neighboring pixels. This can obscure useful information in the 3D reconstruction and can distort the dynamic range of the image. These pixels are removed by smoothing the very high and low values to match the surroundings.

Next, a rough alignment of the stack of images is computed based on the correlations of the densities in the projections. The actual calculations are carried out in Fourier space. A fiducial model is then generated so that the images can be aligned precisely. There are multiple ways to generate this model. The most accurate alignment is produced from a fiducial model of real fiducial particles within each image of the tilt stack. These fiducial markers are small gold particles of a defined size which are included in the specimen preparation. They produce very dark areas on the images. A model of the positions of these particles can be generated automatically or by hand. The fiducials are then tracked through the image stack and the images are aligned so that the path of each fiducial is as close to ideal as possible. R-weighted backprojection is then used to compute the 3D volume from a series of 2D images taken from different angles [133,140,141]. In order to compute the alignment, the 2D projection images are effectively smeared along the axis

of the beam [141,142] and summed at points of intersection [142]. Weighted back projection algorithms also filter intensities so that low frequencies are not over represented in the final reconstruction [142].

Maintaining correct handedness

ET has classically been used to image cellular components, most of which do not have an innate handedness visible on the scale at which they are being imaged [143,144]. Now that the available technology (direct electron detectors), sample preparation and computational handling of data (subvolume averaging) have increased resolution closer to the atomic scale [145,146], the maintenance of correct handedness of the object of interest in the final 3D reconstruction must be considered [143]. If handled incorrectly, the final 3D volume will be the mirror image of the true volume in the sample [143]. Handedness was an important consideration for this research as the ventral disc is one of only a few large macromolecular arrays to have innate handedness in the large structure; and structures from the ventral disc were obtained with resolution greater than 5 nm using subvolume averaging [138,143].

The apparent handedness of the object of interest in the 3D reconstruction is influenced during data collection, computational reconstruction of the tomogram, and the display of the object relative to the perspective of the user [143]. The microscope effect of magnification changes have been calibrated with the software used in the Boulder Laboratory for 3D EM of cells to ensure the maintenance of correct handedness of all

data obtained and processed here.

Montaging Allows Large Area Imaging at Higher Resolution

Montaging is a way to obtain higher magnification tomograms, of small and detailed components of a system within a large X,Y area where context is important. This technique was essential for acquiring the information that allowed the layout of the MT array of the ventral disc to be determined (Chapter 3).

Acquiring a Montage

Montaging can be used to obtain large tomograms at high magnification. Normally, as magnification is increased, the field of view is reduced [135]. Instead of taking one image at a lower magnification so that all the area of interest is contained within the field of view, many sequential overlapping images are acquired at a higher magnification so that the whole area of interest is imaged. This is repeated at each angle of tilt to create a tilt stack. It must be considered that areas where the images overlap can receive up to four times the dose of each individual image at each angle of tilt. This technique is most amenable to samples prepared by resin embedding or negative stain that can withstand more dosage before beam damage significantly alters the structure of the object.

Reconstruction of a montage of tomograms

A montaged tilt stack is reconstructed into a 3D volume just like a normal tomogram, except extra processing steps are required to optimize the alignment of the overlapping images. Alignment can be difficult because of unpredictable distortion effects, especially at the areas of image overlap due to sample warping and other complex optical aberrations [147]. Mass-loss in these areas can also result in distortion and make final image alignment more difficult, especially if surface fiducial markers are used that do not reflect changes in the interior of the sample [147].

Cryo- Electron Tomography

Cryo-electron microscopy (cryo-EM) was originally developed in 1984 by Jacques Dubochet's group at the European Molecular Biology Laboratory (EMBL). The idea behind this method is to preserve the sample in a condition as close to native as possible while still allowing it to be imaged under vacuum and exposed to radiation.

Sample preparation for cryo-electron microscopy

Sample preparation for cryo-EM involves adding a small volume of the sample solution to a suitable support film on an EM grid. The grid is then blotted so that much of the solution is removed and only a thin film remains. Before a significant amount of

evaporation can occur, the sample is plunged into a very cold liquid ethane/propane mixture with a high specific heat capacity, in order to induce rapid freezing. The aim of the process is to freeze the sample so quickly that the ice is vitreous and the sample is not damaged by the formation of ice crystals.

Traditional methods of sample preparation for EM often involved chemical fixation and heavy metal staining to increase contrast, and even drying. This was appropriate in the cellular context where large structural features were preserved well enough to image. However, structures, for example protein complexes, in the nanometer range, were significantly altered by these methods of preparation. The contrast from stained samples results from scattering of the electrons by the large atoms of the stain and therefore provides indirect information on the object of interest [138].

Limitations of cryo-electron microscopy

Even though cryo-EM allows for the collection of images of biological objects as close to the true solution structure as possible, there are drawbacks to the technique. First, sample preparation, handling and imaging are more difficult than with traditional EM. A well-trained and skilled user is required to obtain high quality data.

The principal limitation with images obtained from cryo-EM is the very low signal to noise ratio. This results from two properties of the sample. The first is that only a low dose of electrons can be applied to the sample before it is damaged beyond the point of

being useful by ionization caused by the electron beam [148]. Plunge frozen samples are not protected by fixation, stain or resin, and are quickly damaged by the radiation of the beam. Applying fewer electrons means that less information can be obtained to form the images versus the background noise.

The second problem stems from the chemical composition of the sample and the absence of heavy metal stain. The brightfield contrast in the final image is constructed from two different types of contrast that result from elastic scattering of electrons [148]. As the electrons pass through the sample their path will be altered, if they pass close enough to the nucleus of an atom to be effected by its attractive force.

The first type of contrast is from electrons that, after interacting with the sample, were scattered at an angle larger than will allow them to pass through the objective aperture [148]. This is known as scattering contrast [148] and mostly results from the presence of heavy atoms with large nuclei (such as those found in stains and fiducial particles). The electron is physically prevented from reaching the detector and the absence of signal produces a dark area in the final image (Figure 2.3).

Contrast also comes from interference between the scattered wave and the incident (electrons not scattered by any atomic nuclei) wave at the point where the image is formed [148]. This is known as phase contrast and results from electrons that are scattered by the sample, but not at an angle so large that they cannot pass through the

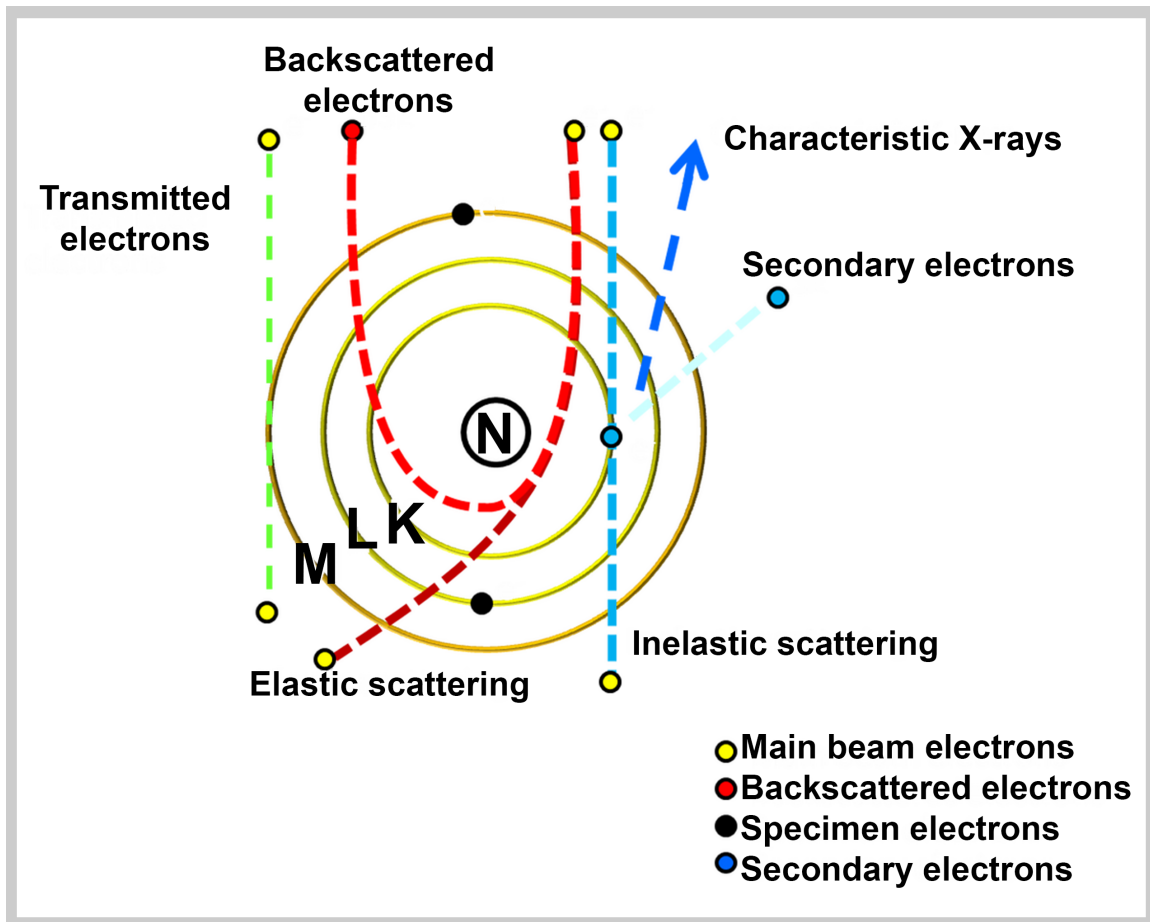


Figure 2.3: Types of electron scattering that result from interaction of the beam electrons with the atoms of the specimen. Adapted from www.biologicalelectronmicroscopy.com

objective aperture. Biological samples are composed of light elements including carbon, hydrogen, oxygen, nitrogen, sulphur, phosphorous etc. Because of the low atomic mass of these elements, the structures in the sample do not cause large angles of scattering of the electrons of the beam. In fact, the biological information in the images results mostly from phase contrast from the difference in mass between the sample and the buffer solution it is contained in [138], and comes directly from the object of interest.

In order to increase the contrast, cryo-samples are often imaged under focus. These

negative defocus values increase the contrast of the image by adding an additional phase shift to all electrons that interact with the sample relative to the incident beam that results from the lack of perfect focus at the sample. This extra contrast makes the material present distinguishable from the background. However, if not corrected for can result in a distortion of the true structure in the final tomographic reconstruction.

Contrast Transfer Function Correction

The brightfield image formed from a sample in the electron microscope is modulated by the contrast transfer function (CTF). The only parameter of the CTF that the user can control is the defocus value (Figure 2.4). Altering this value will change the contrast and will emphasize different features within a sample, depending on the value chosen. The CTF causes the phases to oscillate between -1 and +1 as the spatial frequencies change from low to high. When the function crosses zero the contrast is inverted and, instead of yielding interpretable data, it detracts from the amplitude of the information in the micrograph.

CTF correction attempts to computationally recover information about the sample lost where the CTF function has dropped below zero. IMOD carries out CTF correction using a method known as phase flipping [149] where the contrast of the information in these

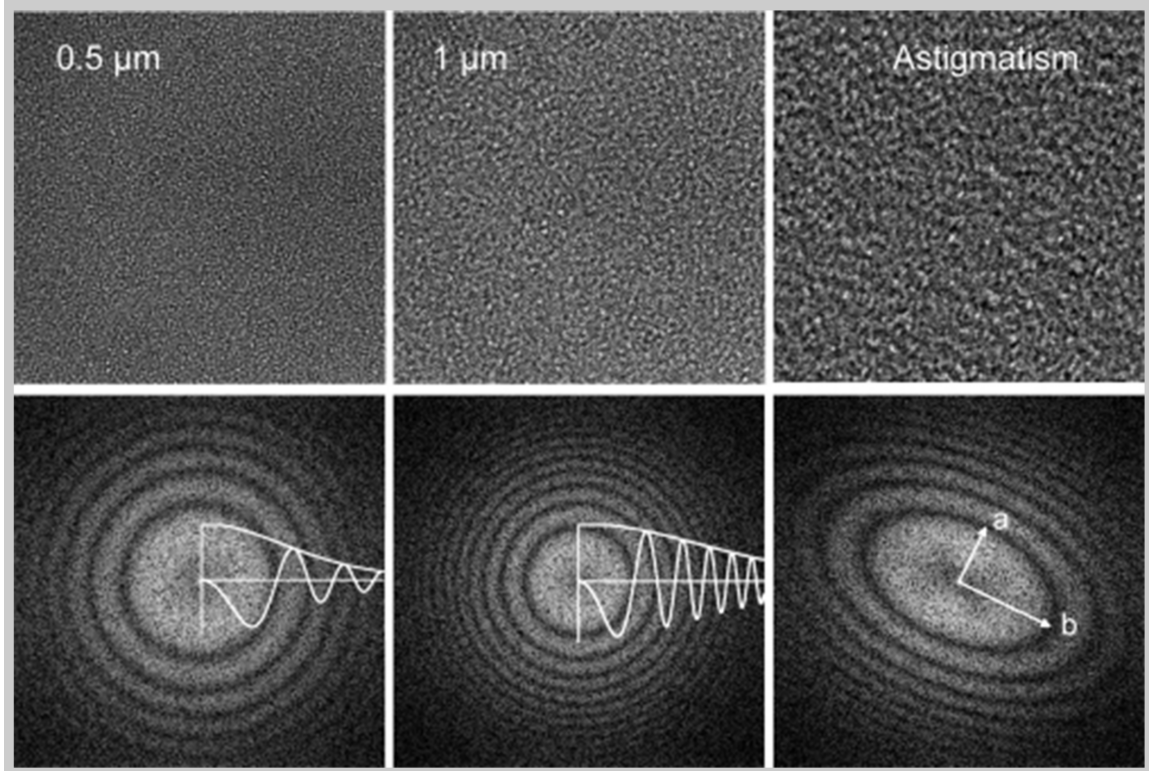


Figure 2.4: Images of carbon film collected using different defocus values. The CTF for each image shown in reciprocal space in the lower row. Left: Carbon film imaged using $0.5\ \mu\text{m}$ defocus. The Thon rings are clearly visible in reciprocal space demonstrating how the CTF oscillates between 1 and -1. The frequency of oscillation increases at high spacial frequencies. **Middle:** An image of the carbon film taken at $1\ \mu\text{m}$ defocus. The film appears to have more surface features. The lower image shows the effect of the increased defocus value on the frequency of oscillation of the CTF in reciprocal space. The higher the defocus value, the more often the CTF drops below 0. **Right:** The carbon film has been imaged with a non-round or astigmatic beam. The distortion of the image is easily visible in reciprocal space. The Thon rings are elongated along the axis (b) perpendicular to the long axis of the ellipsoid beam. Adapted from Orlova, E.V. et al, 2011.

regions is effectively reversed [150,151,152]. In order to do this for a tomogram, the parameters described above must be known for the individual microscope used to acquire the tilt stack. It is also necessary to calculate an accurate value for the defocus over small ranges of tilt angles.

When the CTF is corrected for, the signal to noise ratio is increased slightly, improving the quality of the tomogram [153]. This correction prevents distortions in the final 3D

reconstruction resulting from the relatively high defocus values used in cryo-EM [153].

Subvolume Averaging

Subvolume averaging a computation method that allows higher resolution information to be obtained from cryo-ET with a poor signal-to-noise ratio [103,154]. The objects of interest used for subvolume averaging are often contained within a larger cellular volume, or in the case of this research, exist along the length of cytoskeletal tubular structures. In the case of the ventral disc, the repeating structures exist along the length of a MT and therefore cannot exist as individual isolated units. This means that single particle methods cannot be employed as individual 2D projection images, containing the structure of interest in many different orientations cannot be obtained. Instead, ET must be used, as the objects of interest are continuous and are biased to a limited range of orientations or cannot be purified to homogeneity from the larger cellular environment [154].

3-D information is obtained instead by tomographic reconstruction described above. The maximum resolution that can be obtained in practice from a single un-averaged object in a cryo-tomogram is approximately 5 nm or 50 angstroms [154], high resolution information exists within the volume but is not interpretable because it is obscured by the high level of background noise. Aligning and averaging many of the same objects together improves the signal-to-noise ratio and resolution of the structural features of the

object.

After objects of interest within the larger tomogram volume are identified, they can be averaged together in an iterative process [154,155]. The subvolumes are aligned to a reference and an averaged structure is generated. This structure functions as a reference for further rounds of alignment refinement [154,155]. Eventually a stable structure is converged on so that no changes occur and no more refinement is necessary [154,155]. In order to converge on the correct final structure, it is often necessary to use a missing wedge correction to decrease the bias from of the missing wedge of data in the alignment in Fourier space [155,156].

Averaging subvolumes together increases the signal-to-noise ratio significantly [157]. The signal is amplified, whereas the noise cancels out and is decreased, increasing resolution [157]. Additionally, if the orientation of the object of interest is different within each subvolume, the missing wedge and distortion will be present in a different area of the structure. Averaging the subvolumes can fill in some of the missing information and compensate for the missing wedge, making the resolution of the final structure closer to being isotropic [154]. These improvements usually yield structures with resolutions of approximately 2 nm, when no other methods of structural solution are used to assist [154].

Limitations of Subvolume Averaging

There are some important limitations to the types of data that are suitable for subvolume averaging and to the way the results should be interpreted.

An important consideration is that the first step of any alignment is the definition of the subvolumes by the user. This means that the single objects to be averaged must have sufficiently large lower resolution structures, with sufficient contrast so they can be distinguished from other material within the tomogram by the user [154]. Beyond this, it is important that the user is able to define the orientation of an asymmetrical object within the larger volume. This greatly improves the initial alignment and decreases the search angles required to achieve alignment, reducing computational time.

Another important consideration is sample heterogeneity. To be suitable for subvolume averaging the sample should be as homogeneous as possible. The alignment is based on correlation of densities in different subvolumes, so that the signal-to-noise ratio is improved so that structures are revealed that are not obvious in a single subvolume. If there are variations between the subvolumes, the heterogeneous elements will not be enhanced and will not appear in the final structure. Averaging a sample with large amounts of heterogeneity will fail to yield a useful result. However, if the variation exists as distinct structural conformations it may be possible to identify sub-classes of the structures that could not be identified by eye [157].

Ultimately, the resolution of any structure that can be obtained from averaging is limited by a number of factors: the quality of the tomographic data, where things like thickness of the sample can limit the resolution; the flexibility and therefore heterogeneity of the objects in the subvolumes; and lastly the amount of input data available [154]. In general, the more subvolumes that can be averaged the better the resolution of the final structure. In order to increase the amount of data, subvolumes from multiple tomograms can be included in an average. However, this can increase sample heterogeneity due to sample preparation and imaging condition artifacts.

An important limitation in the computation of subvolume averages is reference bias, where the final structure tends to resemble the initial reference, even if it is not a good representation of what is present in the individual subvolumes. There are several ways to minimize reference bias: these include using an initial reference with no structural features, composed of pure noise or using a multi-particle reference so that the initial reference does not come from a single subvolume, but from an initial cautious alignment of subvolumes that are randomly selected. Reference bias can be checked for by using different starting references [154]. The same data should always yield the same final average structure when different starting references are used.

Another computational issue that can arise from subvolume averaging is over-alignment. Over-alignment can produce a result that does not represent the true structural features, but instead a structure built from the noise aligning against itself in a reinforcing manner [154]. This can be avoided by using starting references containing only low resolution

structural features, such as those that can be identified in the raw subvolumes, with high resolution information only being visible in the final structure after averaging [154].

Over-alignment and reference bias can be ruled out by running up two independent averages from a single set of data that has been divided randomly [154]. The two new data sets should be treated completely independently and if reference bias and over-alignment are not a problem then the two results should be identical [154].

CHAPTER 3: Architecture and Organization of the Ventral Disc Array

Introduction

Previous research completed by Holberton between 1974 and 1986 [61,62,63,64,65,91,92,93,94,95,124,125,126,158] provided information on the structure and composition of the ventral disc of *Giardia muris* and *Giardia lamblia*. Holberton established several important aspects of ventral disc organization and composition. Holberton studied thin sections of Giardia trophozoite cells using EM. He established that most of the ventral disc exists as a single layer of MTs with long MRs extending towards the dorsal surface [61,62]. Holberton was also the first to describe crossbridges between the MRs [63,95]. Holberton developed the detergent extraction technique, which was refined and applied in this study [61], to image negatively stained ventral discs, discovering that the MTs are organized into a right-handed overlapping spiral [61].

Thanks to the development of modern EM 3-D analysis methods, such as tomography [159] and montaging [160,161], multiple ventral discs were imaged and reconstructed in 3D. These reconstructions provided sufficient resolution to easily distinguish between the individual MTs and visualize the major structural features of the ventral disc, while maintaining the context of the intact array (Figure 3.1 and Figure 3.2). In total, six different ventral discs were imaged, reconstructed and modeled. The results presented below come from data obtained from all six ventral discs. To avoid confusion the same

ventral disc will be used as an example in the figures in chapters 3 and 4.

It is hoped that the information about the overall architecture and the arrangement of the MTs within the array will serve as a foundation and an accurate context for further study of the ventral disc. In addition to providing a full structural context this work will correct a few misconceptions that exist in the current literature.

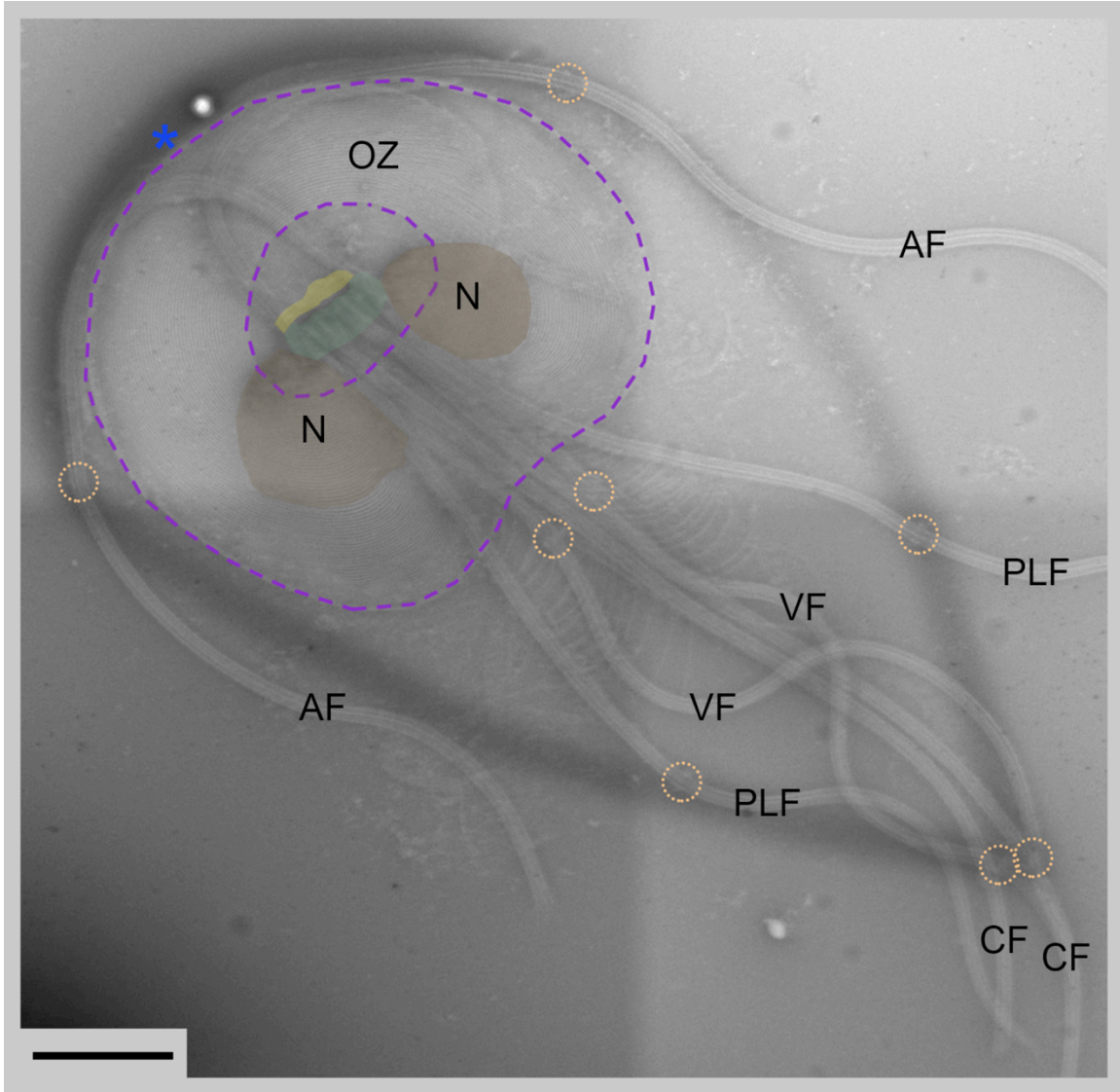


Figure 3.1: Extracted cytoskeleton and ventral disc of a *Giardia lamblia* trophozoite. A 2x2 montage EM image of an extracted cytoskeleton. A dark shadow was artificially added to the image to show where the outline of an intact cell would be. The ventral disc is outlined with a dashed purple line. The dense bands are colored yellow and the basal bodies are colored green. The nuclei are colored brown and labeled with N. The positions of the flagella pockets are outlined with light orange circles. The marginal plate is marked with a blue *. OZ = overlap zone, AF = anterior flagellum VF = ventral flagellum PLF = posterior-lateral flagellum CF = caudal flagellum. **Scale bar = 2 μm .** This image demonstrates how well most cytoskeletons survive extraction and how many of the components observed in intact cells still associated with one another in their native arrangement.

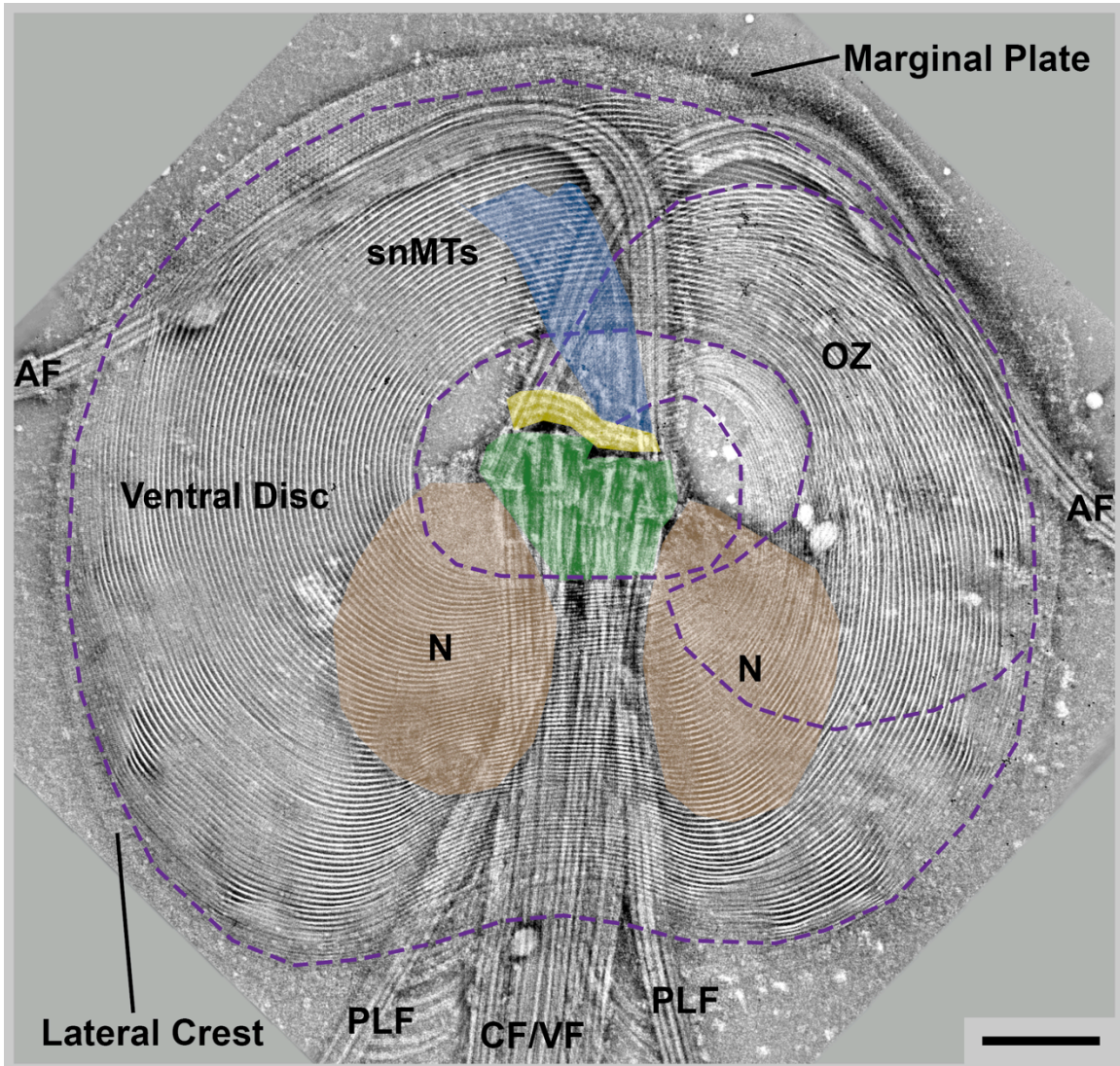


Figure 3.2: Extracted ventral disc of a *Giardia lamblia* trophozoite. 180 nm thick tomographic slice from a 4x4 montaged tomogram of an extracted and negatively stained ventral disc. The ventral disc is outlined with a dashed purple line. The nuclei (N) are colored brown. The basal bodies are colored green. The dense bands are colored yellow. The snMTs are colored blue. OZ = overlap zone, AF = anterior flagellum VF = ventral flagellum PLF = posterior-lateral flagellum CF = caudal flagellum. **Scale bar = 1 μ m.** Montaging has allowed a large $\sim 10 \mu$ m in diameter array to be imaged at a magnification height enough to resolve the individual MTs of the array and determine the overall architecture and organization of the ventral disc MTs.

Brief Materials and Methods

Giardia lamblia trophozoite cells were cultured and their cytoskeletons were gently extracted using a combination of detergent and physical stress from vortexing and sonication. The extraction protocol was optimized to reduce damage to the cytoskeletons, keeping as many components present and keeping the ventral discs as intact as possible (Figure 3.1), without the use of fixatives.

The cytoskeletons were negatively stained using aurothioglucose. The cytoskeletons were imaged at 18,000 X nominal magnification, so that individual MTs could be distinguished. A 4x4 montage was used so that the whole ventral disc could be visualized as a complete unit in a single tomogram. The tomogram was reconstructed and modeled using IMOD software. A single model contour was placed along the full length of each MT to allow as much information as possible to be extracted from the 6 disc models that were constructed.

Advantages and Limitations of Exaction of the Cytoskeletons and Preparation by Negative Stain

The use of negative stain allowed quick and easy preparation of the extracted ventral discs without the use of crosslinking fixatives. The negative stain also provided excellent contrast so that protein was easily distinguished from the background in most areas of the

ventral disc. In the tomograms the protein density is white in contrast and the background is dark. This enhanced certain features, such as the crossbridges, which are difficult to distinguish without high contrast (See chapter 4, Figure 4.2 and chapter 5, Figure 5.1).

A drawback to sample preparation with negative stain is the flattening of the protein structures, so that fine structural details cannot be observed. In the ventral disc, this resulted in a shortening of the MRs, and an alteration of the structural detail of the trilaminar sheets. Negative staining also meant that the side arms (a MT associated structure) could not be distinguished from the margin-facing wall of the MT.

Using extracted discs and imaging using a 4x4 montage tilt series allowed all the MTs of the disc to be imaged in a single tomogram. An alternative approach would be to section resin embedded cells and reconstruct tomograms of each section, eventually building up a complete 3D reconstruction of the ventral disc. However, due to the complexity of the array, it was not possible to accurately join the serial sections in Z (Cindi Schwartz: personal communication).

The use of extracted cytoskeletons does lead to some unavoidable structural changes in the ventral disc. The principal change is the loss of the domed disc conformation that can be observed in an intact cell [62,123]. During extraction the ventral disc flattens and some of the crossbridges may break [61]. It appears that flattening of the ventral disc causes some artifacts or “ruffling” in the MT in some areas of the disc (Figure 3.1 and Figure 3.4, panel A)

Results

Supernumerary Microtubules

The snMTs are MTs that are closely associated with the ventral disc (Figure 3.3), but do not form part of the main body of the disc. The function of the snMTs is unknown. It was previously thought that the snMTs are only present on a small percentage of ventral discs and possibly only present at certain times in the cell cycle [62,84]; however they were present on all of the discs imaged (N=8). Similar to the ventral disc MTs, the snMTs nucleate at the microtubule organizing centers of the disc, the dense bands (DB) (Figure 3.3). The DBs are strips of dense material organized into six curved bands (Figure 3.3, Panel C). Analogous MT organizing centers have been observed in other organisms in the Excavata kingdom, such as *Saccinobaculus* [51,52]. The dense material in this organism organizes the axostyle MTs [51,52]. The DBs in *G. lamblia* are arranged in two sets. This work has revealed that DB1, DB2 and DB3 always organize a large proportion of the ventral disc MTs (Figure 3.3, Panel A) and DB4, DB5 and DB6 always organize the snMTs (N=6) (Figure 3.3, Panel B).

Each set of DBs is arranged like stairs (Figure 3.3, Panel C). The capped MT minus ends are closely packed side by side on the dorsal surface of the dense material. The step-like arrangement of the DBs means that the MTs form three overlapping sheets. This right set of DBs, that organize the snMTS, are located to the right and ventral (under) relative to the left DBs. This means that the snMTs extend between the two layers of ventral disc MT that form the overlap zone, and not above the main body of the disc as previously

thought.

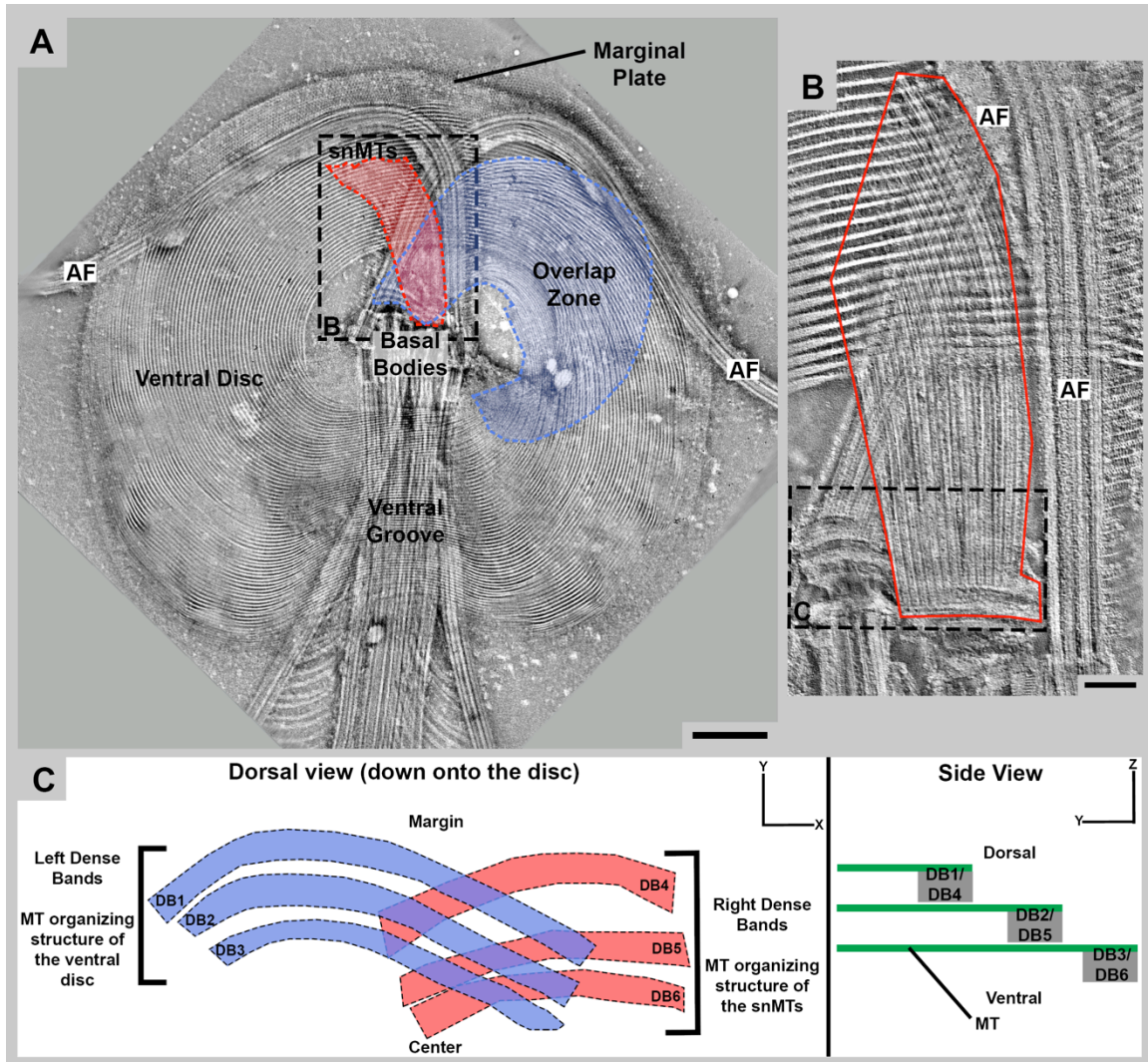


Figure 3.3: Location and organization of the snMTs. Panel A: The location of the snMTs in relation to the main body of the ventral disc. The snMTs are outlined with a dashed red line. The Overlap zone is outlined with a dashed blue line, and has been highlighted to illustrate the difference in location, size, and shape from the snMTs. The black dashed line shows the location of panel B. **Scale bar = 1 μ m.** **Panel B:** A zoomed in view of the DBs and snMTs (red outline). AF = anterior flagellum. **Scale bar = 500 μ m.** The left DBs (blue dashed outline) organize only ventral disc MTs. The right dense bands (dark blue dashed outline) organize the snMTs exclusively. The snMTs seem to mirror the organization of the ventral disc MTs, except that they extend between the two layers of the overlap zone, out towards the disc margin. Although there is some variability in the length, the snMTs were observed on all the ventral discs imaged (N=8). **Panel C:** A schematic diagram showing the organization of the DBs. The left DBs (blue), including DB1, DB2 and DB3, are slightly larger than the right DBs (red), including DB4, DB5 and DB6. The left DBs are also located above (dorsal) to the right set. The right side of the panel shows the stair-like arrangement of the MTs (green) projecting from the three dense bands (grey) of both sets.

The snMTs roughly track the curvature of one of the anterior flagella that also extends

out between the layers of the overlap zone. The MTs of DB1, DB2, and DB3, and those of DB4, DB5, and DB6, are approximate mirror images though they are spatially translated (Figure 3.3). However, the snMTs remain in three overlapping layers and do not fan out into a single layer like the ventral disc MTs. The snMTs terminate much earlier (Figure 3.3, Panel A) than the MTs of the main body of the ventral disc and do not take on more extreme curvature like the MTs of the dorsal layer of the overlap zone (Chapter 4, Figure 4.4).

The fact that the snMTs do not spread out into a single layer made accurate modeling of the individual MTs impossible. The MTs in this region were so densely packed that stain penetration was relatively poor, reducing contrast. Also, there was so much tightly packed material in this area that interpretable image detail was somewhat compromised, due to the increase in sample thickness.

However, it was still possible to visualize the edge of the snMTs and to determine how far they extended (Figure 3.3, Panel A). The lengths observed between the six discs were variable, but the snMTs never extended beyond the margin of the disc. In fact, because they are so short, the snMTs cannot account for the large area previously observed by fluorescence confocal microscopy [121] (Chapter 1, Figure 1.9). The large structure observed was in fact the overlap zone (Figure 3.3, Panel A). The overlap zone is a much larger structure that extends around to the ventral groove. This is important to note as DAPs previously classified as localizing to the snMTs [121] more likely localized to one or both layers of the overlap zone.

The Architecture and Organization of the Main Body of the Ventral Disc

Although various aspects of the ventral disc have been studied in the past, the overall arrangement of the MTs in the large array of the disc has not been determined until now (Figure 3.4).

Large Scale Architecture of the Ventral Disc MTs

All of the ventral discs that were modeled (N=6) formed a right-handed spiraling array, which agrees with previous studies [61,62]. With the exception of the area very close to the DBs, where three layers of MTs can be observed, the ventral disc is composed of a single sheet of MTs that spirals around and passes under itself. The ventral disc array is a highly organized structure: once a single layer of MTs is formed in the dorsal (upper) overlap zone no MT crossing over of the MTs can be seen. This is consistent with what Holberton described in the MT/MR complexes: the MTs are connected and spaced out by crossbridges that exist between neighboring MRs [61,62,63].

There are rare instances where MTs come very close or slightly overlap in the regions where “ruffling” in the extracted disc is observed. This crossover is transient and does not

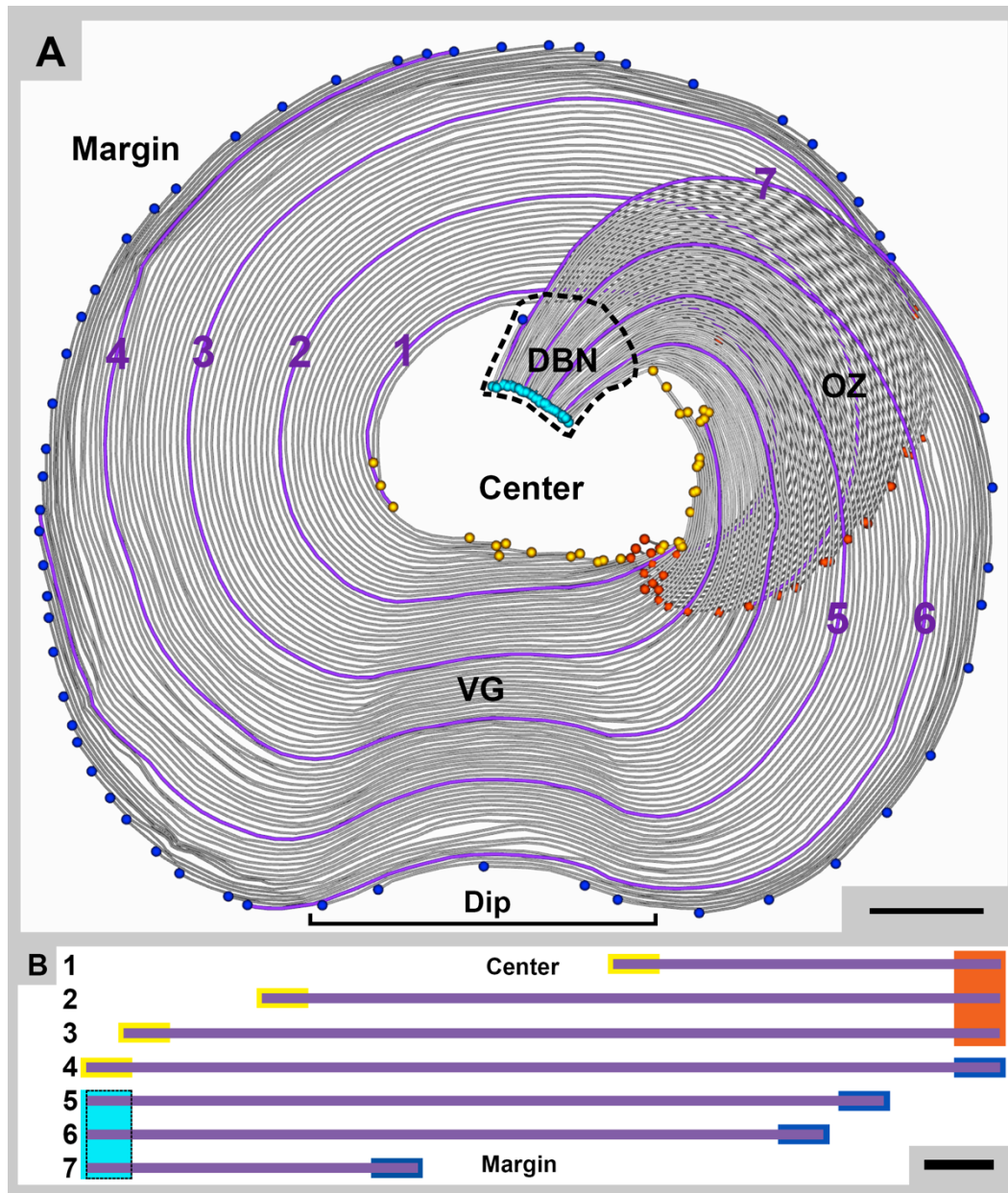


Figure 3.4: Architecture of the ventral disc. Panel A: A model of all the MT/MR in the main body of the ventral disc shown in Figure 3.1. Each line is a single MT. DBN = dense band nucleation zone, OZ = overlap zone, VG = ventral groove. The light blue spheres mark MTs that nucleate at the dense bands. The yellow spheres mark MT that nucleate in clusters on the center edge. The dark blue spheres mark MT plus ends that terminate at the disc margin. The orange spheres mark MT plus ends that terminate in under another part of the disc. The dashed black line represents an area of uncertainty in the model. In that region the MT were so densely packed that the individual MTs could not be distinguished from one another. The model was extended to the most distal dense band along its previous trajectory to get the best estimate of length possible. The purple lines are seven example MTs that have been selected to be shown in greater detail throughout chapters 3 and 4. They will be a guide to orient the reader in this complex structure. They have been numbered 1 to 7 from the center to the margin. **Scale bar = 1 μ m.** **Panel B:** The purple lines represent the relative lengths of the example seven MTs. The colored boxes indicate where they nucleate and terminate. Yellow = center edge, light blue = dense bands, orange = ventral overlapping surface, dark blue = margin. **Scale bar = 1.3 μ m.**

continue to other areas in the structure (Figure 3.4, Panel A). It is believed that these areas of crossover are an artifact from the extraction process and result from a relaxation of the disc when the domed conformation is lost.

Structural features of the ventral disc: the overlap zone

The area formed where the ventral disc spirals under itself is known as the overlap zone (Figure 3.3, panel A and Figure 3.4, panel A). The single sheet of MTs passes around and under to form two completely distinct layers that are not interwoven. The two layers are known as the dorsal overlap zone (upper, near the start of the spiral) and the ventral overlap zone (lower, at the end of the spiral). The overlap zone was previously thought to be a relatively small structure where the MTs spiral overlapped just enough to close the dome. In fact, there is an extensive area of overlap that composes close to 30% of the ventral disc on average (N=6) (Chapter 4, Figure 4.1, Panel B). The ventral overlap zone extends under and around the disc (Figure 3.4, Panel A). However, the exact point of termination and extent of curvature was one of the more variable aspects between the six ventral discs examined. Two of the six ventral overlap zones terminated just prior to the ventral groove, two terminated at the start of the ventral groove and two extended beyond the ventral groove towards the basal bodies and terminated in the center of the ventral disc (data not shown).

The variation in size and shape of the ventral surface of the overlap zone may be natural or another artifact of extraction. No structural connections were observed between the dorsal and ventral overlap zones in either the negative stained ventral disc tomograms or

those that were imaged using cryo-ET (Chapter 5, Figure 5.1). It is then possible that the shape of the ventral overlap zone is maintained purely by curvature of the MTs and/or the crossbridges between the MRs. Because the ventral layer of the overlap zone is not anchored directly to the rest of the array, it might experience slightly more damage from physical stress during extraction. This damage leads to breakage of the long crossbridges that exist between the widely spaced MRs (described in Chapter 4), which could result in a tendency for this area to shift and deform slightly during extraction.

Structural features of the ventral disc: the ventral groove.

The ventral groove is a region of the ventral disc that passes under the ventral, posterior-lateral and caudal flagella. In the domed disc, this area dips down and around the flagella. In the six extracted ventral discs, the majority of the dip in Z was lost when the doming relaxed, even though the flagella were still present and located over this region. The characteristic curving of the MTs towards the center of the disc and the close packing of the MTs/MRs is still maintained (Figure 3.4, Panel A).

Structural features of the ventral disc: the disc margin.

The outer edge of the ventral disc is known as the margin [84]. In the domed structure in an intact cell, the margin is steeply sloped and is composed of 4 to 9 MTs on the outer edge of the array (Figure 3.5, Panel A). When viewed in cross-section [62], the MTs are staggered relative to their neighbors. The domed ventral disc does not have a uniform curvature; it is shaped more like a Frisbee, flatter in the center and steeply sloped at the marginal edges [62]. The marginal edge is one of the most robust structural features in

the ventral disc, with close packing of the MTs being maintained in the extracted discs (Figure 3.3, Panel A), likely by extensive crosslinking by larger and thicker crossbridges [84].

Number, Length and Organization of MTs within the Ventral Disc

Array

The ventral disc was previously estimated to contain ~50 MTs [84] determined by counting the MTs in a cross section. In fact, it was found that the main body of the disc is composed of an average of 95 ± 5 individual MTs, which is almost double the previous estimate. The ventral disc shown in Figure 3.4, panel A contains 94 MTs (N=1). In order to form the disc spiral, MTs terminate at regular intervals around the margin (Figure 3.4, Panel A). It is therefore not possible to gain an accurate count of the number of MTs in the disc from a single cross section.

In order to form the spiral from a single sheet of MTs, and also to achieve a roughly circular disc, the MTs of the disc vary substantially in length depending on their position in the array. Seven MTs (Figure 3.4, colored purple in panel A and panel B) that are evenly spaced throughout the ventral disc (N=1) were chosen to provide a simplified example of the MT length trends that can be observed in the ventral disc.

The length of each MT in the six discs was determined by accurately modeling the

MT/MR complex from its minus end to its plus end. The excellent contrast provided by the negative stain meant that it was easy to distinguish between each individual MT in all areas of the ventral disc, except near the DBs. In this area, there are three layers of MTs that are very densely packed, leading to poor stain penetration. This issue was compounded by the additional material of the DBs, the snMTs and the ventral overlap zone, increasing the thickness of the sample. This made it impossible to accurately follow the path of the individual MTs near the DBs.

In order to gain a better estimate of length, each MT was modeled in a plus- to minus-end direction in the dorsal overlap zone to the point where it entered three layers near the DBs. The contour was then artificially extended to the nucleation sites on DB3, along the trajectory at which it entered the three layers. The distance between the three DBs was measured at multiple locations and the mean average was determined. The result was then subtracted from the length of each contour in this region, so a more accurate estimate could be made of total MT length, assuming that an approximately equal number of MTs nucleated at DB1, DB2, or DB3. The average length uncertainty was 84 ± 4 nm (N=6), which is relatively small compared to the total length of each ventral disc MT (Figure 3.4, Panel B).

The longest MT from each disc extends from the DBs and terminates at the anterior of the disc, in the margin, just before it passes under itself to form the ventral overlap zone. The longest MT in the ventral disc (figure 3.4, panel A) is located between example MT3 and MT4 (Figure 3.4, Panel A). The average length for the longest MT is 18.36 ± 0.75

μm (N =6). This is ~ 1.2 times longer than the cell itself, based on a $12 \mu\text{m}$ estimate of cell length [162].

The shortest MT in the ventral disc is usually located either on the center edge (33% of the ventral discs) or in the dense bands nucleation zone right up against the anterior flagella (50% of the ventral discs). In one disc the shortest MT was located in the middle of the main body of the disc (17% of the ventral discs) (N=6). This was either the result of a rare MT that nucleates in an atypical location or a rare broken MT that was damaged during sample preparation.

The average total length of MT in the main body of a ventral disc, accounting for DB uncertainty, is $1.23 \pm 0.05 \text{ mm}$ (N=6) (Table 3.1). To put this in context, this is the length of ~ 102 trophozoite cells (from head to tail of the tear drop) arranged end to end. The highly organized array packages a total of 1.22 mm of MT to be packaged into a disc that, in an intact cell, is approximately 6 to $8 \mu\text{m}$ in diameter. The large amount of protein (tubulin, MRs proteins and DAPs) that is needed to build a structure this large represents a significant investment of cellular resources and emphasizes the importance of this structure to the trophozoite form of *Giardia*.

The Organization, Location and Morphology of MT Minus- and Plus-ends in the Ventral Disc

There are two principal sites for MT nucleation in the ventral disc, at DB1, DB2 and DB3, and on the center edge of the array. The DBs are where 59 % (N=6) of MTs nucleate. The minus ends are arranged side by side on the DBs and have a capped morphology [44,84]. The capped ends narrow to a point (Figure 1.5), which is rounded by the stain condensation (Figure 3.5, panel C).

The second site for MT nucleation is on the center edge of the disc (Figure 3.5), where 39% (N=6) of the MTs originate. In this area, the MTs nucleate in small clusters. The morphology of the center edge minus ends is different from the capped minus ends observed at the DBs. In the negative stain long tapered ends can be seen (Figure 3.5, panel D). These structures result from the stain condensation of blunt minus ends with an overhanging MR. This morphology was first observed by Schwartz, C. et al., 2012 [84]. Until this work, it was not known that the blunt MT minus ends that have overhanging MR are located exclusively on the center edge.

Lastly, 2% (N=6) of MTs appear to nucleate in the main body of the ventral disc. This category includes MTs that nucleate in the main body of the disc and rare broken MTs that were shorn during sample preparation.

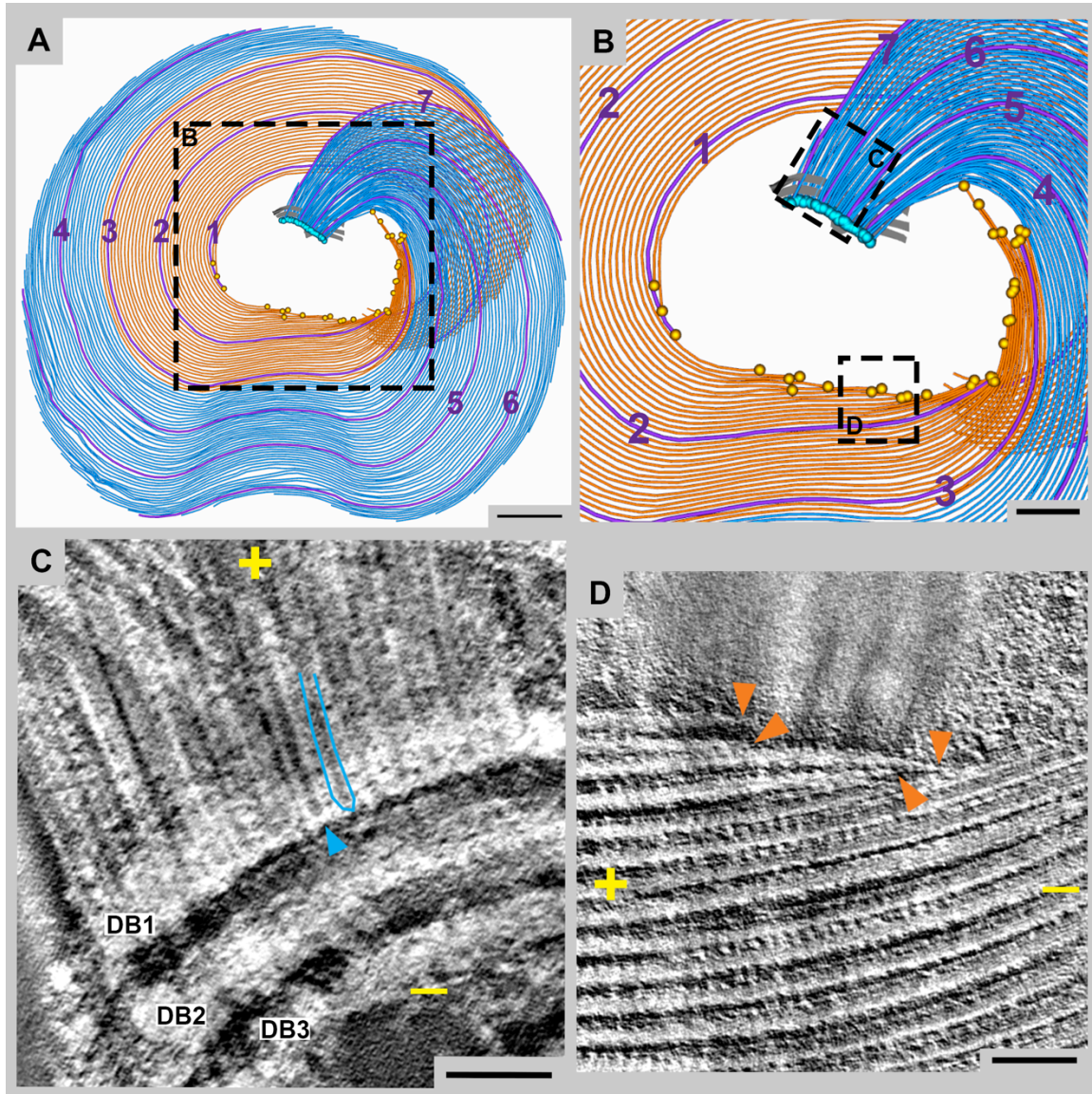


Figure 3.5: A closer look at the location and morphology of the nucleation sites of the ventral disc MTs. **Panel A:** The model has been colored to show how the location of MT nucleation and MT termination are related. The dense band nucleating MTs (blue) terminate in blunt ends at regular intervals around the margin. The center edge nucleating MTs (orange), terminate under the dorsal overlap zone and form the ventral layer of the overlap zone. The example MTs are labeled 1 to 7 (purple). **Scale bar = 1 μ m.** **Panel B:** A zoomed in view of the two nucleation zones in the model. The left and right sets of dense bands (grey) form two MT organizing centers. The left set nucleate the blue ventral disc MTs, The dashed lines represent the locations of panels C and D in the model. **Scale bar = 500 nm.** **Panel C:** An example of MT organization at the left dense bands in a 24 nm thick tomographic slice. The MTs nucleate side by side, (example marked with a blue outline and a blue arrow) on top of the dense material. The dense bands are staggered like stairs (DB1 top, DB2 middle, DB3 bottom), so that three layers of MT are created. The three layers fan out to form the single layer of the ventral disc. The polarity of MTs is marked with a yellow plus and minus symbols. **Scale bar = 50 nm.** **Panel D:** An example of the clusters of center nucleating MTs in a 24 nm thick tomographic slice. The polarity of MTs is marked with yellow plus and minus symbols. The minus ends appear to taper to a point (marked with orange triangles), the taper is due to the overhanging MR that extends beyond the blunt minus end of the MT (see Figure 1.5). **Scale bar = 50 nm.**

Nucleation sites relate to the location of termination

The principal sites of nucleation (DBs and center edge clusters) correlate closely with the sites where microtubules terminate at their plus-ends (Figure 3.5, Panel A). 59 % (N=6) of MTs nucleate at the DBs and 58 % (N=6) terminate at regular intervals around the margin of the disc in blunt plus ends. The DBs MTs, colored blue in Figure 3.5, go on to form the vast majority of the margin around the disc (Figure 3.5, Panel A).

39% (N=6) of MTs nucleate on the center edge in clusters and 41% (N=6) terminate in the ventral surface of the overlap zone, also in blunt plus ends. The vast majority of the ventral surface of the overlap zone is made up of center edge nucleating MTs (Figure 3.5, Panel A). This is potentially a significant result because the deletion of the center edge MTs from the models almost completely removed the ventral overlap zone and correlates well with the phenotype observed upon knockdown of MBP expression [123]. MBP is the only DAP knockdown discovered thus far that causes an impaired attachment of the trophozoite cell.

The disc phenotype observed upon MBP knockdown was previously described as open, as it was thought that the “small” overlap zone in the disc had “opened” to produce a horseshoe like shape [123] (Chapter 1, Figure 1.10). However, it is unlikely that this description is accurate. It is now known that the overlap zone is a much larger structure that previously thought. The MBP knockdown discs do not show a significant increase in the diameter of the array or a displacement of the ventral surface of the overlap zone that would have occur upon the “opening” of such an extensive structure.

Instead, the conformation observed after anti-MBP Morpholino treatment could be explained by two phenomena. The first is the complete loss of the center edge MT from the ventral disc, resulting in the loss of the entire ventral overlap zone surface and a flattening of the array. The second is the loss of the MRs from the center edge MTs. Beta-giardin-GFP was used as a ventral disc marker in the study [123]. It was, therefore, not possible to distinguish the loss of MTs from the loss of MRs. Loss of the MRs from the center edge nucleating MTs might still result in a flattening of the array.

In either case, MBP could provide a very promising drug target. MBP is unique to *Giardia* and its knockdown impairs attachment [123]. Ideas for testing this hypothesis are described in chapter 6.

Summary of Results and Discussion

The use of montaging and electron tomography allowed the complete ventral disc array to be imaged and reconstructed in 3D at a higher resolution than any previous study. The high contrast and high-resolution sample allowed a model of the arrangement of all MT/MR complexes to be constructed for six individual ventral discs. This model has provided new information on the quantity and length of MTs present, the morphology of ventral disc structures and the organization of MT nucleation in the array. This work has also served to correct a few misconceptions that have existed in the literature until now. The results of this chapter are summarized in Table 3.1.

Aspect of Ventral Disc	Literature	This Work
snMTs	large structure, rare	small structure, nucleates at DB4, DB5, DB6, on every disc examined
Overlap Zone	small structure: actual overlap zone was mistaken for snMTs	Large structure that constitutes 33% of the ventral disc array and extends from the left dense bands to the ventral groove.
MT number	~ 50	95 ± 5
Total MT length	unknown	1.23 ± 0.05 mm
Sites of MT nucleation	at dense bands and around the disc: specific organization unknown	The ventral disc MTs nucleate at two principle sites: at DB1, DB2 and DB3 and in clusters on the center edge.
Ventral Overlap Zone	no specific details	majority of ventral surface formed by center edge nucleating MTs

Table 3.1: A summary of the key results from Chapter 3 and how they relate to the current literature on ventral disc structure.

CHAPTER 4: Regions of the Ventral Disc

Introduction

In 2011 the Dawson Laboratory at UC Davis published work that demonstrated that the localization of MAPs (known as DAPs in the ventral disc) that associate with ventral disc MTs was not uniform across the array [121]. The results of the extensive fluorescence microscopy study revealed that there were common patterns of DAP localization across the ventral disc. This allowed the proteins to be classified by the area or region of the disc in which they were observed. Excluding flagella localization, they saw four major patterns: localization to the whole disc; localization to the marginal edge of the disc or lateral crest; localization to ventral groove or excluding the ventral groove; and lastly, localization to the overlap zone (which was originally mistaken for the snMTs in the published paper [121]). The natural continuation of this work was to examine the ventral disc regions revealed by GFP tagging to determine if structural differences could be observed.

The six ventral disc tomograms provided the first opportunity for comparison of these areas in a high-resolution reconstruction of a complete ventral disc. Holberton established that there is a basic structural unit of the ventral disc consisting of the MT, the MR and crossbridges [61,62,63,64], which was confirmed by Schwartz, C. et al, (2012), who demonstrated the same structure with more detail and improved resolution [84]. When

the tomograms were examined it was found that there were obvious differences between distinct regions of the ventral disc.

The different regions of the ventral disc were found to have different MR and crossbridge morphologies, variation in curvature of the MT/MR complexes, and differences in the lateral spacing of adjacent MTs. The regional variation was consistent across the six ventral disc tomograms that were examined. The structurally divergent regions localized the large structural features of the overall array and showed approximate correlation with the patterns observed with fluorescence microscopy. The improved resolution obtained from ET allowed six different regions to be identified.

Results

Based on characteristic differences in MT spacing, MT/MR curvature, and the length and morphology of the MRs and crossbridges six structural distinct regions were identified. These are: the dense bands nucleation zone (DNZ), the dorsal overlap zone (DOZ), the disc body, the ventral groove (VG), the ventral overlap zone (VOZ), and the margin (Figure 4.1, Panel A).

Location of the Regions

The six structurally distinct regions localize to specific areas of the ventral disc (Figure 4.1, Panel A). The first region is the DNZ. This region includes the MTs that extend from the DBs MT organizing center to the area where the MTs fan out from three layers into a single layer. This is the smallest region of the ventral disc, composing 5 % (N=6) of the total MT length (Figure 4.1, Panel B).

The Dorsal Overlap Zone is the second largest region in the ventral disc, composing 17% (N=6) of the total MT length (Figure 4.1, Panel B). The DOZ begins at the point where three layers fan out to form a single layer (Figure 4.1, Panel A). The MTs in this layer pass over those of the VOZ and usually extend around close to or up to the VG (dip in the ventral disc where the flagella pass over the array (Chapter 3, Figure 3.4, Panel A). This region also includes some center edge nucleation clusters (Chapter 3, Figure 3.5).

The disc body is the largest region in the ventral disc, composing 40% (N=6) of the total MT length (Figure 4.1, Panel B). Schwartz, C. et al. (2012) used cryo-ET, combined with subvolume averaging of the disc body, to obtain the first high-resolution structure of a repeating unit that composed the ventral disc [84]. The disc body is divided into approximately two halves by the VG and is the only region to exist as two separate parts (Figure 4.1, Panel A).

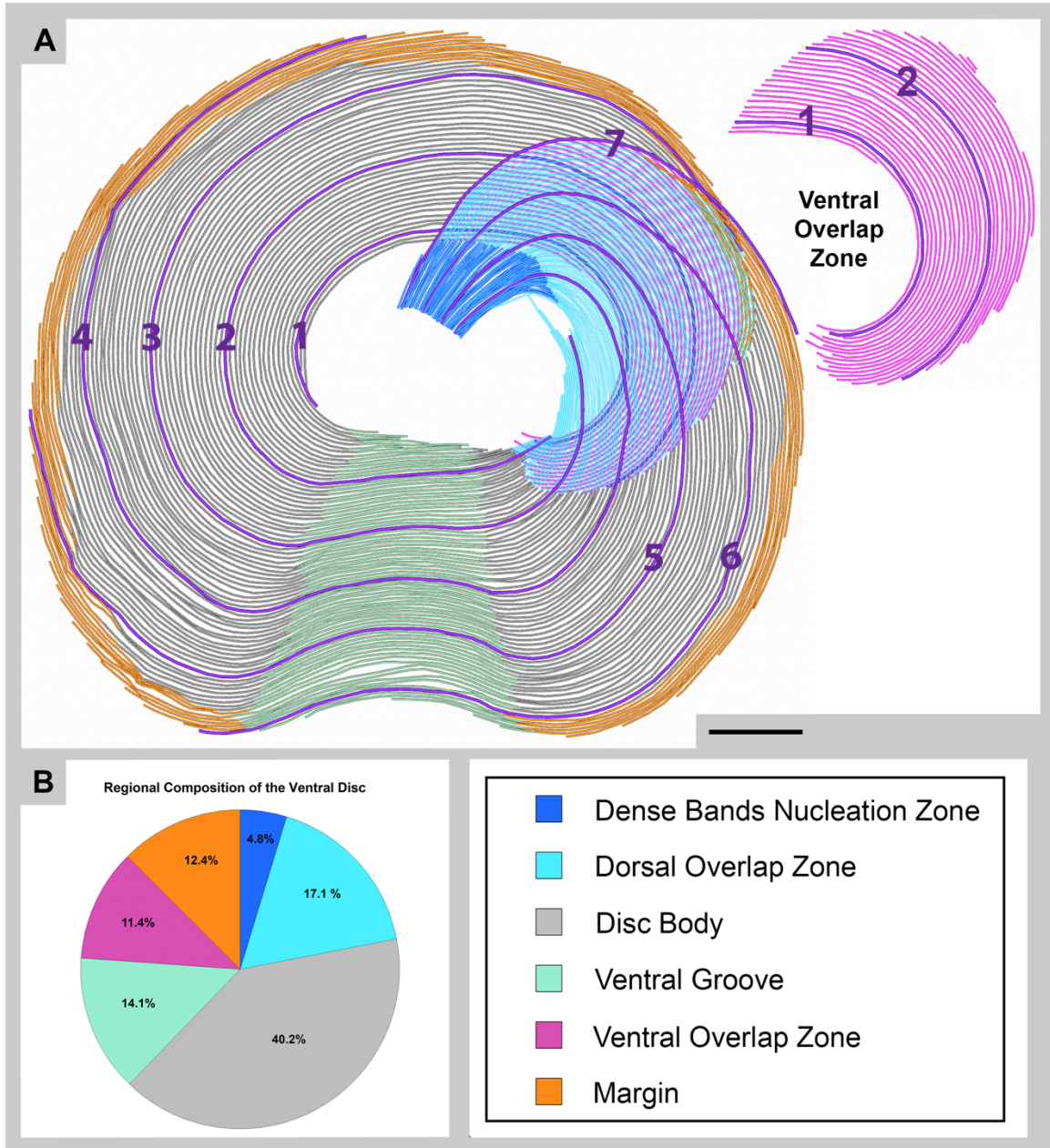


Figure 4.1 Regions of the ventral disc. Panel A: There are six structurally distinct regions in the ventral disc. The locations of these regions in the ventral disc are represented by different colors in the model, the regions are: Dense Bands Nucleation Zone (blue), the Dorsal Overlap Zone (cyan), Disc Body (grey), the Ventral Groove (green), Ventral Overlap Zone (pink), and the Margin (orange). The VOZ is formed when the ventral disc curves under itself and is located under the DOZ. It has been displayed to scale on the right of the main disc for clarity. The seven example MTs (purple) are labeled 1 to 7. **Scale bar = 1 μ m.** **Panel B:** Shows the percentage regional composition the ventral disc (N =6) by MT length.

The VG is located in the middle of the disc body (Figure 4.1, Panel A). In the VG, the ventral disc MTs pass under three pairs of flagella. In the intact cell, the array has a 3D

dip in the VG. In the extracted ventral disc, the 3D structure is lost but a 2D dip is still maintained. The VG makes up 14% (N=6) of the total ventral disc structure (Figure 4.1, Panel B).

The two regions where ventral disc MTs commonly terminate are the VOZ and the margin, both of these regions are equal in total size and each make up 12% (N=6) of the total MT length (Figure 4.1, Panel B). As discussed in chapter 3, the VOZ is formed almost entirely from the center edge nucleating MTs. The VOZ is the only region of the disc located under another region (Figure 4.1, Panel A).

The margin is composed of 4 to 8 MTs at the outer edge of the ventral disc (Figure 4.1, Panel A). It is the region where the majority of MTs terminate at approximately regular intervals. In an intact cell, the MTs are staggered relative to each other to form the edge of the shallow dome [62].

Characteristic Regional Spacing and Morphology

As stated in the introduction, the six ventral disc regions were defined by structural differences. In this section the differences in MT spacing as well as MR and crossbridge morphology observed in the negative stain tomograms will be described in detail (Figure 4.2).

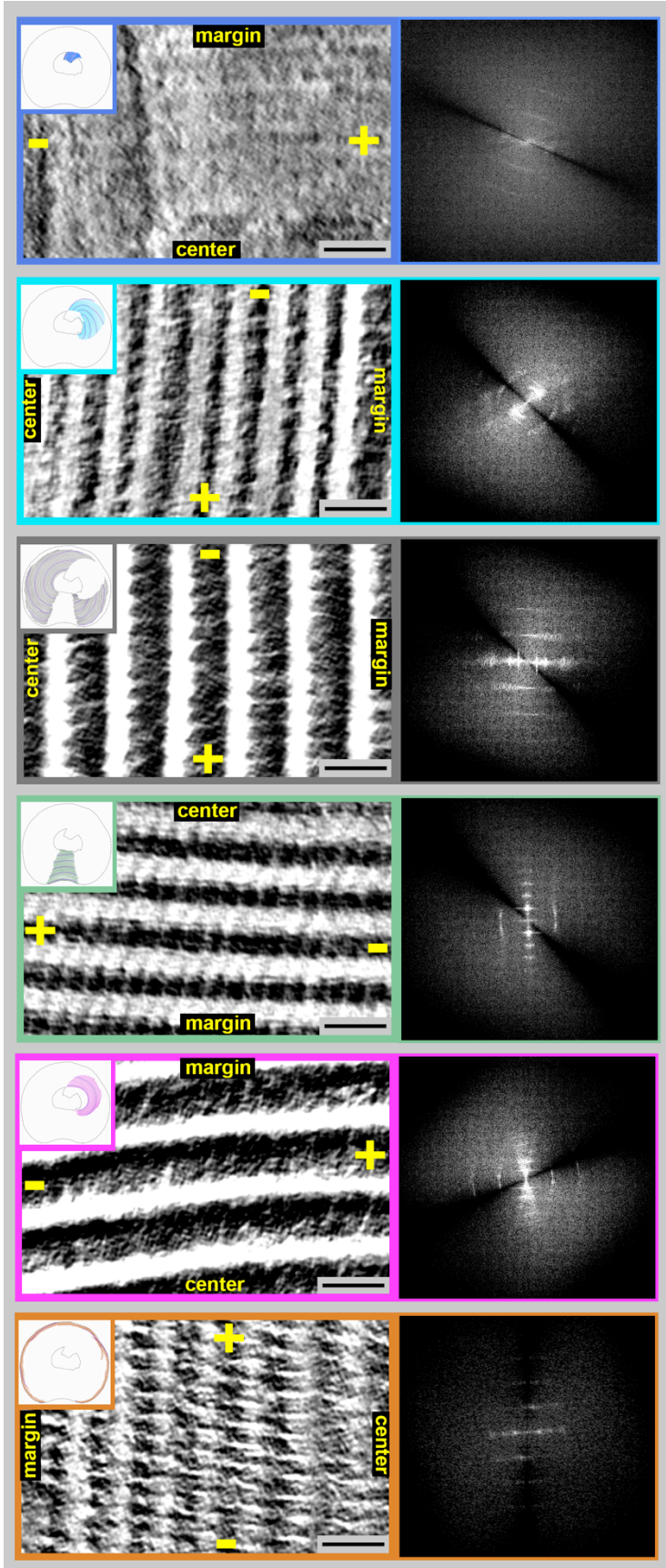


Figure 4.2: 24 nm tomographic slices from six ventral disc regions (left column) and power spectra obtained from larger longitudinal sections through the MRs at each region showing the repeating structures in reciprocal space (right column). The X, Y tomographic slices from the six regions are shown in the colored boxes on the left. **Scale bar = 50 nm.** The colors are as follows: dense bands nucleation zone (blue), dorsal overlap zone (cyan), disc body (grey), ventral groove (green), ventral overlap zone (pink) and margin (orange). All of the tomographic slices are longitudinal sections through the MRs, with the exception of the DNZ where there are no MRs, so a longitudinal section through the MTs is shown. Each box is labeled with “margin” and “center” to indicate the direction of the center and margin edge of the ventral disc. Each box is also labeled with a “+” and “-” to indicate the polarity of the MTs. The power spectrum for each region is shown on the right. The major lines in each spectrum represent the repeat distances the crossbridges and other MT and MR features, in the direction along the MT, in reciprocal space. From inner to outer these lines are 1/16 nm, 1/8nm, 1/6 nm. The distance between the MR, and the length of the crossbridges connecting them is located in a direction perpendicular to the major lines. The line closest to the center of the spectra gives this distance in reciprocal space. The distances between MRs are: DOZ distance = ~32 nm, disc body distance = ~54 nm, VG distance = ~37 nm, VOZ distance = ~54 nm, margin distance = ~35nm.

Dense Bands Nucleation Zone

All regional examples shown in Figure 4.2 are pictured at the MR height, with the exception of the DNZ (Figure 4.2, blue box), where a longitudinal section through the MTs is shown. Where the MTs nucleate, close to the DBs, no MRs were observed. As the MTs begin to spread out into a single layer, very short MRs can be observed. No indications of crossbridges could be seen either between the very short MRs or the between the MTs.

The MT packing in the DNZ is unique. At the DBs the MTs are very closely packed so they are arranged side by side, with no space detectable space between them. The MTs are organized in three staggered layers, as discussed in chapter three and shown partially in Figure 4.2, blue box). This is the only place in the disc where the MTs are traveling in the same direction and are arranged on top of one another in multiple layers. As the MTs of the DNZ continue towards the DOZ they begin to separate and fan out to form a single layer. The MTs are still so densely packed in this region that it was not possible to model each individual MT with 100% accuracy and their exact organization as they spread out to form a single layer is still unknown.

Dorsal Overlap Zone

The MTs of the DNZ transition into the DOZ (Figure 4.2, cyan box). In the DOZ, the height of the MR increases once the MTs form a single layer. The MRs are tall and straight in most of this region. The MRs are still packed close together in the DOZ with a spacing of ~32 nm between them (Figure 4.2, power spectra, cyan box). The MTs

gradually become more widely spaced as they curve around the disc, spreading out from the marginal side. The MTs on the center edge do not become widely spaced until the disc body. The crossbridges between the MRs in the DOZ are short and wide at both sides of the MR. According to the power spectrum of this region, the crossbridges occur at a frequency of 16 nm. Most of the DOZ MTs transition into the disc body, however on some ventral discs the DOZ MTs were observed transitioning directly into the VG.

Disc Body

The first area of the disc body is located directly after the DOZ. The MTs in this region are widely spaced and have tall and regular MRs, that are 54 nm apart (Figure 4.2, grey box). Long crossbridges are observed between the MRs at 16 nm frequency (Figure 4.2, power spectra, grey box). The crossbridges appear to be wider at the margin side of the MR, narrowing and tapering as they connect to their neighbor. The disc body is separated into two areas by the VG (Figure 4.1, Panel A).

Ventral Groove

In the intact cells, the VG forms a 3D channel where the ventral disc MTs dip down and under six flagella. In order to accommodate the flagella, significant structural changes occur in the VG. The 3D shape of the VG is lost in the extracted disc, but the position of the flagella and the 2D curvature indicate where it would have existed. In order to accommodate the 2D dip at the posterior edge of the ventral disc, the disc body MTs must pack close together as they enter the ventral groove (Figure 4.2, green box). The spacing between the MRs in this region is ~37 nm (Figure 4.2, green power spectra).

The MRs in the VG are shorter and the crossbridges are very regular and still occur at intervals of 16 nm. The crossbridges extend at an angle to connect to the neighboring MR (Figure 4.2, green box). The MTs pass through the VG and then transition into the second disc body section (Figure 4.1, Panel A).

The shorter MRs in the VG might mean that there is less available height for crossbridges to exist, linking the neighboring MRs together. This might account for an artifact of extraction, which tends to occur in this region. The MTs near the marginal edge of the ventral groove tend to separate slightly. It is believed this occurs due to the stress of extraction [61] and would not occur in an intact cell, since this does not occur in a regular manner throughout the six ventral discs.

Ventral Overlap Zone

The second disc body section transitions into the VOZ as it passes under the dorsal layer of the ventral disc (Figure 4.1, Panel A). The MTs of the VOZ are widely spaced and the MR are ~54 nm apart (Figure 4.2, pink box). The MRs decrease in height throughout the region and can become as short as 20 nm (Figure 5.1, Panel E), which is shorter than the diameter of the MT. The crossbridges appear to be more irregular, but a repeat frequency of 16 nm is still obtained from the power spectrum. The irregularity of the crossbridges may be due to extraction and breakages, as this region can sustain more damage than the rest of the extracted ventral disc.

Margin

The disc margin is one of the most distinct regions of the ventral disc. It consists of 4 to 8 MTs on the marginal edge of the array. As MTs transition to the margin there is a dramatic change in the structure of the MR and crossbridges (Figure 4.2, orange box). The crossbridges are large and regularly spaced. They appear to extend on top of the MR in the negative stained discs, however, the cryo-ET and subvolume averaging carried out by Cindi Schwartz indicates that, in fact, the MRs are angled relative to the MTs and are no longer perpendicular to the MTs in the extracted array (manuscript in preparation).

The MT are closely packed in this region, with a MR spacing of ~ 35 nm. The crossbridges in the margin are thicker than in the rest of the ventral disc. A 16 nm repeat pattern can still be seen on the power spectra (Figure 4.2, power spectra, orange box), indicating that the axial crossbridge repeat constitutes a conserved feature across the entire ventral disc.

The margin is the termination point for many of the MTs from the multiple regions of the ventral disc, including the DOZ, the disc body, and the VG. The VG has an area that is margin-like in the way the MTs are arranged, but the distinctive crossbridges were absent, so those MTs were included as part of the VG and not the margin region.

Patterns of MT Curvature within the Ventral Disc

MT curvature is known to be altered by MAP decoration. *In vitro* experiments have

demonstrated that MTs decorated with motor proteins are straighter and more rigid than those without decoration [163]. Knowing that differential DAP localization exists across the ventral disc, it was essential to examine MT curvature in the disc regions that were identified.

The extent of MT curvature was determined by fitting a circle to each point of the model contour of each MT (Figure 4.3). The circle was fitted to 1750 nm of the contour line around the central model point, the smaller the fitted circle the more tightly curved the MT. 1750 nm around the central point was required to yield smooth sections of curvature. The radius of the fitted circle has an inverse relationship with degree of curvature of the MT around that particular point. For ease of understanding, the curvature values are presented as Kappa (K). $K = 1/r$ and is directly proportional to the tightness of curvature.

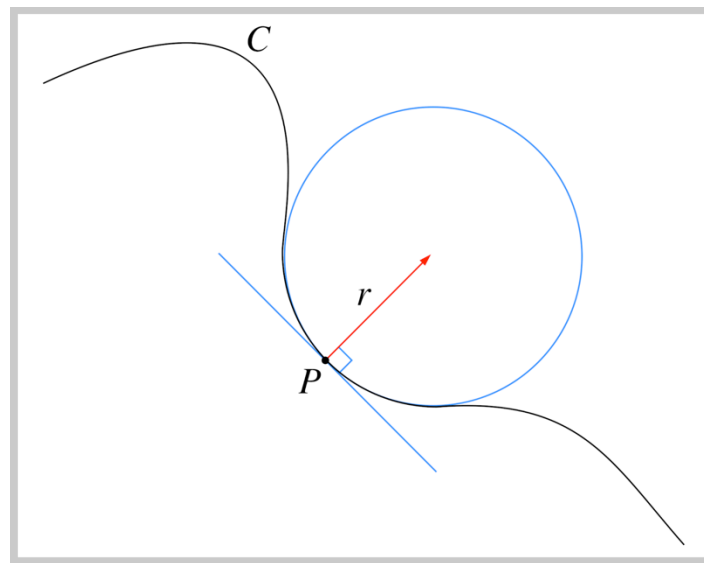


Figure 4.3: The method by which curvature of the ventral disc MTs was determined. C = model contour of a MT, P = model point, r = the radius of the circle fitted to the contour around each point, the more tight the curvature of the MT, the smaller the radius of the fitted circle. In order to give an easier to understand result, curvature is then presented as a Kappa value, where $K = 1/r$. Kappa is directly proportional to increasing curvature.

Curvature across the ventral disc array

A heat map of MT curvature was produced by coloring the model of the ventral disc MTs according to the curvature values obtained for each model point (Figure 4.4). The DNZ has been omitted from this analysis as the path of each MT could only be approximately determined in this section of the model.

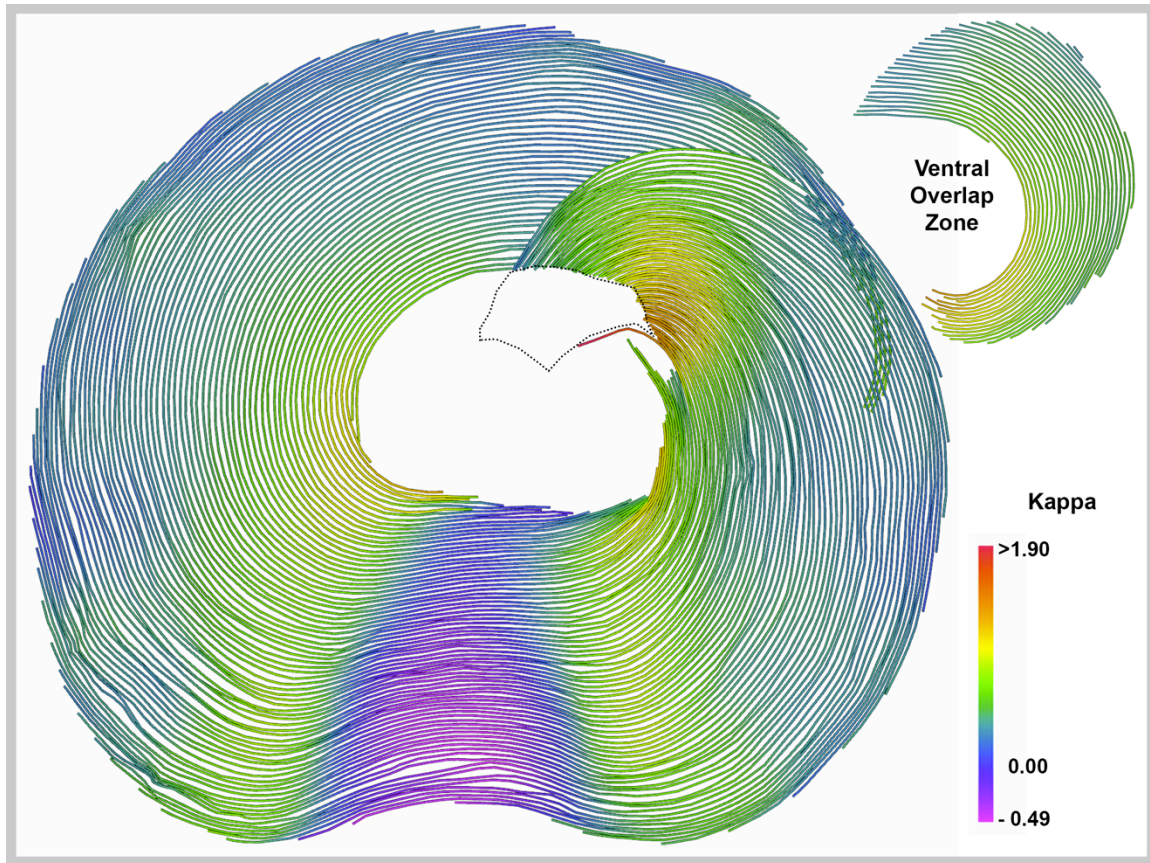


Figure 4.4: MT curvature at different regions of the ventral disc represented in a heat map. The extent of curvature at each point of the MT contour is represented by color and corresponds to the Kappa value ($1/\text{nm}$) at each point. Within the ventral disc, red represents areas of extremely high curvature, yellow to orange is high curvature, moderate curvature is represented by green, low curvature to straight sections are represented by blue and finally purple and pink show low to negative curvature. The ventral disc MTs must curve to form the spiral shape of the array. Although a lot of the ventral disc MTs conform to the expected curvature as they progress through the spiral, there are several regions that deviate from this pattern. Most obvious is the VG, which has negative curvature, where the fitting circles are fit to the outside of the disc edge. Both the DOZ and VOZ have tighter curvature than the rest of the ventral disc.

Kappa Value	Color in heat map	Description of Curvature
>1.90	Red	Extremely high
>1.50 to 1.90	Orange	High
>1.00 to 1.50	Yellow	High moderate
>0.50 to 1.00	Green	Moderate
>0.00 to 0.50	Blue	Low to straight
-0.49 to 0.00	Pink/purple	Negative low to straight

Table 4.1: Kappa values, their corresponding color in the heat map (Figure 4.4) and description of curvature.

In order to form a spiral it is expected that the MTs of the ventral disc will have higher curvature when closer to the center edge of the disc. As the MTs spiral out towards the marginal edge, their curvature will decrease. As the MTs come to termination in the margin, their curvature should become shallow and closer to being straight.

This pattern is observed across most of the array (Figure 4.4), with MTs at or near the center edge showing high curvature (orange and yellow). MTs in the middle of the array have moderate curvature (green), decreasing to low curvature (blue) as they become close to straight on the margin (Table 4.1). However, there are some areas of the array that do not conform to this general pattern.

Most obvious is the VG and the areas of disc body MTs that flank the VG (Figure 4.4). The DOZ follows the expected curvature pattern, although all the values are shifted up, as if it were fitted to a spiral with a smaller initial radius. The VOZ also exhibits higher than expected curvature values (Figure 4.4). The patterning of curvature is also reversed. Instead of curvature decreasing along the MT in the minus to plus direction, the opposite trend is observed. Curvature increases in this region, with the tightest curvature values being observed near the plus ends of the MTs.

The example seven MTs illustrate nicely that curvature varies in a regular fashion dependent upon a MTs location within the array (Figure 4.5). It also demonstrates that clear changes in curvature can be observed as a MT transitions from region to region.

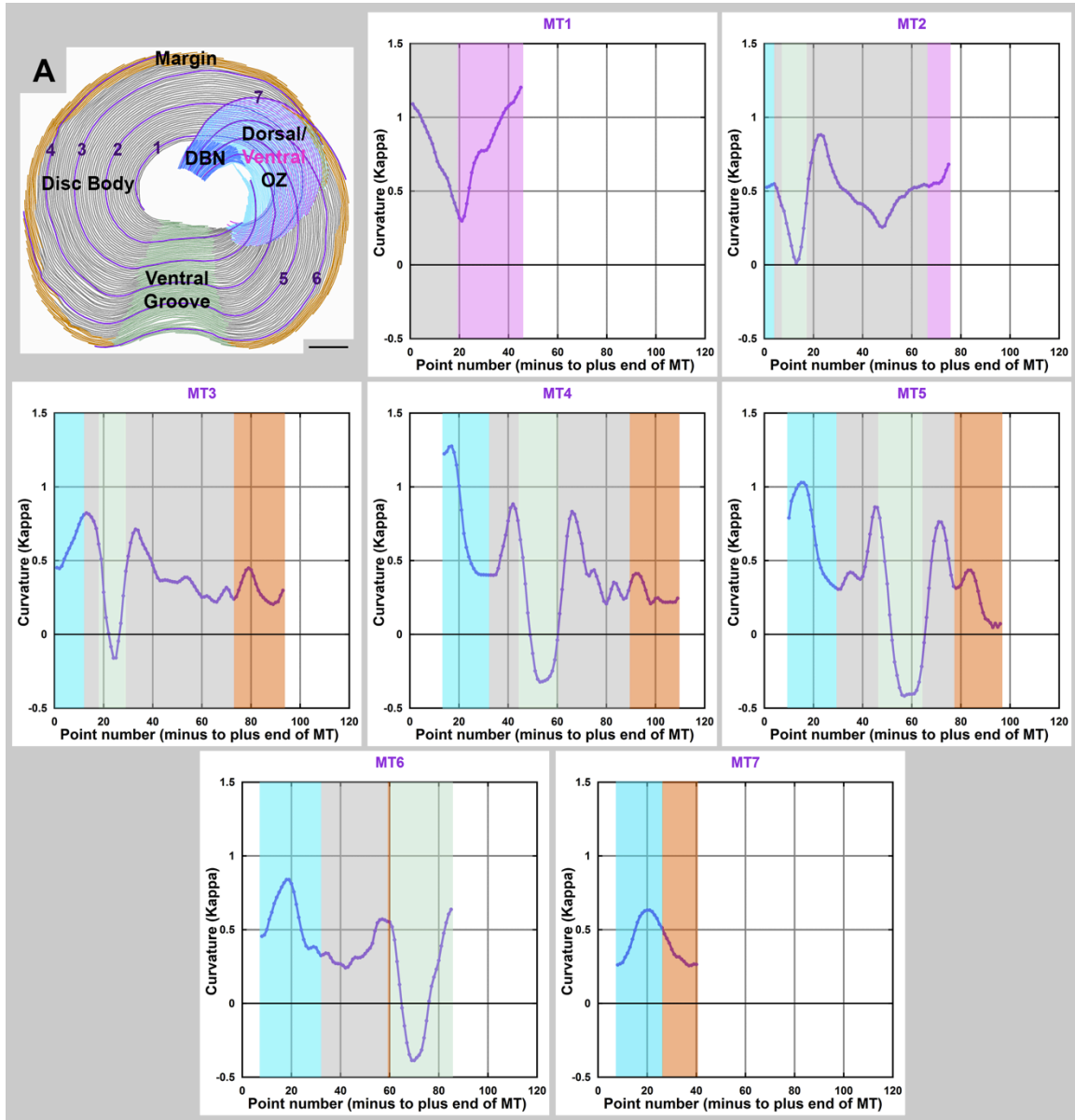


Figure 4.5: Variations in curvature along individual MTs. Panel A: Model of the ventral disc colored to show the regions: dense bands nucleation zone (blue), dorsal overlap zone (cyan), disc body (grey), ventral groove (green), ventral overlap zone (pink), and margin (orange). The example seven MTs (purple) are numbered 1 to 7. **Panel 1 to 7:** The curvature of each of the seven example MTs from a single disc ($N=1$) has been plotted point by point from the center to the margin along the length of the MT. The background had been colored to show the regions, the colors are the same as Panel A. These graphs illustrate how curvature changes along a single MT as it passes through multiple different regions. If the spiral was uniform in all regions, the MTs would transition from low to high curvature as the spiral from the center to the marginal edge of the array. The curvature profiles of the special seven MTs clearly illustrate this is not the case.

Descriptions of the Curvature Profile of Each Ventral Disc Region

Highly curved Microtubules in the Dorsal Overlap Zone (Figure 4.6)

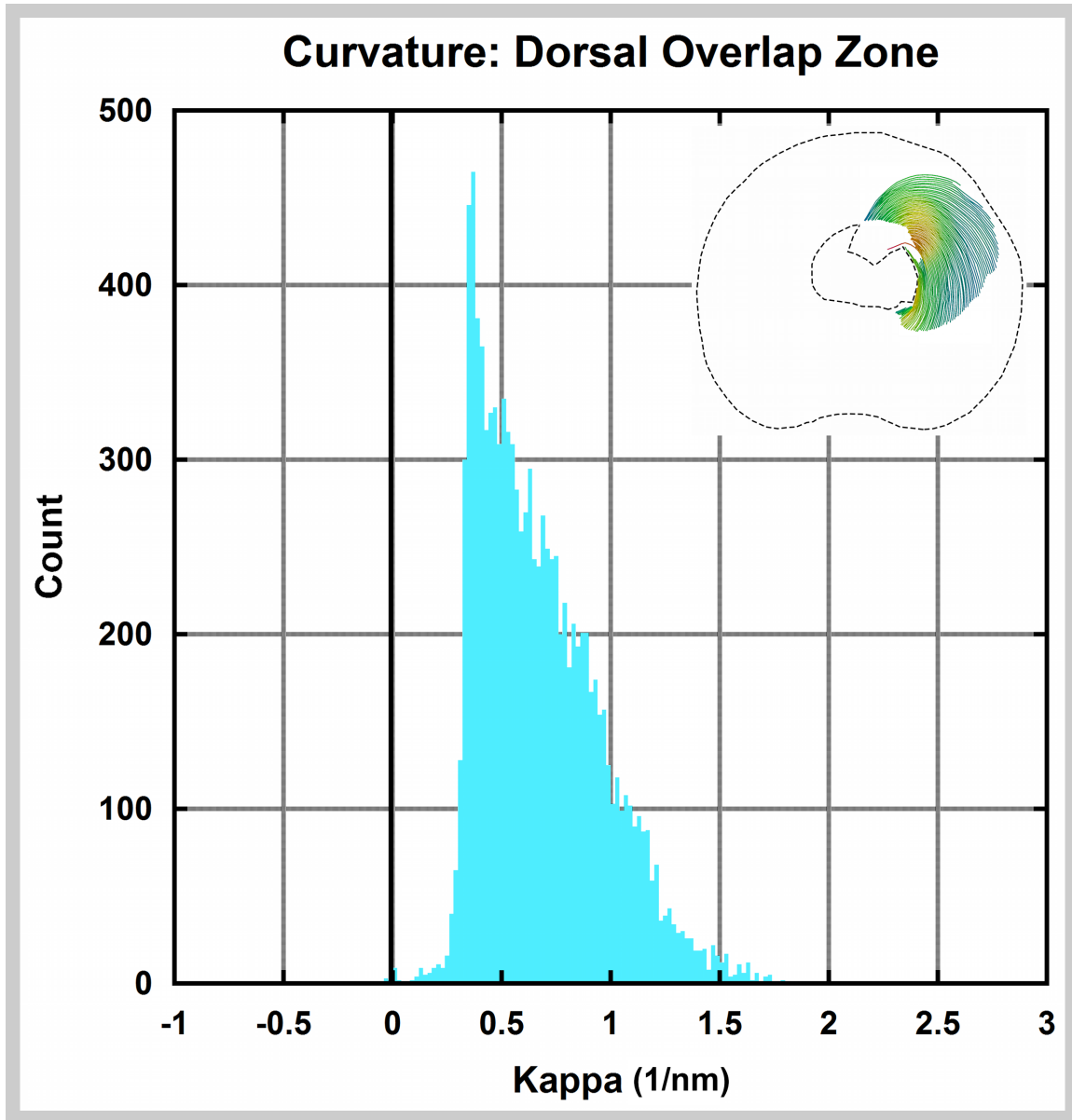


Figure 4.6: Histogram of curvature values of the dorsal overlap zone (N=6). The dorsal overlap zone has a curvature profile with few low or negative curvature components. This peak comes from the MTs closest to the margin that spread out from the closely packed MTs near the center edge. The curve for the DOZ is broad with a few counts reaching into the high curvature range above 1.5 nm^{-1} . There are a few MTs on each disc that are extremely highly curved, but these regions are so small they contain hardly any points and do not appear on the histogram.

The DOZ forms as the MTs of the DNZ fan out into a single layer after nucleated at the DBs microtubule organizing center. Due to the location of the DBs (near the center of the ventral disc), and the angle at which the MTs exist in the DNZ, higher curvature (Figure 4.6) is needed in this region in order to form a disc with the observed diameter.

The DOZ has an area at the center edge where the MTs are very closely packed and extremely highly curved (red), in comparison to the rest of the ventral disc (Figure 4.4). In this area, the pattern of decreasing curvature from center to margin is still maintained, though the range of curvature values is shifted up. It is not currently known how a localized area of tight curvature is imparted to this specific region during ventral disc formation or how it maintained throughout the lifetime of the array [76]. Thus far, no tightly curving MT structures analogous to the ventral disc of *Giardia* have been discovered in other organisms.

In the DOZ, the MTs also fan out from being closely packed to being more widely spaced. This increase in spacing occurs in order from the margin to the center edge and is characteristic of the MT arrangement in the DOZ. As a MT breaks away from the closely packed area to become more widely spaced in relation to its neighbors, its curvature the pattern seen in the rest of the array (Figure 4.4).

Curvature in the Disc Body (Figure 4.7)

The majority of the disc body follows the expected pattern of curvature for a spiraling array (Figure 4.7). However, as the disc body approaches the VG, curvature increases as

the MT begin to pack more closely (Figure 4.4 and Figure 4.7). The opposite pattern is observed as the VG transitions back into the disc body.

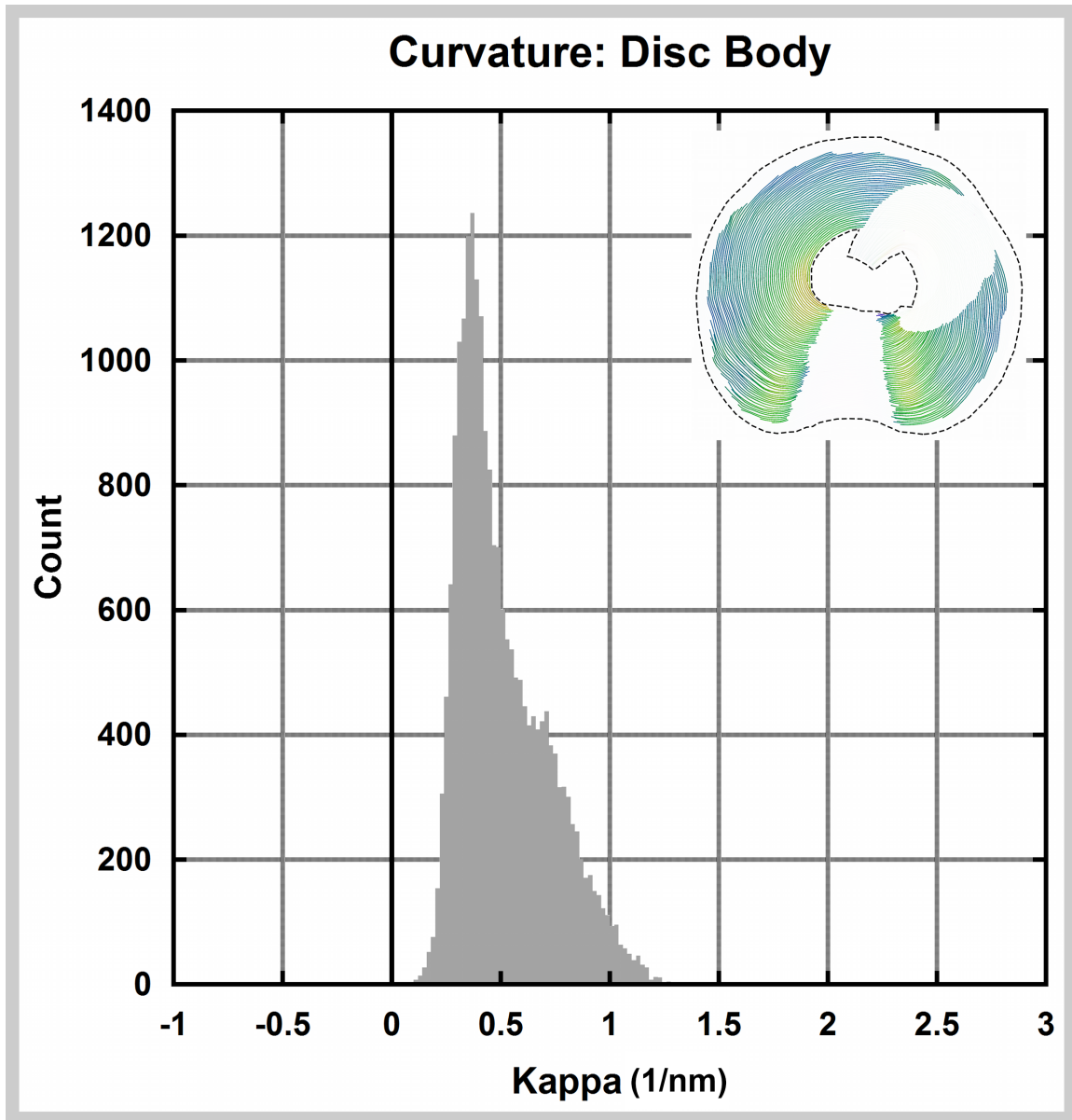


Figure 4.7: Histogram of curvature values of the disc body region (N=6). The disc body again has a peak in the low curvature regions (0 to 0.5), that come from the long stretches of MTs present close to the margin of the disc. There is a small peak in the moderate range (>0.5 to 1) of curvature values. This peak comes from an increase in curvature in this region just before the MTs transition into the disc body. The highest curvature values in this region are seen in the high moderate range (>1 to 1.5). This comes from short stretches of MT of the disc body region present at or near the center edge of the array.

Curvature of the Ventral Groove MTs (Figure 4.8)

In order to accommodate the close packing of MTs observed in the VG, an increase in curvature is observed at the disc body MTs transition in the VG region. As the 2D dip forms, the MTs pass through an inflection point where they are relatively straight (Figure 4.4 and Figure 4.8). It is here that the characteristic MT spacing and morphology of the MR and crossbridges in the VG can be observed. The VG is the only disc region where negative curvature is observed (Figure 4.8). The closely packed MTs continue to curve away from the center of the disc with tightness of curvature reaching a maximum near, but slightly off center of the middle of the VG. The tightness of curvature at the apex of the dip is comparatively low compared with the rest of the ventral disc.

In this study we can only account for curvature in the VG that occurs in the flattened disc configuration. In the domed disc, changes in curvature must occur along the Z- axis to form the channel for the flagella. It is possible that the pressure of the flagella on top of the array induces the Z- axis dip; however, this does not account for the negative curvature that must occur to allow the close packing of MTs dip observed in the extracted discs. Again, the mechanism by which this curvature is achieved is unknown; however, since there are specific DAPs that are missing from and localizing particularly to the VG, it is likely that MT decoration plays a role.

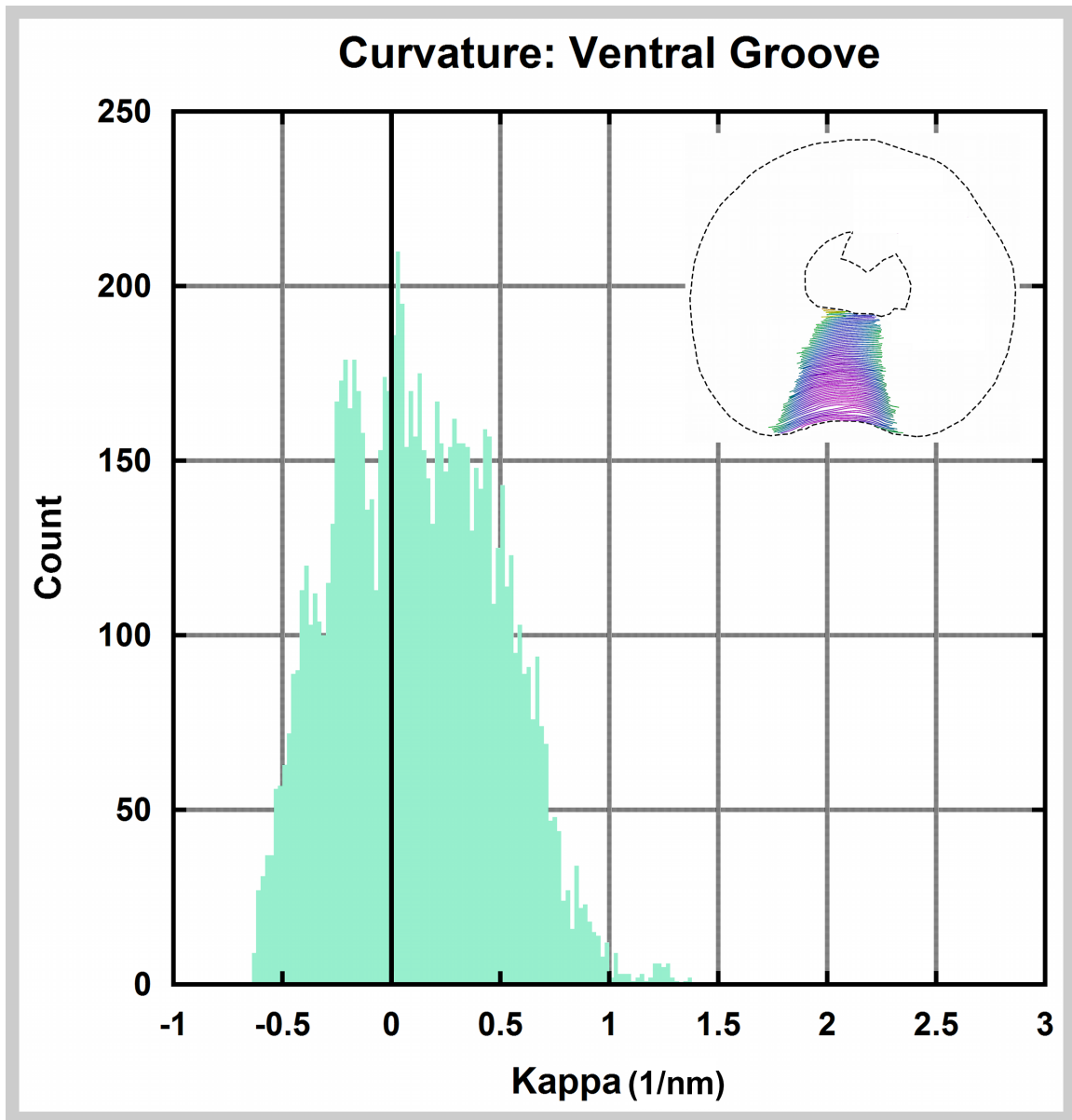


Figure 4.8: Histogram of curvature values of the VG region (N=6). The VG has a curve that is very different from the other regions of the ventral disc. The curve centers around a peak just above zero, where the MTs are almost straight. This represents the inflection point where the MTs transition from positive to negative curvature. In the center of the VG the MTs are closely packed and curve away from the center of the disc, this curvature was assigned a negative value to reflect the change in direction. The highest values of negative curvature just enter the moderate range (<-0.5), and are located near the marginal edge. The MTs near the center edge, even in the middle of the VG are almost straight. The MTs on both edges of the VG have low (>0 to 0.5) and moderate (>0.5 to 1) curvature. There are some values in the VG that fall into the high moderate category (>1), these values likely come from “ruffling” artifacts in this region that artificially increase the curvature of the MTs in this region.

Curvature in the Ventral Overlap Zone (Figure 4.9)

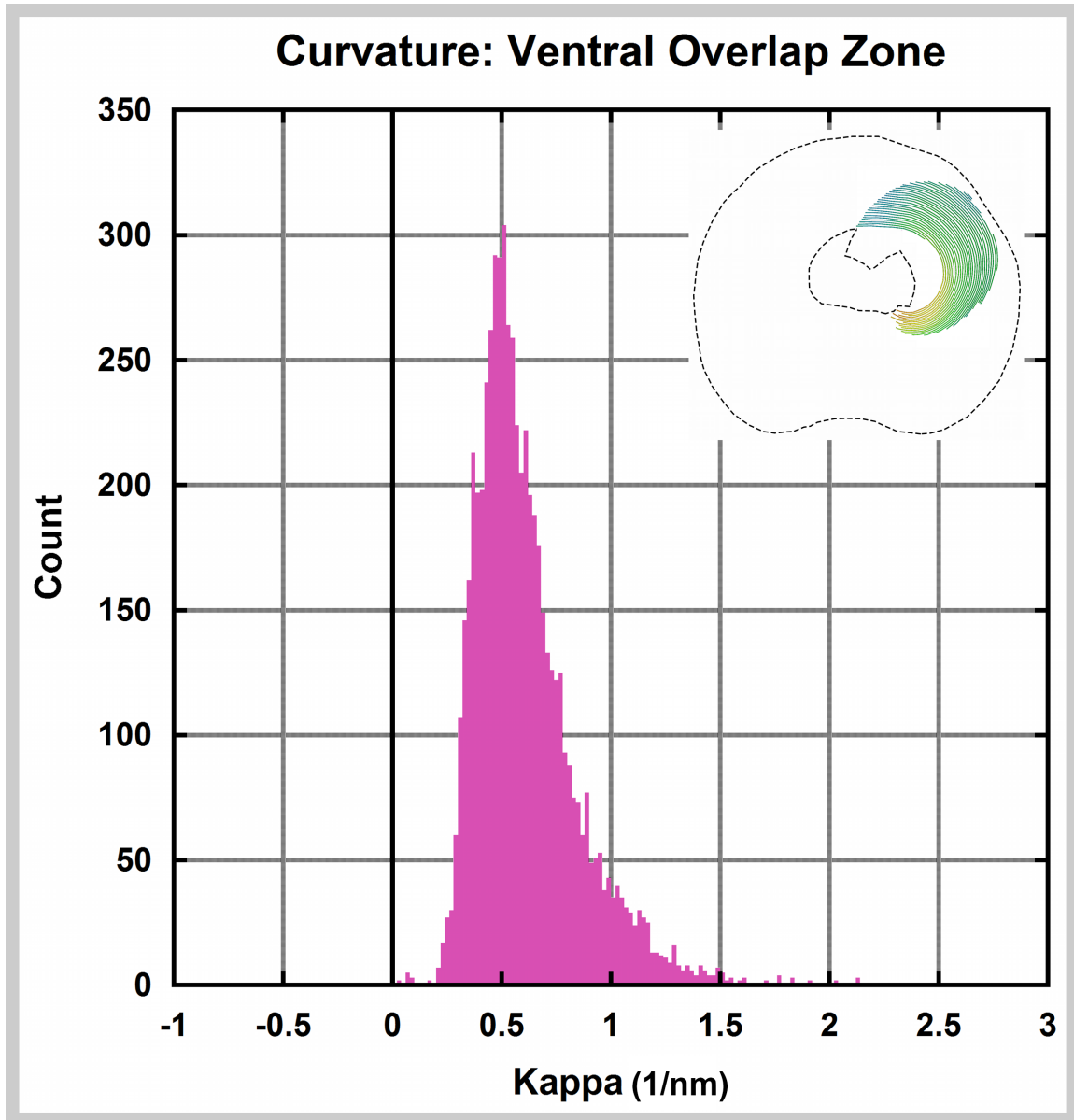


Figure 4.9: Histogram of curvature values of the VOZ region (N=6). The VOZ has a peak at the transition between low and moderate curvature (around 0.5). Instead of curvature decreasing in this region, curvature increases towards the plus end of the MTs. The curve has the same profile that would be expected for a spiral, but it is shifted towards higher values of curvature. Extremely high (>1.90) curvature values can be seen at the ends of the MT that reach some of the highest values seen in this disc.

Curvature of the MTs in the VOZ varies from moderate to high and in some cases extremely high (red) in certain discs (Figure 4.4 and Figure 4.9). The tightness of

curvature varies from disc to disc but tends to correspond with the length of the VOZ MTs. Ventral discs that have longer MTs that extend past the VG up towards the basal bodies tend to have more extreme (red) curvature at the ends.

Interestingly, the VOZ deviates from the curvature trend that would exist if the disc formed an ideal spiral. Instead of following directly around the margin on the edge of the DOZ, the VOZ curves in towards the center of the spiral. The tightness of curvature actually increases as the ventral disc comes to termination in the VOZ, meaning curvature increases from along the MT in a minus- to plus- end direction. This is the opposite trend from all other regions of the disc and is only observed in the VOZ. The mechanism by which an increase in curvature is induced as MTs enter this region and proceed to termination, is not known.

Curvature in the Margin (Figure 4.10)

The margin most closely fits the curvature profile expected from a regular spiral (Figure 4.4 and Figure 4.10). The curvature of MTs in this region is low (Figure 4.10). As the MTs enter the margin, they are near the outermost edge of the disc and are therefore expected to have the lowest curvature. There some curvature artifacts resulting from cytoskeleton extraction can be seen in the margin. There are some areas where “ruffling” occurs that contribute to non-native curvature of the MTs, increasing the curvature above the normal range.

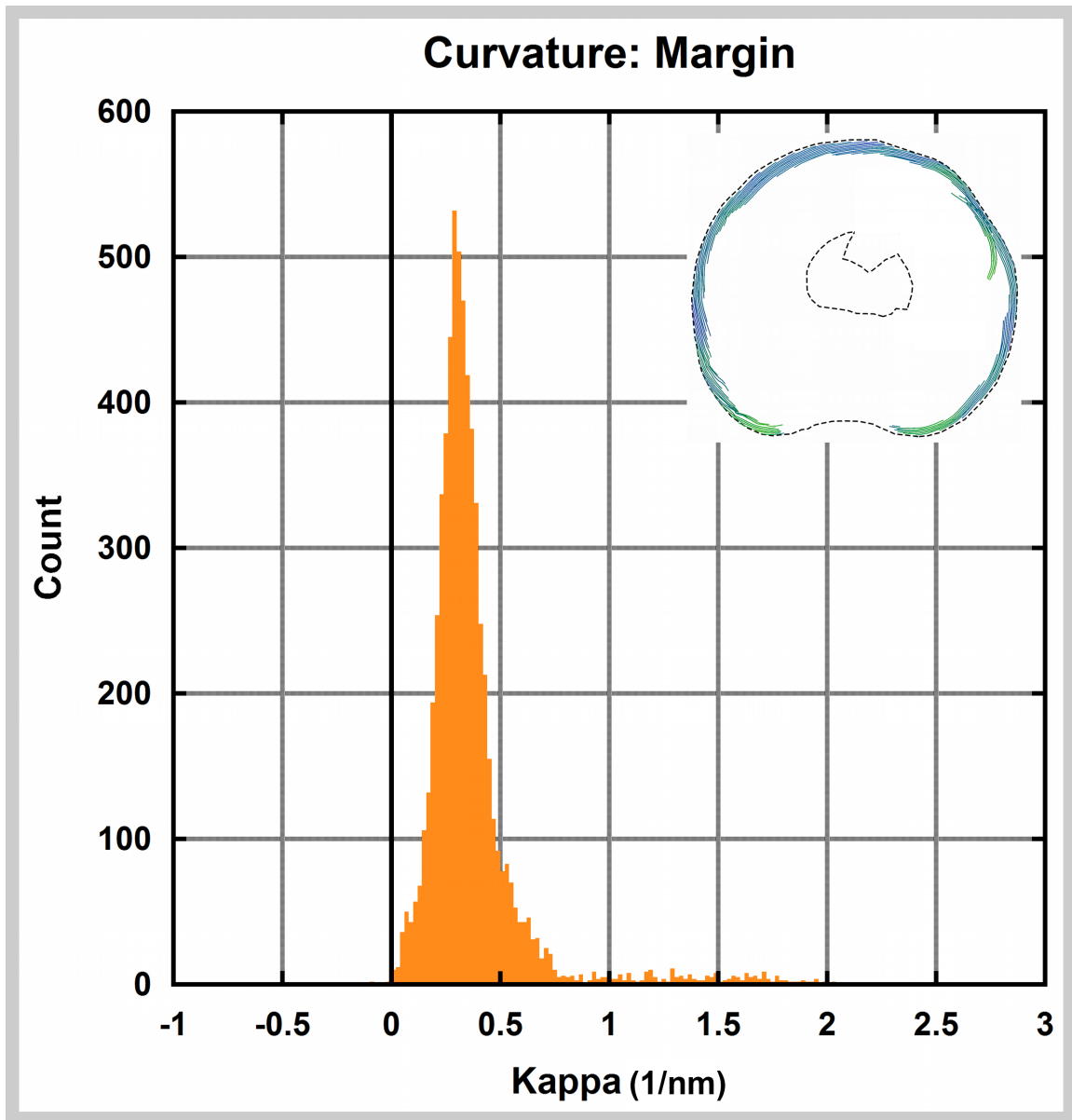


Figure 4.10: Histogram of curvature values in the margin region (N=6). The margin region is located around the marginal or outer edge of the ventral disc array. As the MTs spiral out to the edge of the disc, they become straighter and the margin curvature is highly consistent. There is a large peak of counts in the low curvature range (>0 to 0.5). There are values that extend from ~0.75 to >2. These values result short stretches increased curvature on either side of the ventral groove and from “ruffling” of the disc MTs that artificially increases curvature. In general most of the margin is consists of MTs that are close to being straight.

Regional Transitions Along Individual MTs

Now that the characteristics of each region have been established, it is important to consider how the regions are linked together to form a functional ventral disc. The MTs that form each region are not independent and are rarely unique to just one disc region. In fact, a single MT often passes through multiple regions and its decoration and associated structures undergoes multiple structural transitions along its length (Figure 4.11).

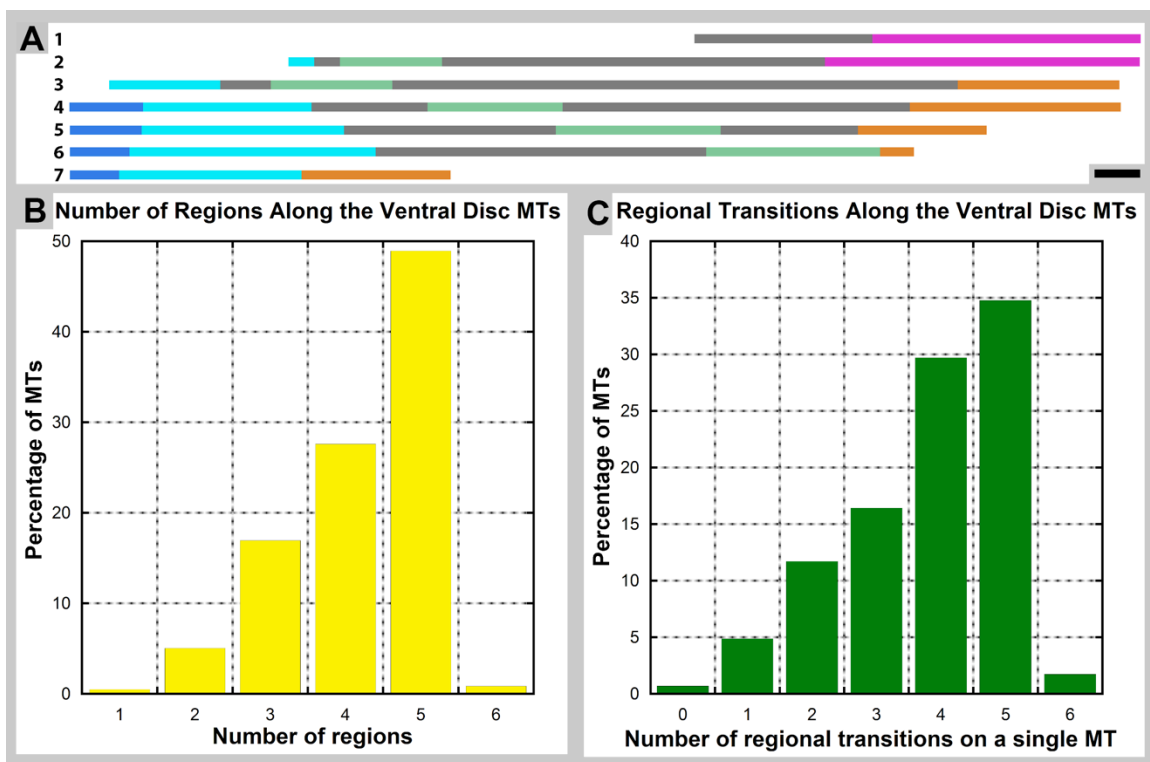


Figure 4.11: Regional transitions of the ventral disc MTs. **Panel A:** The example seven MTs have been divided by disc region: DNZ (blue), DOZ (cyan), disc body (grey), VG (green), VOZ (pink) and margin (orange). The panel illustrates how individual MTs pass through multiple different regions and transition between them. **Scale bar = 31 nm.** **Panel B:** shows the percentage of MTs that pass through different numbers of regions (N=6). Almost half of the MTs are long enough to pass through five separate regions. A small percentage of MTs pass through only 1 region. **Panel C:** shows the percentage of MTs that undergo different numbers of regional transitions (N=6). This gives an indication of the number of structural transitions that occur along a single MT.

The variability in the number regions ventral disc MTs pass through illustrates differences in MT lengths that exist within the ventral disc, demonstrating that some MTs

are too short to pass through more than a single region, while others are long enough to pass through all six regions of the disc. Almost half of the MTs in the ventral disc pass through five distinct regions, undergoing up to six structural transitions. Any MTs that pass through the VG will transition back into a disc body region before entering either the margin or VOZ (Figure 4.1). This means that almost all the MTs in the ventral disc undergo multiple instances of reorganization in terms of MT spacing, MR height, crossbridge length and morphology (Figure 4.2), and the degree of MT curvature (Figure 4.4).

It is clear that specific structures and MT arrangements must occur in specific areas of the disc, allowing the mature array to fit together correctly as a single functional unit. It is known that changes in the structure of the array lead to impaired attachment of the trophozoites [123]. The mechanisms by which variations in structures, MT arrangement, and MT curvature are imparted and maintained during the lifetime of the array are unknown. Given that differential protein localization has been observed in the DAPs [121], it is highly likely these proteins play an important role in forming and maintaining the regional characteristics observed.

Results Summary and Discussion

Six structurally distinct ventral disc regions have been identified. These regions include: the DNZ, the DOZ, the Disc Body, the VG, the VOZ and the Margin. The regions vary

based on four characteristics: the MT organization relative to the neighboring MTs, MT curvature, the height and morphology of the MRs, and the morphology and length of crossbridges (Table 4.2).

Region	MT/MR spacing	Microribbons	Crossbridges	Curvature
Dense Bands Nucleation Zone	side-by-side, three layers	none, to very short	none	unknown
Dorsal Overlap Zone	closely packing, single layer MRs ~32 nm apart	tall and straight	short , 16 nm repeat	moderate to extremely high
Disc Body	widely spaced, single layer MR 54 nm apart	tall and straight	Long, 16 nm repeat	moderate to low
Ventral Groove	close packing, single layer MR ~37 nm apart	short	Short, angled, 16 nm repeat	Negative low, straight and low
Ventral Overlap Zone	widely spaced, single layer MR ~54 nm apart	decreasing throughout region to short	long, 16 nm repeat	moderate to high
Margin	closely packed, single layer MR ~35 nm apart	short, and angled	thicker, short, 16 nm repeat	majority low

Table 4.2: Structural and organizational characteristics used to define each ventral disc region.

In the mature ventral disc, a single MT can pass through up to six different regions, undergoing up to six structural and organization transitions. It is currently unknown exactly how these structural differences are introduced to specific locations in the ventral disc. It seems likely the DAPs are involved, as the MTs are known to be highly decorated [84], and the localization of the DAPs is not uniform across the ventral disc [121].

Using the published images of DAP localization [121] an attempt was made to compile a list of all the possible DAPs that could be found in each ventral disc region (Table 4.3).

However, the information that can be obtained from this type of visual correlations is limited by several factors including: the resolution gap between light and electron microscopy; the lack of the ability to distinguish between the margin and the lateral crest; the occlusion of the DNZ by other components; the possibility of a ventral disc lacking complete incorporation of GFP tagged subunits; and the possibility of mis-localized DAPs due interference by the GFP tag.

This analysis produced a list of seventeen proteins (top seventeen DAPs in Table 4.3) that seem to be common to all regions of the disc. Two proteins (DAP17053 and DAP103807) were missing from the VG, but found in all other regions. The VG and margin (or lateral crest) contain DAP13981, which was absent from the other three regions. The DOZ and VOZ contained two proteins (DAP17090 and DIP13) that were previously thought to localize to the snMTs. The margin or lateral crest contains nine proteins not found in other ventral disc regions. High-resolution information about structure of each region is required to accurately determine the differences that might exist in protein composition.

DAP	Name	Motifs	D O Z	D B *	V G	V O Z	M /L C
112079	Alpha-2 tubulin	tubulin	✓	✓	✓	✓	✓
101291	Beta tubulin	tubulin	✓	✓	✓	✓	✓
7796	Alpha-2 annexin	Annexin	✓	✓	✓	✓	✓
11683	Alpha-3 annexin	Annexin	✓	✓	✓	✓	✓
7797	Alpha- 5 annexin	Annexin	✓	✓	✓	✓	✓
15101	Alpha-17 annexin	Annexin	✓	✓	✓	✓	✓
4812	Beta-giardin	SF-assemblin	✓	✓	✓	✓	✓
86676	Delta- giardin	SF- assembling	✓	✓	✓	✓	✓
17230	Gamma-giardin	Novel	✓	✓	✓	✓	✓
4410	SALP-1	Novel	✓	✓	✓	✓	✓
16279	Nek kinase	Protein kinase	✓	✓	✓	✓	✓
103807	Ankryrin repeat protein	Ankryrin repeat	✓	✓	✓	✓	✓
92498	Nek kinase	Protein kinase	✓	✓	✓	✓	✓
5010	Ser/Thr prosphatase PPsA-2 subunit	Metallo- dependent Phosphatase	✓	✓	✓	✓	✓
5374	CAP_GLY	CAP_GLY motif	✓	✓	✓	✓	✓
16343	MBP	Novel	✓	✓	✓	✓	✓
13766	Ankyrin repeat protein	Ankyrin Repeat	✓	✓	✓	✓	?
17053	Ankryrin repeat protein	Ankryrin repeat	✓	✓	✗	✓	?
103807	Ankyrin repeat protein	Ankyrin repeat	✓	✓	✗	✓	?
13981	Nek kinase/ ankryrin	Protein kinase and ankryrin repeat	✗	✗	✓	✗	?
17563	ERK1 kinase	Protein kinase	✗	✗	✗	✗	✓
17096	Ankryrin repeat protein	Ankryrin repeat	✗	✗	✗	✗	✓
24194	Ankryrin repeat protein	Ankryrin repeat	✗	✗	✗	✗	✓
103810	Ankryrin repeat protein	Ankryrin repeat	✗	✗	✗	✗	✓
17097	Ankryrin repeat	Ankyrin repeat	✗	✗	✗	✗	✓
16424	Hypothetical protein	Novel	✗	✗	✗	✗	✓
23492	Ankyrin repeat protein	Ankyrin repeat	✗	✗	✗	✗	✓
14872	Ankyrin repeat protein	Ankyrin repeat	✗	✗	✗	✗	✓
15576	Ankyrin repeat protein	Ankyrin repeat	✗	✗	✗	✗	✓
17090	SAM motif protein	SAM	✓	✗	✗	✓	✗
16263	DIP13	Novel	✓	✗	✗	✓	✗

Table 4.3: Organization of the DAPs based on their GFP localization patterns to regions of the ventral disc. Information was obtained from Hagen et al, 2011 [121]. * indicates that DB has been used to represent the disc body region, not the dense bands, margin (M) and lateral crest (LC) . A tick indications the DAP localizes to a region and a cross indicates that it does not. The “?” indicates that it was not possible to visualize the absolute marginal edge of the ventral disc, so it was not possible to be certain if the localization included the margin or lateral crest. The DNZ has been omitted as the region is obscured by other cellular contents in the fluorescence microscopy images.

Even though significant structural variation appears to exist between the ventral disc regions, there is one dominant structural feature that is conserved. Despite changes in

length and morphology, the crossbridges occurred at a repeat length of 16 nm in 5 of the of the 6 ventral disc regions, forming very regular connections between the neighboring MRs. These regular connections may play a crucial role in maintaining the overall architecture within ventral disc array.

Connections between MTs have been observed previously that were governed by the axial 4 nm and 8 nm repeat frequency of the tubulin monomers and dimers [164]. It seems likely that the frequency of occurrence of the crossbridges is related to the 8 nm α/β tubulin heterodimer length, as it is twice that difference. This suggests that each 16 nm repeating unit that forms the MR has either a long projection that forms the crossbridge, or has a binding site onto which other proteins assemble.

CHAPTER 5: Structures of the Regional Repeating Units of the Ventral Disc

Introduction

An intermediate-resolution structure of the ventral disc repeating unit was obtained by Schwartz, C. et al, (2012) using cryo-ET [84] (see Chapter 1, Figure 1.6). This structure was initially thought to represent the repeating unit for the entire ventral disc. It is now known that the structure obtained represents the repeating unit of the Disc Body region only.

Now that it is known that regional variation exists between coarse structures that compose the ventral disc, it was logical to extend this study to investigate the variation that might exist between the smaller repeating units for each region. In order to do this, the sample preparation method was changed from negative stain to rapid plunge freezing and vitrification. This method better preserves the fine structural detail of biological samples. The resultant tomograms were further processed using subvolume averaging to produce a 3-D density map with enhanced signal-to-noise ratio.

Only four of the six ventral disc regions were amenable to cryo-ET. The quantity of material present in both the DNZ and VG meant that collection of high quality cryo-tomograms was not possible. However, by working in collaboration with Cindi Schwartz,

three additional structures were produced for the DOZ, the VOZ and the margin.

The disc body structure revealed that the MTs are highly decorated both on the inside and outside surface [84]. The protein densities observed were named by their location in the structure (See chapter 1, Figure 1.6). The densities are presumably composed by the DAPs that localize to the ventral disc; however, it is not yet known which DAP corresponds to which of the observed densities.

The structures of the DOZ and VOZ have decoration in the same location as was observed in the disc body. Interestingly, significant variation exists by region between the size and shape of a number of these densities. The 3-D structures derived by subvolume averaging with PEET from the four ventral disc regions listed above were also used to gain insight into which structural components of the ventral disc are common to the entire array. The four regional averages were aligned and correlated to produce an estimate of the common core ventral disc repeating unit. This core unit is composed of densities that appear to be the same in all four 3-D structures.

In order to obtain cryo-ET data, the cytoskeletons were rapidly plunge frozen on holey carbon grids to produce frozen- hydrated samples contained in a thin layer of vitreous ice. Regions of the ventral disc were imaged and single axis tomograms were reconstructed using IMOD. IMOD was used to model the MT/MR interface and define the center point for each subvolume (Figure 5.1). PEET was used to align and average the subvolumes to produce a final result with a greatly enhanced signal-to-noise ratio (Figure 5.2 and Figure

5.3). PEET alignment was used to align the regional averages for statistical analysis of common and divergent densities (Figure 5.6).

Results

The cryo-ET data collected at the overlap zone revealed the same patterns of MT spacing, MR height, and crossbridge length, as were visualized in the negative stain (Figure 5.1). The cryo-tomograms also allow the visualization of the three trilaminar sheets of the MR. An additional density could be distinguished on the margin facing side of each MT. This structure is known as the side arm [62,84]. Tomographic data could not be collected from areas of the OZ that were located in the most anterior part of the ventral disc. The material, such as the snMTs, meant that sample thickness was prohibitively thick in that area.

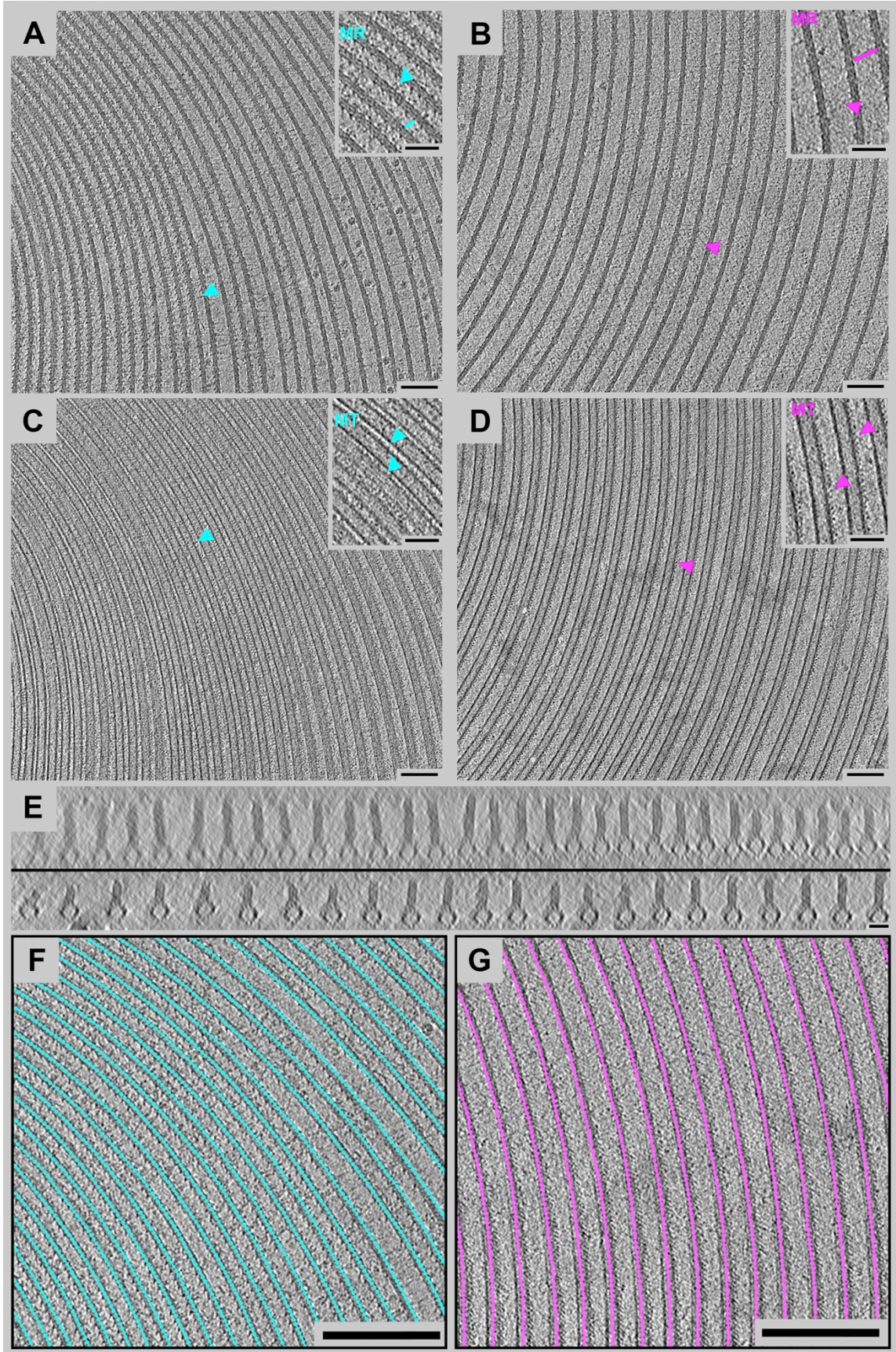


Figure 5.1: Tomographic slices from cryo-ET data of the overlap zone. Panel A: 7.75 nm thick X, Y tomographic slice of the MRs of the DOZ. **Scale bar = 50 nm. Inset in panel:** Zoomed in view of a small section of MRs. **Scale bar = 35 nm.** Cyan arrows indicate examples of the crossbridges, cyan bar an example of crossbridge length. The dark spheres are believed to be ribosomes that became trapped between the MRs during extraction of the cytoskeleton. **Panel B:** 7.75 nm thick X, Y tomographic slice of the MRs of the VOZ. **Scale bar = 50 nm. Inset in panel:** Zoomed in view of a small section of MRs. **Scale bar = 35 nm.** Pink arrows indicate examples of the crossbridges, pink bar an example of crossbridge length. **Panel C:** 7.75 nm X, Y tomographic slice of the MTs of the DOZ. **Scale bar = 50 nm. Inset in panel:** Zoomed in view of a small section of MTs. **Scale bar = 35 nm.** Cyan arrows indicate examples of side arms. **Panel D:** 7.75 nm X, Y tomographic slice of the MTs of the VOZ. **Scale bar = 50 nm. Inset in panel:** Zoomed in view of a small section of MTs. **Scale bar = 35 nm.** Pink arrows indicate examples of side arms. **Panel E:** 15.5 nm thick tomographic slice of each surface of the overlap zone in cross section. The DOZ is shown above the VOZ. **Scale bar = 25 nm.** The PFs of each MT and the trilaminar sheets of the MRs can be clearly seen in each region. It is clear that the MRs of the VOZ are significantly shorter than the MRs of the DOZ. **Panel F:** Model at the MT/MR interface, each cyan dot represents the center of a subvolume used for averaging. **Scale bar = 100 nm.** **Panel G:** Model at the MT/MR interface, each pink dot represents the center of a subvolume used for averaging. **Scale bar = 100 nm.**

MT spacing and curvature

Close packing between the MRs and MTs in the DOZ was observed in the frozen-hydrated samples, as it was in the negative stained ventral discs. The spacing between the neighboring MTs/MRs increases from the center of the disc to the marginal edge, as was observed previously. The neighboring MTs/MRs of the VOZ presented a uniform wide spacing, as in the negatively stained discs (Figure 5.1, Panel A and C).

MR height

Cryo-tomograms of the ventral disc can be rotated around the X- axis to show the MRs in cross-section in the Y, Z plane (Figure 5.1, Panel E). The DOZ and VOZ cannot be visualized face on at the same time because the MT are oriented at a different angle relative to one another. The long MRs of the DOZ can be observed in the cross section extending approximately 75 nm above the MT. The MRs of the VOZ are considerably shorter in height, ranging from approximately 20 nm (shorter than the diameter of the MT), up to 50 nm (twice the diameter of the MT) (Figure 5.1, Panel E).

Crossbridge length and morphology

The crossbridges between MRs are clearly visible in both the DOZ and VOZ regions (Figure 5.1, Panels A and B). The DOZ contains short crossbridges connecting the closely packed MRs. In the VOZ, the long crossbridges were observed connecting the widely spaced MRs. Some of the crossbridges appear to project out from the MR at an angle less than 90°. This angulation was not observed in the negative stain. Both the DOZ and the VOZ have sections where crossbridges are missing. It is likely that these

were damaged or broken during extraction of the cytoskeletons.

Side arms

The cryo-ET reveals the presence of structures known as side arms [62,84] (Figure 5.1, Panels C and D). The side arms could not be distinguished from the MT wall in the negative stain data. The side arms extend from the marginal MT wall in both regions. In the DOZ, it is not clear if the side arms are connecting adjacent MTs. The side arms in the VOZ do not appear to extend to neighboring MTs.

In order to improve the signal-to-noise ratio and reveal structures that are not directly visible in a single unit, the ventral disc MTs were modeled at the interface of the MR and MT. Model points were placed at 8 nm intervals along the model contours. Each point was used to define the center of a 70x70x70 pixel subvolume. PEET software was used to align the subvolumes and generate a 3D density map for each region (Figure 5.2 and Figure 5.3). More details are presented in chapter 7.

Subvolume Averaging of the Dorsal and Ventral Overlap Zone

The coarse structural components of the ventral disc were originally described by Holberton [61,62,63] Holberton demonstrated that the ventral disc is composed of MTs with MR structures extending dorsally from each MT. Holberton also identified the side arm [62] a structure extending out from the margin side of each MT. Cindi Schwartz enhanced our knowledge of ventral disc composition by producing a much higher

resolution structure using subvolume averaging. This structure, now known to represent the repeating unit of the disc body, demonstrated that the ventral disc MTs are highly decorated in specific locations on and around the MT [84]. The structure also shows that the MRs are not a single unit, but actually consist of trilaminar sheets that extend, side by side from the top of each MT [84,121]. It was also discovered that there were proteins bound to the inner surface of the MT, and these are known as MIPs or in *Giardia* as GMIPs [84].

Given that it is now known that regional variation exists within the coarse structures that compose the ventral disc, it was logical to generate higher resolution structures for each region of the overlap zone. A similar subvolume averaging protocol to that employed to produce the disc body structure was used to generate an average volume for both the DOZ and the VOZ. The aim was to allow a comparison to be made between these structures that compose two regions that are close in space, but exist at opposite ends of the spiraling array.

Subvolume Averaging Specifications

The DOZ average was produced from aligning just over 20,000 subvolumes, and the VOZ average was produced from just over 13,000 subvolumes. There is uncertainty as to the accuracy of the method commonly used to estimate the resolution of EM data [165]. However, an internal resolution of 2.8 nm (28 angstroms) as determined by Fourier shell correlation (FSC) at a threshold of 0.5 [166,167]. The 70x70x70 pixel volume (159,661 nm³) contained 6.8 x 8 nm repeating structural units. The crossbridges, were seen to

repeat at intervals of 16 nm, as observed throughout the negatively stained ventral discs.

The subvolumes used to generate each 3D density map were obtained from six individual tomograms. Three of these tomograms were imaged at $-6 \mu\text{m}$ defocus and three were imaged at $-4 \mu\text{m}$ defocus, in an effort to recover the maximum amount of information in the CTF correction. Each ventral disc, from each individual tomogram, is oriented slightly differently relative to the tilt axis. This means the missing wedge was located in a slightly different location within the individual subvolumes. By including subvolumes from different tomograms, the missing wedge was reduced as much as possible to a missing cone in the average volume. The missing cone could not be fully filled in because the large flat ventral discs are always oriented either MRs up or MRs down relative to the projection axis.

The 3D averaged volumes produced by PEET are shown in grayscale (Figure 5.2 and Figure 5.3). The darkness of a density represents its regularity in the subvolumes that contributed to the final average. Very regular structural features appear as dark. In both the DOZ and VOZ, the PFs of the MTs and the MRs appear very dark. Structures that appear with irregular frequency or in multiple conformational states appear as lighter or closer to the background grey. Structures that are very irregular will not be enhanced by averaging and will be indistinguishable from the background noise. The average volumes also contain bright white areas that could represent the absence of density in the sample, ie. a hole in the structure, but can also result from artifacts that occur when averaging data containing a missing wedge and an imperfectly corrected CTF.

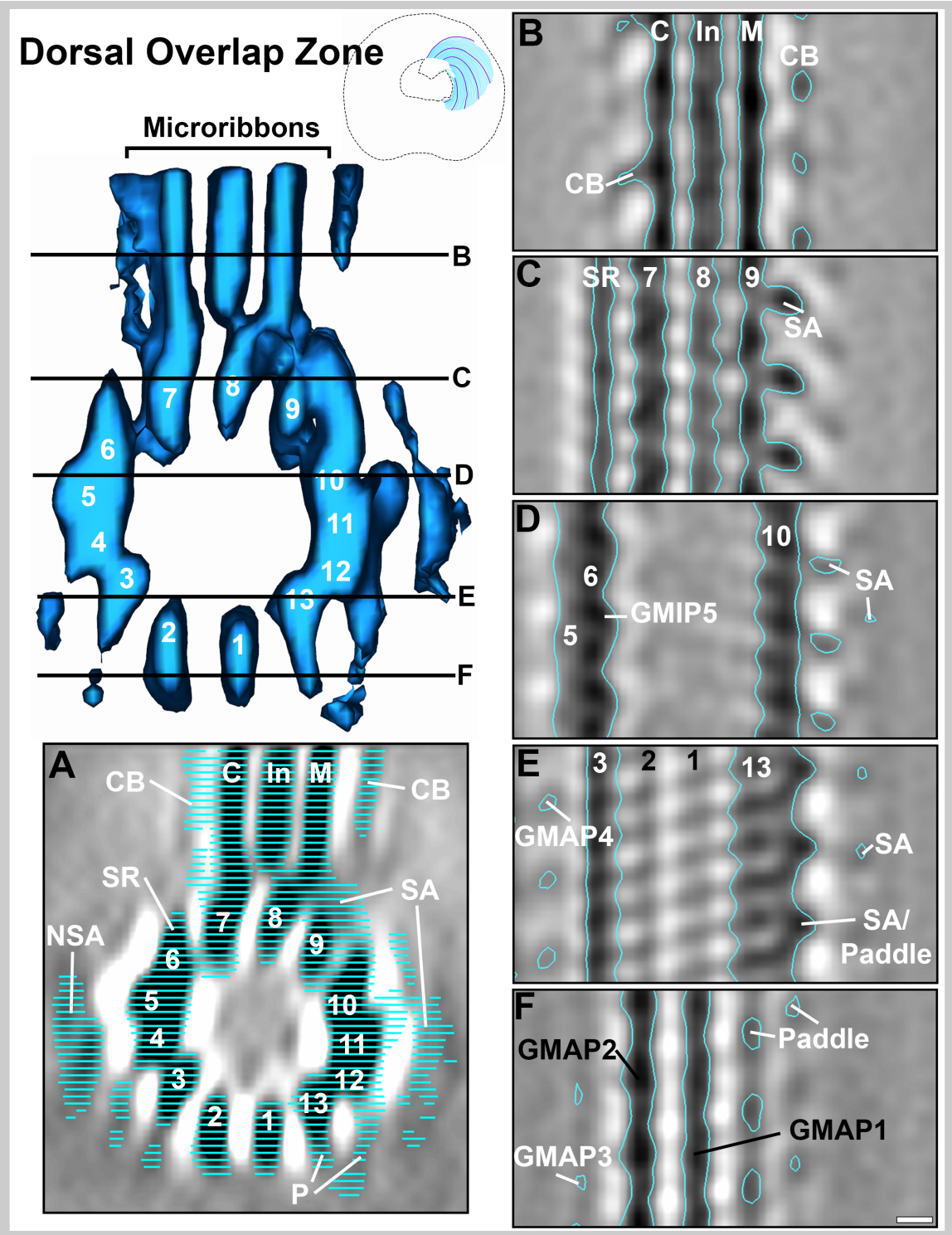


Figure 5.2: 3-D density map of the DOZ produced by subvolume averaging. An isosurface representation has been used to show the location of longitudinal sections through the structure. The PFs are numbered 1 through 13. **Scale bar = 3.8 nm** for all panels and is located in Panel F. **Panel A:** A 54.3 nm thick slice of the average 3D density map in cross section. The isosurface model is overlaid onto the data to show what is included and excluded from the model. Some structures have been labeled: CB = crossbridges, C = center-facing sheet, In = inner facing sheet, M = margin-facing sheet, SR = side-rail, SA = side arm, NSA = neighboring side arm, P = paddle. The NSA is very close to a density projecting from PF4. This might represent a connection between neighboring MTs. **Panel B:** 7.8 nm thick longitudinal slice through the 3D density map of the average volume. The three trilaminar sheets of the MR are well represented. Residual densities of the crossbridges are present, though their irregularity reduces their size and darkness within the average. **Panel C:** 7.8 nm thick longitudinal slice through the 3D density map of the average volume. PF7, 8 and 9 are clearly visible. A density on the shoulder of the side arm (SA) is visible in the section. The continuous density of the side-rail (SR) is also visible. **Panel D:** 7.8 nm thick longitudinal slice through the 3D density map of the average volume. GMIP5 and the top of PF5 is just entering the section Well represented areas of the side arm density are shown in the isosurface can be seen on the right of the MT. The pale grey color indicates the uncertainty of the structure of this side arm. **Panel E:** 7.8 nm thick longitudinal slice through the 3D density map of the average volume. PF3 and 13 are well represented. The top of PFs 1 and 2 are also visible. A density on PF4 is represented and labeled GMAP4. This density is only found in the DOZ. On the right of the MT is a density showing where the side arm and paddle merge under PF12. **Panel F:** 7.8 nm thick longitudinal slice through the 3D density map of the average volume. The end point of GMAP3 is visible on the left side of the MTs. GMAP2 is labeled and has approximately 3 repeating units within the volume, indicating it occurs with a repeating frequency of 8 nm. GMAP1 is visible and appears to be more or less continuous along PF1. The DOZ the paddle appears to be composed by two densities, there maybe be a connection between them, but it is so weakly represented in the density map that it does not appear in the isosurface. **Scale bar = 3.8 nm.**

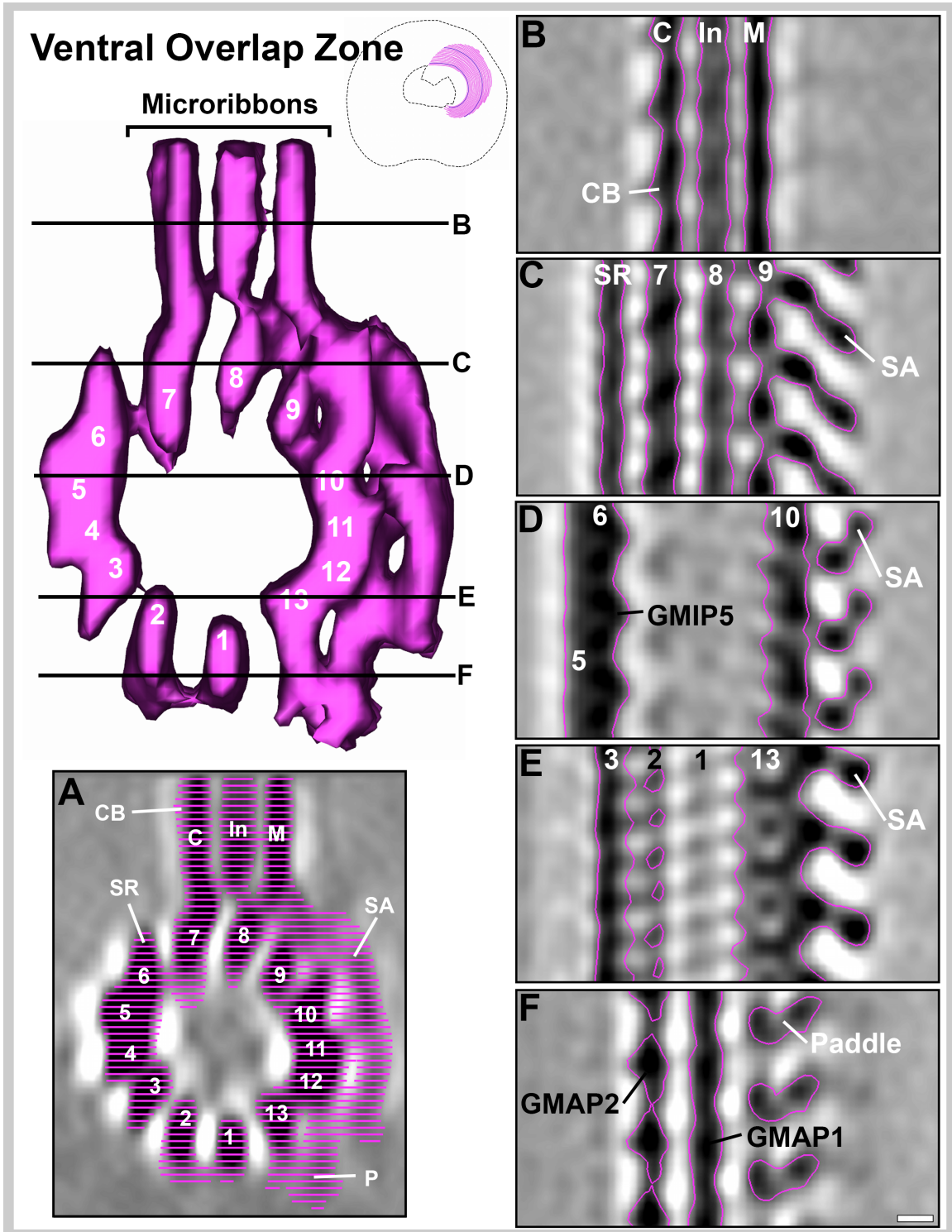


Figure 5.3: 3-D density map of the VOZ produced by subvolume averaging. An isosurface representation has been used to show the location of longitudinal sections through the repeating unit structure. The PFs are numbered 1 through 13. **Scale bar = 3.8 nm** for all panels, located in Panel E. **Panel A:** A 54.3 nm thick slice, a summation of the entire volume, of the average 3D density map in cross section. The isosurface model is overlaid onto the data to show what is included and excluded from the model. Some structures have been labeled: CB = crossbridges, C = center-facing sheet, In = inner facing sheet, M = margin-facing sheet, SR = side-rail, SA = side arm, and P = paddle. The extensive size of the side arm density can clearly be seen on the right of the MT. There is no neighboring side arm present, likely due to the increased distance between the MTs. **Panel B:** 7.8 nm thick longitudinal slice through the 3D density map of the average volume. The three trilaminar sheets of the MR are well represented. Residual density of the crossbridges is present, though the irregularity reduces their size and darkness within the average, so much so that density is only really visible on the center-facing sheet. **Panel C:** 7.8 nm thick longitudinal slice through the 3D density map of the average volume. PF7, 8 and 9 are clearly visible. The continuous density of the side-rail (SR) is also visible. A large density on the shoulder of the side arm (SA) is visible pointing towards the minus end of the MT. **Panel D:** 7.8 nm thick longitudinal slice through the 3D density map of the average volume. PF6 and 10 are clearly visible. The very top of PF5 is just entering the section. The GMIP5 density is also just entering the section. The side arm is still clearly visible on the right side of the MT. It occurs with a repeat frequency of 8 nm, but is shifted relative to the PFs. It appears to occur at each $\alpha\beta$ tubulin dimer interface. At this level, the proteins point towards the plus end of the MT. **Panel E:** 7.8 nm thick longitudinal slice through the 3D density map of the average volume. PF2, 3 and 13 are well represented. The top of PF 1 is also visible. The density of PF4 seen in the DOZ is completely absent. On the right of the MT is the bottom of the side arm, where it merges with the paddle. It is still much larger than the density present at the same position in the DOZ. **Panel F:** 7.8 nm thick longitudinal slice through the 3D density map of the average volume. GMAP2 is labeled and has approximately 3 repeating units within the volume, indicating it occurs with a repeating frequency of 8 nm. GMAP1 is visible and appears to be more or less continuous along PF1. The paddle has two clear densities, with additional connecting density that is sufficiently strongly represented to be included in the isosurface. **Scale bar = 3.8 nm.**

In order to compare and contrast the averaging results, isosurface models were generated from each averaged volume. An isosurface is a smoothed 3D space-filling representation of the data in the 3D density map. A threshold value is set for inclusion in the isosurface. In this case inclusion in each isosurface model was set so that as much of the visible densities as possible were included in each isosurface representation (see Figure 5.4 and Figure 5.5), without introducing model contours containing nothing but noise (light grey) or holes or averaging artifacts (white). The fit of each isosurface model to the data is shown in the cross sections through the averaged volumes.

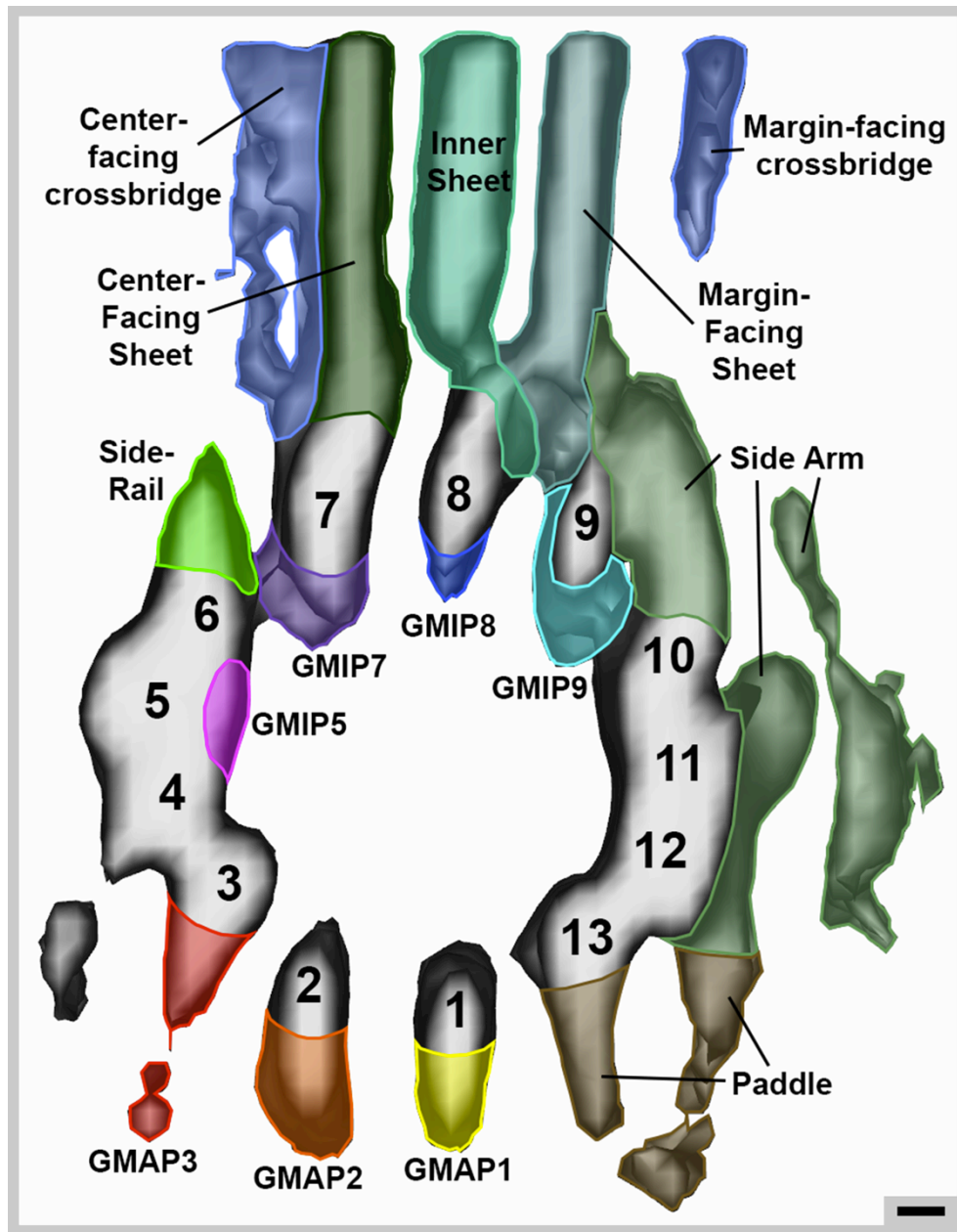


Figure 5.4: Isosurface representation of the DOZ repeating unit structure in crosssection. The PFs are numbered 1 to 13. Distortion of the PFs due to missing wedge artifacts can be seen, causing an elongation of their density along the Z-axis. This likely affects other densities in the structure as well. The densities decorating the MT have been colored to correspond to the color scheme used in the disc body average structure. The reduced size of the side arm in the DOZ is obvious in this representation. The density in the center of the paddle is so poorly represented in this region that it is not included in the isosurface. The trilaminar sheets are visible in the structure. The crossbridges are not well represented, with only small residual structures present. GMAP1 and GMAP2 are both fairly small in size. GMAP3 has an extra density extending from PF3 that is not present in other regions. The density on PF4 has not been colored as it does not appear in another other regions. GMIP5, which is easy to see in the density map is hard to distinguish from the PF in the isosurface, however the extra density in this area accounts for this protein. The side rail is not connected to the crossbridge or center-facing sheet of the MR in this structure. GMIP7 and GMP8 are small densities on the inner surface of PFs 7 and 8. GMIP9 is larger in the DOZ than in other regions of the ventral disc. **Scale bar = 3.8 nm.**

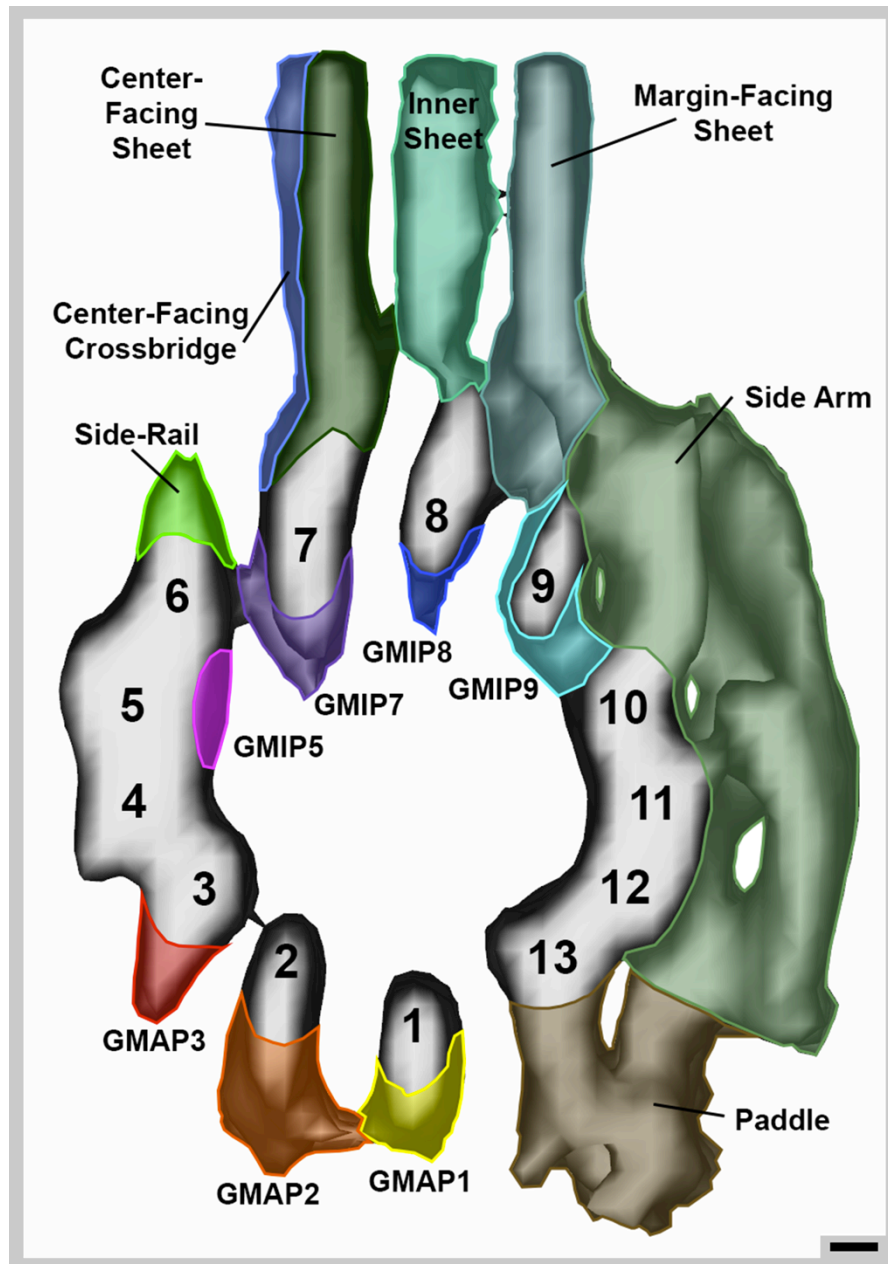


Figure 5.5: Isosurface representation of the VOZ repeating unit structure in cross section. The PFs are numbered 1 to 13. A slightly less severe distortion of the PFs by missing wedge artifacts can be seen in this structure. This effect is less severe in the VOZ as increased curvature at the end of this region fills in the missing wedge more fully. The densities decorating the MT have been colored to using the color scheme from the disc body average structure. The side arm in the VOZ is extensive and bulky, similar to the disc body. The density ends near PF12 and 13, it does not continue down next to the paddle. The paddle is larger and more bulky in the VOZ. There is a visible connection between the two main densities which compose the structure. The short trilaminar sheets are visible in the structure. The crossbridges are very poorly represented, only small residual structures can be seen. GMAP1 and GMAP2 are connected to each other. This connection is not observed in any other region. GMAP3 is smaller in the VOZ than the DOZ. GMIP5, which is easy to see in the density map is hard to distinguish from the PF in the isosurface, however the extra density in this area accounts for this protein. The side rail is not connected to the crossbridge or center-facing sheet of the MR in this structure. GMIP7, GMIP8 and GMIP9 are smaller in this region than in other disc locations. **Scale bar = 3.8 nm.**

Comparison of the Repeating Unit Structures of the Dorsal Overlap Zone and the Ventral Overlap Zone

The center of the repeating unit structure of both the DOZ and the VOZ is a 13 PF MT (Figure 5.2, Figure 5.3, Figure 5.4 and Figure 5.5). The MTs in both volumes are not perfectly round and there is a loss of resolution of the individual PFs along the Z-axis due to the missing cone of data. The cross-sectional ellipse of the MT could also result from the deformation of cylinder by extensive decoration by bound proteins.

The Microribbons

The largest structures attached to the MTs in both the DOZ and the VOZ are the MRs (Figure 5.2, Figure 5.3, Figure 5.4 and Figure 5.5). Trilaminar sheets are well represented in both of these regional averaged volumes (Figure 5.2, Panel B and Figure 5.3, Panel B); however the MR densities of the VOZ repeating unit are short enough to fit completely inside the 54.25 nm x 54.25 nm x 54.35 nm box used to define the subvolume. The MRs of the DOZ (like those of the disc body [84] and margin) extend most far beyond the confines of the box. It was decided that a uniform volume should be used for all of the ventral disc regions, so that the results of each average would be comparable. The additional length of the MR extending out of the box was not included in the final average and did not contribute towards alignment of the subvolumes in the average.

The Crossbridges

The DOZ and VOZ both have residual crossbridge densities present on the center and

margin-facing sheet (Figure 5.2, Panel B and Figure 5.3, Panel B). The crossbridges that are strongly represented enough to appear in the isosurface representation (Figure 5.4 and Figure 5.5) occur at a repeat frequency of 16 nm. The crossbridges are better preserved and more regularly shaped in the DOZ, most likely because they are shorter and there are more intact crossbridges included in the final average and can be seen with a repeat frequency of 16nm, as was observed previously. The crossbridges on the right hand side of the MR in the DOZ, and those in the VOZ are poorly represented and appear to occur at a repeat frequency of 8 nm. They are likely forced into this frequency as they are poorly represented in the structure. This lack of good representation of the crossbridges could be due to irregularity of the presence of crossbridges, due to breakages during extraction or because the angle of connection can vary leading to poor re-enforcement during averaging.

The Side Arms

Another large density is the side arm, a density which represents the only other feature visible in cryo-ET without subvolume averaging (Figure 5.1, Panel C and D). The side arm is located on the margin side of outer surface of the MT. This density extends from PF9 to PF12, joining PF9, PF10, PF11 and PF12 (Figure 5.4 and Figure 5.5).

The VOZ has a large and extensive side arm (Figure 5.3, Panel C, D and E) that is similar in size and shape to the side arm found in the disc body [84]. Both the VOZ and the DOZ are missing an extension in the side arm that is only found in the disc body [84] (See Chapter 1, Figure 1.5). In the disc body, this extension hangs down from the outer

side arm, parallel with the paddle [84].

The side arm that exists in the DOZ is much smaller (Figure 5.4) than in both the disc body and the VOZ. Substantial amounts of density are missing between around PF10, PF11, and PF12, leaving a smaller arm extending from a projection coming from PF11 (Figure 5.2, Panel C, D and E). It might be that close packing between the MTs within the DOZ means there is not enough space to accommodate the larger side arm, limiting the size of the structure.

However, it could be that, unlike in other regions, the side arm of one DOZ MT is physically connected to its neighbor (Figure 5.2, Panel A). There is an additional density on PF4 that is unique to the DOZ. Figure 5.2, Panel A, shows an average of all the slices in the regional average volume. On the left side of the structure is the side arm from the neighboring MT. This density may be connected to an extension that projects from PF4 (Figure 5.2, Panel E), which is not present in other regions of the disc. A faint connection can be observed in the density map, but it is below the threshold for inclusion in the isosurface representation. It is likely that this connect averages poorly as the neighboring MT does not align well with the repeat of the center MT. Also, most of the neighboring MT is masked out during alignment so it cannot contribute to the final solution. It is also possible that the density on PF4 represents a new GMAP, which we could name GMAP4. This density could represent DAP17090 or DIP13, which is only located in the OZ (Chapter 4, Table 4.3).

The Paddle

The paddle is a density of significant size that extends towards the ventral surface of the cell (Figure 5.4 and Figure 5.5). The paddle descends from PF13 and from the bottom of the side arm on PF12 (Figure 5.2 and 5.3) in all three regional repeating units, every 8 nm, but slightly off-set from the α/β tubulin dimers, along the MT. The paddle in both the DOZ and VOZ is smaller than in the disc body [84]. Approximately half the volume of this density is missing in the overlap zone regions. The DOZ, is also missing density from the center of the paddle (Figure 5.2, Panel F). It gives the appearance that two distinct densities, connecting to form a loop, compose the paddle in this region.

Intra-region variation

Both the paddle and the side arm in both the DOZ and VOZ represent variable structures within the repeating units. This variability is indicated by the lighter color of the densities of these structures within the 3D density map (Figure 5.2, Panel A, C, D, E, and F; Figure 5.3, Panel A, C, D, E and F). Structures that are variable within a region, meaning that they are different in each individual subvolume, are not enhanced as well with subvolume averaging, and therefore do not appear as dark in the average volume.

The intra-regional variation observed in the side arm and paddle could manifest in several ways. The structures could be composed of different proteins, even within the same region. This seems unlikely as only two DAPs are known to localize specifically to the overlap zone (Chapter 4, Table 4.3). Another alternative is that the side arm and paddle occur with a repeat frequency greater than 8 nm. This again, is an unsatisfactory

explanation as the side arm can actually be observed with a regular repeat frequency of ~8 nm in the un-averaged tomograms.

This leaves two possible explanations: the first is that the large side arm and paddle structures exist in multiple conformational states or there are subsets of structures at this loci on the MT; the second explanation is that the side arm and paddle are angled differently in each repeating unit due to the curvature of the MTs. This would have a significant effect on the representation of these structures in the density map, especially in the DOZ, where the curvature of the MTs is high.

It could be that the side arm and paddle are involved in imparting curvature to the MTs of the ventral disc. Further details about side arm and paddle structure could be elucidated from this data by the production of subclasses of subvolume averages, based on the curvature value of each subvolume center point. Ideas on how to carry this out are discussed in chapter 6.

GMAPs

There are several smaller densities bound to individual PFs on the outer surface of the MT in both the DOZ and VOZ repeating unit (Figure 5.4 and Figure 5.5). Most of these densities which appear to be close to the size of tubulin are named *Giardia* microtubule associated proteins (GMAPs) and, with the exception of the side-rail, numbered by the PF on which they are located.

The GMAP densities including GMAP1, GMAP2, GMAP3 and the side-rail, on PF6, are present in the DOZ, the disc body, and the VOZ. GMAP1 and GMAP2 are smaller in the DOZ repeating unit than in any other structure (Figure 5.4). However, GMAP3 is larger and there is an extra density on PF4, which will be referred to as GMAP4 (Figure 5.2, Panel A, E and F). It might be that these two densities are involved in binding and linking neighboring MTs. In the VOZ, GMAP1 is smaller than in the disc body and GMAP2 is significantly larger. These two densities are in very close proximity, which is not observed in any of the other regional structures (Figure 5.5). GMAP2 does not correspond to the same repeat frequency as most of the other densities in the structure. Its axial repeat frequency of incorporation along PF2 is approximately every 16 nm, corresponding to every other α/β tubulin dimer (Figure 5.2, Panel F and Figure 5.3, Panel F).

The side-rail in both the DOZ and VOZ (Figure 5.2, Panel C and Figure 5.3, Panel C) is similar in size and is significantly smaller than the density observed in the disc body [84]. The bridge, which is present in the disc body, connecting the side-rail to the center-facing MR sheet, is completely absent from both the DOZ and the VOZ repeating unit.

GMIPs

While the majority of MT associated density is on their outer surface, there are also densities bound to specific locations on the inner surface of the MT (Figure 5.4 and Figure 5.5). They have been named *Giardia* microtubule inner proteins (GMIPs) and, again, are named by the PFs to which they are attached. The densities include GMIP5,

GMIP7, GMIP8 and GMIP9. In both the DOZ and VOZ repeating units, GMIP7 and GMIP8 are reduced in size relative to the densities observed in the disc body [84]. GMIP9 in the DOZ is larger than the density observed at the same location in the VOZ and disc body.

GMIP5 is one of the most dominant densities in all three of the averaged volumes. GMIP5 is located at PF5, coming up into contact with PF6 (Figure 5.2, Panel D and Figure 5.3, Panel D). GMIP5 is approximately the same size as a tubulin monomer and is very regularly sized on every repeating unit on all four regions of the disc that were averaged.

Summary of Observed Differences in the Decorating Densities

The results of the comparison between the average volumes from each region of the disc have revealed some differences between the regions (Table 5.1). In general, the differences that exist between the regions are subtle. Most of the same densities appear to be present at the same locations in the structures, though there are variances between the size and shape of the densities present.

Structure	Dorsal Overlap Zone	Disc Body	Ventral Overlap Zone	Margin
Microribbons	Trilaminar sheets	Trilaminar sheets	Trilaminar sheets	Different structure, angled
Crossbridges	Visible both sides	Visible both sides	Only on margin-facing sheet	Large, blade-like, on margin facing side
Side arm	Small	Largest	Large	Smallest
Paddle	Small ring-like	Largest	Smaller	Absent
GMAP1	Present	Present	Present, connected to GMAP2	Absent
GMAP2	Present	Present	Present, connected to GMAP1	Present, connected to GMAP3
GMAP3	Present	Present	Present	Present, connected to GMAP2
GMAP4	Present	Absent	Absent	Absent
Side Rail	Present	Large	Present	Large
Bridge	Absent	Present	Absent	Absent
GMIP5	Present	Present	Present	Present
GMIP7	Present	Present, connected to GMIP8	Present	Small
GMIP8	Present	Present, connected to GMIP7	Present, small	Small
GMIP9	Present, large	Small	Present, large	Absent

Table 5.1: Summary of the structural differences that exist between the DOZ, the disc body, the VOZ, and the margin. Information obtained from this study and from C. Schwartz et al, 2012 [84].

Identification of the Core Repeating Unit of the Ventral Disc

The results of the subvolume averaging produced structures for each region that were remarkably similar. It seems likely that the hypothesis that a basic unit that occurs throughout the ventral disc is correct. In order to test this hypothesis further and attempt to identify the structure of the core unit, further alignment and comparison of the different repeating unit structures were performed.

PEET was used to align, but not average, all four (DOZ, disc body, VOZ and margin) repeating unit volumes based on the strongest features in each 3-D density map, such as PFs and MRs. This was possible since the four regional structures have many features in common. Alignment placed all the average volumes in identical orientations relative to the MT, so that areas of commonality between them could be determined.

The grayscale of the aligned averages were then normalized to the grayscale in the disc body average. This produced density maps with similarly distributed means and standard deviations, representing the densities in each map. A threshold of 1σ below the standardized mean was defined. All voxels dark enough to fall within this value were given a binary value of 1. All voxels above the threshold were assigned a binary value of 0.

The binary density maps from each region were then used to produce a binary structure containing all the common features from all four regions. The volumes were assessed voxel by voxel. If a particular voxel had a value of 1 in each regional binary structure, it was assigned a value of 1 in the common core structure. If a voxel failed to have a value of 1 for any of the regional averages, it was assigned a value of 0, effectively not appearing in the final common core structure. The binary common core repeating unit is shown in Figure 5.6. The isosurface model contours of the DOZ and VOZ have been overlaid to indicate how the common core structure fits within each regional unit (Figure 5.6).

Structural features in the common core repeating unit

Only a few structural features were found to be of sufficiently low variability, within and between the regions, to be included in the common core structure. As expected, the PFs of the MT were well represented.

Only two of the three sheets of the MRs were well represented in the common core structure. The Inner sheet and the Margin-facing sheet were both well represented, with slightly reduced sizes indicating that some variability exists. The center-facing sheet is poorly represented indicating this structure is more variable than expected.

Much of the variation that exists in the MRs comes from the margin repeating unit structure. The MRs in the Margin repeating unit are angled relative to the MT, and only two MR sheets are present. The Margin also contains large blade-like crossbridges that

extend out from the angled MRs. This difference in structure likely accounts for why the crossbridges are not represented as a common feature, despite their presence in five of the six ventral disc regions.

The Common Core Structure

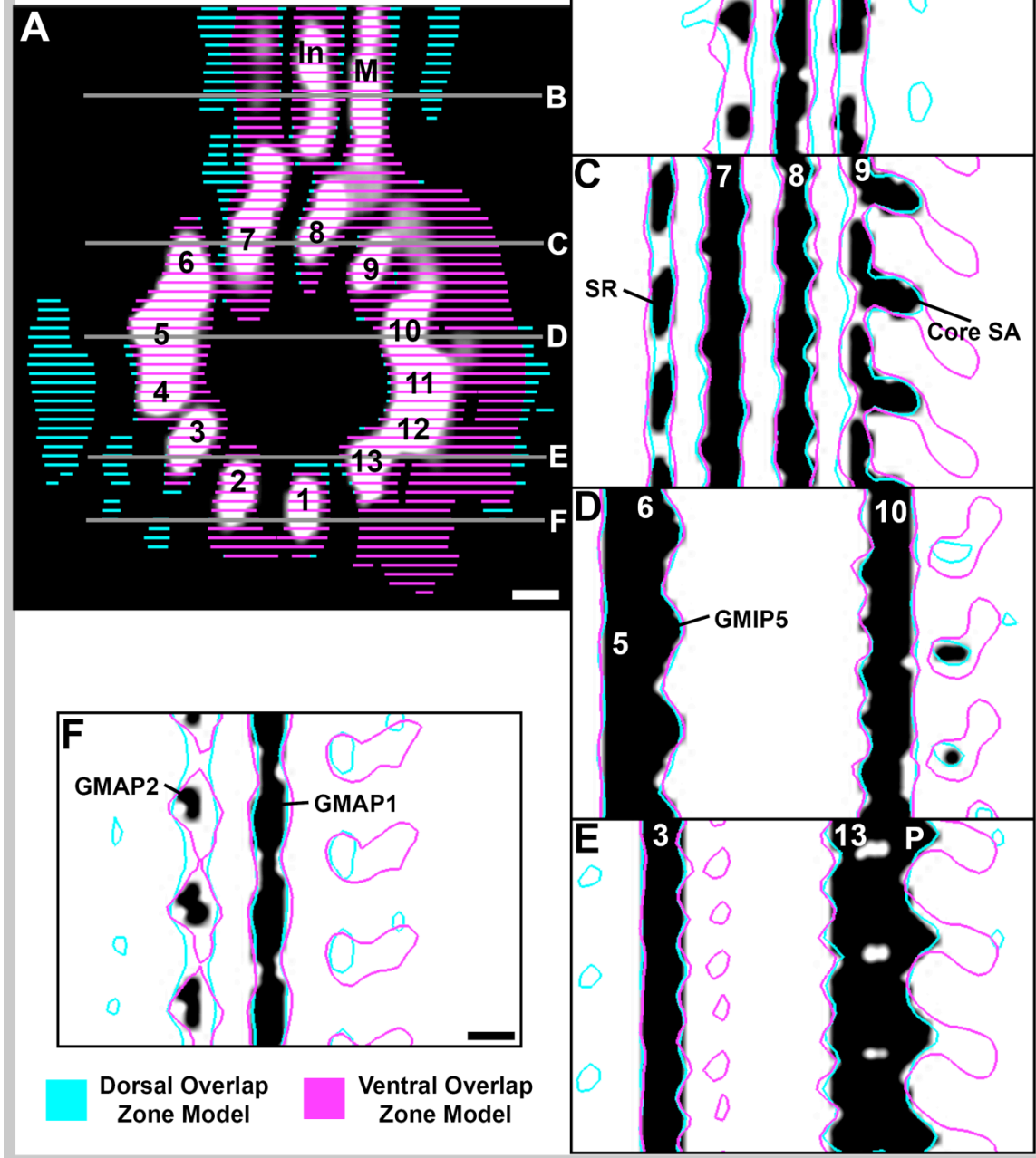


Figure 5.6: Binary 3-D density map of the common core structure of the ventral disc. Panel A: A 54.3 nm thick cross section of the binary common core density map. The PFs are numbered 1 to 13, In = inner sheet, M = margin-facing sheet. The common densities are shown in white. Grey densities demonstrate less well represented areas of the structure. The isosurface model contours have been overlaid on the structure to show how the common core fits inside each regional structure. The positions of the longitudinal sections in panel B to F are indicated by the lines and letters. **Scale bar = 3.8 nm. Panel B to F:** 0.78 nm thick longitudinal sections through the common core structure. The density is shown in black. C = center-facing sheet, SR = side-rail, SA = side arm and P = paddle. The contours of the DOZ and VOZ isosurface models have been overlaid onto the binary structure. **Scale bar (located in Panel E) = 3.8 nm.** It is clear that a lot of the decoration on the PFs is missing from the common core structure. The exception is GMIP5, which fits almost exactly to both the DOZ and VOZ model. This density is also well represented in the disc body and margin structural repeating units.

A lot of the structural features found in the regional repeating unit are not well represented in the common core structure. Most of the smaller densities including: GMAP1, GMAP2, GMAP3, GMAP4, GMIP7, GMIP8, GMIP9 and the side-rail, are dramatically reduced in size or are not present. The side arm and paddle are much smaller. A core side arm can still be seen connecting PF9 and P10, with a small density remaining on PF11.

One of the only well represented features in the common core structure is GMIP5. This density is also strongly represented in all four of the regional averages. The GMIP5 density appears to localize on every 8 nm repeat in the ventral disc regions that were imaged using cryo-ET and appears to be approximately the same diameter as tubulin.

The lack of representation of the repeating structural elements that appear to be similar across the four regions, again suggests that there is both inter-regional and intra-regional variation in these structures. Intra-regional variation would result in a voxel failing to meet the threshold for inclusion in the regional binary structure. Inter-regional variation would mean it would not be included in the common core structure because it fails to appear in all four regions.

When this result is taken in the context of the lack of region specific DAPs, it suggests that the regional differences arise, not from the presence of different region-specific proteins, but from variance in the frequency of incorporation; possible variance in PF location in the repeating unit, or different conformational states of the same group of 17

DAPs. For example, it might be that varying the frequency, location, or conformational state of certain structural proteins alters the flexibility of the MT, affecting the local curvature.

If structural differences between regions arise due to the variable incorporation, or localization of a core set of proteins within the repeating units. Ventral disc biogenesis must be an extremely tightly regulated process to ensure that each of the proteins is incorporated at the correct frequency or location in the repeating unit structures along a single MT, that occur in specific localizations or regions within the larger array.

Results Summary and Discussion

Cryo-ET and subvolume averaging has demonstrated that the variation observed in the coarse structures of the ventral disc regions extends to the fine protein structures of the DOZ and VOZ. Subvolume averaging allows the visualization of smaller protein densities decorating both the outer and inner surface of the MT. This decoration cannot be distinguished from noise in a signal subvolume, without using averaging to enhance the signal-to-noise ratio and therefore revealing greater resolution.

The MTs in the DOZ and VOZ are highly decorated. The locations of the decorating densities are conserved in both of these regions, though the apparent size and shape of the densities changes. This change could be due to the presence of different region specific

proteins. However, given that there are very few proteins unique to each region, it is more likely due to alterations in frequency of incorporation, PF location, or conformational state of each of the core DAPs in each region.

Intra-regional variation in both the DOZ and VOZ are visible in some areas of the structure. The outer areas of the side arm and the paddle are both “hot spots” of variation within these structures. There are multiple explanations that could account for the variation observed. It is possible that the curvature of the MTs, and the angle at which the side arm extends from the MT result in a poor alignment of these structures.

Conversely, the side arm structures may be important for imparting curvature to the MTs, and vary in structure as curvature varies along the length of a MT. It is also possible that these large structures are just more flexible, or naturally exist in multiple conformational states.

When the average volumes from the DOZ, the Disc Body, the VOZ and the margin are aligned to generate a structure containing only densities shared by all four regions the result produces a small common core structure lacking much of the decoration observed in the regional structures. This suggests that only a few proteins localize to every 8nm repeat throughout the ventral disc.

The lack of decoration in the common core structure aligns well with the finding that there are few regionally unique proteins. Instead, it suggests that the variations observed

between the subvolume averaging structures results more from differences in protein incorporation rather than the inclusion of different very wide variety of DAPs in the same location.

An attractive explanation for the variation within and between the 4 ventral disc regions is variability in frequency of incorporation of the core set of DAPs. For example, the protein or protein complex that is represented by GMAP2 is smaller in the DOZ than in the VOZ and disc body. If the protein or protein complex is incorporated only once every 16 nm, or infrequently, with no regular repeat rather than 8nm or is incorporated infrequently, it will appear smaller in the final average structure.

A change in incorporation frequency of a set of core DAPs might provide a model for the smooth modulation of factors such as MR height and MT curvature throughout the array and could explain why the densities observed still occur in the same location in different regions, and vary principally in size and shape. Also, because the MTs are curved along their length it is likely that there are deformations at the interfaces between the tubulin monomers, tubulin dimers and/or neighboring PFs compared to a straight MT. These defects would create center-facing and margin-facing molecular recognitions sites for specific proteins and could explain why features such as the side arms are always assembled on the margin-facing wall of the MTs.

If the regional variation observed in both the coarse and fine structures of the ventral disc are largely due to variable incorporation of a single set of core proteins, this variability

means that the same proteins must be incorporated at different frequencies, along a single MT; therefore the process of assembly must be very tightly regulated.

The presence of MIPs in the ventral disc suggests that at least some of the DAPs must be incorporated as the MTs are polymerizing. The MTs of the ventral disc do not depolymerize until the new daughter discs begin to assemble [76]. The lumen of the MT is ~12 nm in diameter [168]. If MIPs were not incorporated into a growing MT, they would have to be transported up to 18 μm , down the longest MTs, and placed into the correct position. This seems very unlikely as no motor proteins were detected in the proteomic analysis of the ventral disc components [121] and no motor proteins have been localized to the ventral disc with GFP tagging [121]. Alternatively, the MTs would have to open in a controlled manner, after assembly to allow MIPs to enter.

GMIP5

One of the most well represented features in the Common Core structure is GMIP5. This density is strongly represented in all four of the regional averages. The GMIP5 density appears to localize on every 8 nm repeat in the ventral disc regions that were imaged using cryo-ET and appears to be approximately the same diameter as a tubulin monomer.

Using the structural information obtained in this study, we can narrow down the list of known DAPs that might be candidates for GMIP5 (Table 5.2), assuming that it is composed of a single protein and that this density is the result of the same protein in each regional structure. First, all DAPs that do not localize to the DOZ, the disc body, the

VOZ and the margin can be excluded, leaving a list of 19 DAPs. Next, proteins with a known function in the ventral disc can be excluded. This step excludes tubulin, which is known to be the structural component of the MTs [169,170,171]. Beta-giardin, Delta-giardin, Gamma-giardin, and SALP-1 are also excluded, as these proteins are known to localize the MRs [114,115,121,172]

Assuming that GMIP5 is truly a very well represented density, which it appears to be, it is similar in diameter to the tubulin monomers. In *G. lamblia*, alpha-tubulin is 51 kDa [94,121] and beta-tubulin is 50 kDa [94,121]. To allow for the possibility of different oligomeric states of a protein that composes GMIP5, only very large proteins (over 100 kDa) will be excluded next. As many of the known DAPs are large, this leaves only six candidates. All of these remaining proteins contain motifs known to bind to other proteins or MTs [173,174,175,176,177].

Using structural information, the candidates for *in vitro* experimentation to identify GMIP5, have been narrowed significantly (ideas for how this could be achieved are discussed in Chapter 6). The identity of a MIP has yet to be positively determined, and the conformation of a MIP binding site for the inner MT surface is still unknown [103,105]. There is also the possibility that, because of its ubiquitous incorporation into the ventral disc repeating units, this protein plays an important role in the structure or stability of the ventral disc. It could provide an excellent target for the development of new anti- giardia drugs. Identifying this density should be a high priority as it is likely to play an important structural role.

DAPs on all four ventral discs regions	DAPs with no known function in <i>Giardia</i>	DAPs (Below 100 kDa)	DAPs with a known protein-protein interaction motif	Starting list of GMIP5 candidates for testing
Alpha-2 tubulin	Alpha-2 tubulin	Alpha-2 tubulin	Alpha-2 tubulin	
Beta tubulin	Beta tubulin	Beta tubulin	Beta tubulin	
α -2 annexin	α -2 annexin	α -2 annexin	α -2 annexin	α -2 annexin
α -3 annexin	α -3 annexin	α -3 annexin	α -3 annexin	α -3 annexin
α -5 annexin	α -5 annexin	α -5 annexin	α -5 annexin	α -5 annexin
α -17 annexin	α -17 annexin	α -17 annexin	α -17 annexin	α -17 annexin
Beta- giardin	Beta- giardin	Beta- giardin	Beta- giardin	
Delta- giardin	Delta- giardin	Delta- giardin	Delta- giardin	
Gamma-giardin	Gamma-giardin	Gamma-giardin	Gamma-giardin	
SALP-1	SALP-1	SALP-1	SALP-1	
DAP16279	DAP16279	DAP16279	DAP16279	
DAP103807	DAP103807	DAP103807	DAP103807	
DAP92498	DAP92498	DAP92498	DAP92498	
DAP 5010	DAP 5010	DAP 5010	DAP 5010	
DAP5374	DAP5374	DAP5374	DAP5374	DAP5374
MBP	MBP	MBP	MBP	
DAP13766	DAP13766	DAP13766	DAP13766	DAP13766
DAP17053	DAP17053	DAP17053	DAP17053	
DAP17097	DAP17097	DAP17097	DAP17097	

Table 5.2: Using structural information to narrow down the GMIP5 candidate proteins.

CHAPTER 6: FINAL CONCLUSIONS AND DISCUSSION

This research has provided a wealth of new information about the organization of the ventral disc array in *G. lamblia*. The use of large scale 3D reconstruction of negatively stained extracted ventral discs has provided information on the exact path of each MT in the array, leading to new information on the total number, length and organization of MTs within the large structure.

It was discovered that almost the entire ventral overlap zone is formed from MTs that nucleate on the center edge of the array. Deletion of all center edge MTs from the model closely resembles the patterning observed in the ventral disc when MBP is knocked down. Knockdown of MBP results in impaired attachment of the trophozoite cell. This result has led to new avenues of research that may provide the starting point to discover the function of MBP in the ventral disc and the future development new drugs to treat *Giardia* infection.

It was also discovered that this array is not structurally uniform. The MT curvature, length of crossbridges, MT spacing, and MR morphology, alter depending on the area or region of the disc. This means that changes in the structure of the MT decoration occurs along the length of an individual MT, indicating a complex assembly process.

Structural variation was also found to exist within the smaller decorating structures that compose the repeating units of the disc, both within and between different ventral disc

regions. Variation was found largely to exist in the size and shape, but on location on the PFs of the MTs. This made it possible to align the regional repeating unit average volumes to obtain a common core structure for the ventral disc. The common core structure appeared to be lacking much of the decoration observed in the regional repeating units.

The lack of decoration in the common core structure and the variability in density size, but not location in the regional repeating units suggests that both intra- and inter-regional variation is created by variable incorporation of the different DAPs in different ventral disc regions. This result explains how a great deal of structural variation can be created from a small set of proteins found to localize to all regions of the disc. It is possible that changes in frequency of incorporation or location of incorporation within the repeating units, of specific DAPs, could modulate MT curvature, length and type of crosslinking between MTs and MRs, allowing the large array to be constructed from as few different protein components as possible. *In vitro* methods for testing this hypothesis are discussed below.

The regional structures from the DOZ, disc body, VOZ and margin were all found to contain MIPs bound to specific PFs. Only one MIP was found consistently, in all four regions, with very little variation in size and shape. The density is attached to PF5 and is known as GMIP5. This density was the only MIP that was strongly represented in the common core structure and was found to be approximately the size of a tubulin monomer. GMIP5 occurs with a repeat frequency of 8nm, suggesting that its binding is

controlled or modulated by the repeat length of the $\alpha\beta$ tubulin dimer. This protein could play an important role in the structure or function of the ventral disc as it seems to be ubiquitous through the regions examined.

The identities of the protein component or components of GMIP5 are still unknown. However, using information from the structures obtained in this study, the pool of known DAPs that could compose GMIP5 has been narrowed down from thirty-two proteins to only six. This will provide a good starting point for further investigation of this structural component.

It is hoped that this work will serve as a foundation and a context for further research into the structure and function of the ventral disc, the processes of ventral disc assembly, and eventual identification of the proteins that compose the ventral disc subunits.

If I had another five years...ideas for further research

Construction of curvature class averages

It was not clear whether the variation in the size and shape of the side arm both within and between different ventral disc regions was due to changes in conformation of this structure, differential occupancy, or poor alignment of the density due to curvature of the MT.

The work presented here has resulted in the development of a protocol for determining the curvature of each point in a contour. It would be simple to apply this and determine the exact curvature value for each point used to define a subvolume in the cryo-ET data. This would allow a very new feature of PEET to be used. This feature allows the production of class averages from select subvolumes in the original average. Class averages could be constructed from subvolumes with center points that have been assigned curvature values within a narrow range. This would reveal if the side arm conformation is related to curvature of the MT or provide a better average if curvature is preventing a good alignment from being obtained. Since this data is already available, these class averages will likely be included in a publication of the work.

Investigation of the MBP Morpholino phenotype

The ventral disc models demonstrated that almost all of the MTs are located in the VOZ nucleate on the center edge of the MT. When the center edge MTs are removed from the model, the structure closely resembles the ventral disc phenotype observed in trophozoite cells treated with anti-MBP Morpholinos (Chapter 1, Figure 1.10). This phenotype is known to impair trophozoite attachment [123].

It appears that knockdown of MBP expression may induce the loss of the center edge MTs or MRs, causing the loss or a change in structure of the VOZ, leading to a flattening of the ventral disc array. To test this hypothesis, extracted cytoskeletons that contain the ventral disc phenotype could be imaged using negative stain and large area montage

tomography.

Because the anti-MBP Morpholinos have to be electroporated into cells and they are short acting, the entire population of trophozoites often do not exhibit the phenotype. Since the trophozoites that carry the phenotype have impaired attachment, it should be possible to enrich the concentration of these cells by centrifuging the culture with sufficient force to remove impaired cells, while leaving wild type cells adhered to the culture tube.

Investigating GMIP5 candidate proteins

The six DAPs that are likely candidates to compose GMIP5 could be investigated using *in vitro* methods. The candidate DAPs should be expressed and purified from a recombinant expression system.

The binding of purified proteins to taxol stabilized *in vitro* microtubules could be investigated using cryo-EM to look for the presence of MT decoration. Helical averaging could be used to obtain a structure of the protein if binding to the inner surface was detected [181,182].

If an atomic resolution structure of the DAP could be obtained, either by X-ray crystallography or NMR, a docking experiment could be carried out to orient the atomic structure within the cryo-EM density [181,182]. This procedure might allow not only the identification of the first MIP, but also the structure of the binding site for the inner

surface of the MT.

CHAPTER 7: Material and Methods

Culture of WBC6-M *Giardia lamblia* trophozoite cells

Modified TY-S-33 media

Modified TY-S-33 non-commercial media was produced in the lab as needed. A concentrated 5X media base is made by adding 25 g D-glucose (Sigma-Aldrich, St. Louis, MO, USA), 5 g NaCl (Sigma-Aldrich, St. Louis, MO, USA), 25 g yeast extract (Sigma-Aldrich, St. Louis, MO, USA), and 50 g casein peptone digest (Sigma-Aldrich, St. Louis, MO, USA) to ultra pure deionized (DI) water, which is made up to 500 ml after addition of components. The mixture was then stirred for 30 minutes and subsequently filtered through Whatman filter paper (GE Healthcare Bio-Sciences, Piscataway, NJ, USA) to remove large particulates.

The media was completed by making a cysteine (Sigma-Aldrich, St. Louis, MO, USA) and ascorbic acid (Sigma-Aldrich) solution. 2 g of cysteine and 0.1 g of ascorbic acid were added to 700 ml of ultra pure (DI) water. The pH of the solution was adjusted to pH 7.0- 7.2 using 10 M NaOH. To this solution, 20 ml of 50X phosphate buffer (220 mM KH_2PO_4 , 427 mM $\text{K}_2\text{HPO}_4 \cdot 3\text{H}_2\text{O}$) 200 ml of 5X basic medium, 8ml of 6% bovine bile (Sigma-Aldrich, St. Louis, MO, USA) solution, 3 ml ferric ammonium citrate (Sigma-Aldrich, St. Louis, MO, USA) solution (2.28 mg/ml), 10 ml of 100X Penicillin/Streptomycin (Life Technologies, Grand Island, NY, USA) and 100 ml of adult

bovine serum (Sigma-Aldrich). After thorough mixing the media was then filtered under vacuum through Nalgene Rapid-Flow PES membrane bottle top filters (Thermo Scientific, Waltham, MA, USA) to sterilize. The filters were replaced if the flow reduced to a slow drip. The media was then divided into 50 ml aliquots and stored at -70 °C until use.

Culture of trophozoite cells

WBC6-M giardia trophozoite cells (a kind gift from the Dawson Lab at UC Davis) were cultured in non-commercial modified TY-S-33 media in anaerobic conditions. Cells were cultured in 15 ml culture tubes containing 12 ml of media. Large cultures were grown in 50 ml conical tubes, containing 50 ml of media. The lids of both types of tubes were screwed on tightly to prevent air exchange and protect the cells from excessive oxygen exposure. After bring up a culture from a frozen cell stock, cells were allowed 1 hour at 37°C to recover and attach to the tube surface. After 1 hour, the DMSO containing frozen storage media was removed and exchanged for 12 ml of modified TY-S-33 media. Cells were then allowed to grow to near 100% confluency before splitting the culture.

In order to split the culture, the culture tubes were placed on ice (30 minutes for 15 ml tubes and 45 minutes for 50 ml tubes). As the media cooled, the cells detached from the sides of the tube and formed a suspension in the media. This cell suspension was then diluted to the desired concentration with fresh media. Culture tubes were then returned to 37 °C to allow cells to reattach to the tube.

Freezing and storage of trophozoite cells

WBC6-M cultures were prepared for frozen storage by placing a 15ml culture tube of cells on ice as described above. After the cells detached from the tube walls, the tubes were centrifuged at 900 x g to form a soft pellet. The media was removed and replaced with 2 ml storage media (90% modified TY-S-33 media with 10% DMSO). The pellets were resuspended in the storage media and 1 ml of this suspension was transferred to a cryo-storage vial. The vials were placed at -70 °C for 48 hours and then transferred to LN₂ storage.

Preparation of extracted cytoskeletons

PIPES, HEPES, EGTA, MgSO₄ (PHEM) buffer

1X PHEM buffer was made for a 2X PHEM buffer stock (120 mM piperazine-N,N'-bis(2-ethanesulfonic acid) (PIPES), 55 mM (4-(2-hydroxyethyl)-1-piperazineethanesulphonic acid) (HEPES), 20 mM ethylene glycol tetraacetic acid (EGTA) and 16.5 mM MgSO₄).

Detergent extraction of cytoskeletons

The media was removed from a 15 ml tube of WBC6-M trophozoite cells by decanting. 2 ml of PHEM buffer with 1% triton X-100 was used to wash the cells. This was removed by decanting. 4 ml of PHEM buffer with 1% triton X-100 was added to the tube and the lid was replaced. The tube was inverted for approximately 2 minutes to coat the cells with

the solution. The tube was then placed on a vortex, on low, for 15 minutes. The suspension was then removed from the culture tube and transferred to a 15 ml conical tube and centrifuged at 2500 x g for 5 minutes. The supernatant was removed and the pellet was resuspended in 1 ml PHEM buffer with 1% triton X-100. The new suspension was vortexed for 15 minutes on low. The tube was then placed in a water bath sonicator for 30 seconds. The tube was then placed at 4 °C for 1 hour. After cooling the tube was vortexed and sonicated twice more as described above. The extracted cytoskeletons were then washed to remove the detergent. This was done by centrifuging the cells at 2500 x g for 5 minutes. The supernatant was removed and the pellet was resuspended in 1 ml PHEM. This step was repeated three times. After the final wash, the cytoskeletons were resuspended in 0.5 ml of PHEM and stored for 48 hours at 4 °C.

Preparation of grids for negative stain of extracted cytoskeletons

Preparation of carbon coated formvar grids

A thin layer of formvar was created on a glass microscope slide (Thermofisher Scientific) by dipping a glass slide into 0.7 % formvar resin in ethylene dichloride solvent. The slice was allowed to dry for approximately two minutes and the layer of formvar was cut free of the slide and floated on water. 200 mesh Cu-Ru grids (Electron Microscopy Sciences, Hatfield, PA, USA) were placed copper side down onto the film of formvar. A glass coverslip (Thermofisher Scientific) was used to scoop the grids and formvar layer

through the water. The grids were then gathered on a surface of the coverslip, with the copper/formvar-coated side facing up, and allowed to dry.

A carbon coat was added to the grids by placing the coverslip in a rotary pumped carbon and sputter coater (Electron Microscopy Sciences). Current was passed through a carbon string until an even coat of carbon was applied to the surface of the grids. Just before use, each grid was cut free of the extra formvar.

Preparing negatively stained extracted cytoskeletons

400 ml of extracted cytoskeleton suspension was removed from 4 °C storage and centrifuged at 2500 x g to pellet. The supernatant was removed and the pellet was resuspended in 200 µl of fresh PHEM buffer. The carbon coated grids were glow discharged to impart a negative charge to the surface of the grids. 5 µl of 20 nm gold fiducial colloidal suspension, 7×10^{11} particles per ml (British Biocellular International, Cardiff, UK), diluted 1:2, was added to each grid. After 5 minutes the grids were blotted on the side of the grid, using Whatmann filter paper, and then allowed to dry fully.

The dry grids were then glow discharged a second time and 10 µl of concentrated cytoskeleton suspension was added to each grid. The cytoskeletons were allowed 20 minutes to adhere to the grid in a humid environment at room temperature. The grids were then blotted on the side so they were partially dry. 5 µl of 3% aurothioglucose solution was added to each grid. A torn edge of Whatmann filter paper was then used to blot the front surface of each grid as dry as possible. The grids were then allowed to dry

completely and then placed in a grid storage box at room temperature until use.

Preparation of plunge frozen grids of extracted cytoskeletons

400 μ l of cytoskeleton suspension was removed from 4 °C storage and centrifuged at 2500 x g to pellet. The supernatant was removed and replaced with 70 μ l of fresh PHEM buffer. A concentrated gold fiducial solution was made by centrifuging 1 ml of 10 nm, 5.7×10^{12} particles per ml, gold fiducial solution (British Biocellular International) for 10 minutes at 2500 x g. 850 μ l of supernatant was removed and the gold pellet was resuspended in the remaining liquid. The tube was then placed in a water bath sonicator and sonicated for 2.5 minutes to break up clumps. 4/2/2 C-flat holey carbon grids (Electron Microscopy Sciences) were glow discharge to impart a negative charge to their surface just prior to use.

The Vitribot (FEI) was used to produce the plunge frozen grids. 4 μ l of concentrated cytoskeleton suspension was added to each grid and allowed 30 seconds to adhere in an environment set to 70% humidity. 1 μ l of concentrated 10 nm gold fiducial solution was added to the grid and mixed with the cytoskeleton suspension by pipetting up and down five times. The grid was then blotted using the settings blot force 0 and blot time 2. The grid was then plunge frozen in a 40:60 mixture of liquid ethane and propane. After plunge freezing each grid was transferred to a grid cryo-storage box and stored in LN₂ until imaged.

Imaging in the TEM

All EM data was collected on an FEI Tecnai F30 FEG transmission EM (FEI-Company, Eindhoven, The Netherlands) operating at 300 kV. All tilt stack images were recorded with binning by 2 on 4K x 4K Gatan Ultracam 895 CCD camera (Gatan, Inc, Pleasanton, CA) after passing through a Gatan Tridium GIF (Gatan, Inc, Pleasanton, CA) energy filter. With this camera, at a nominal microscope magnification of 18,000 x the image pixel size corresponds to 1.20 nm in the sample. At nominal magnification of 27,500 x, the pixel size corresponds to 0.77 nm in the sample.

Acquisition of a 4 x 4 montage

A low magnification map was acquired at 180 X magnification to map the grid and find intact cytoskeletons in areas with good stain density. The grid location of each intact cytoskeleton was marked on the map and each was examined at 4000 X to 5600 X magnification to ensure that no parts of the disc were folded over. When ready to image a dose of 500 to 600 electrons per \AA^2 was applied to an area larger than the montage area, in order to set the stain.

The magnification was then set to 18,000 X, the GIF slit was inserted and both rough and fine eucentricity were refined, and autofocus was taken to achieve a defocus value of -0.5 μm and the slit was refined to re-center on the zero-loss peak. A low dose prescan montage 4 x4 was then set up in Serial to calibrate the image shifts in SerialEM and ensure the disc was centered in the montage area and no part would be excluded from the

final field of view.

A 4 x 4 montage tilt series was collecting automatically using SerialEM software. The montage tilt series was set up so that 80 montage images would be acquired as the stage was incrementally tilted from -60° to $+60^{\circ}$. The target intensity was from 5000 to 6000 $e/\text{\AA}^2$ for each image. The GIF was set up to automatically refine the zero loss peak at 30 minute intervals during tilt series acquisition.

Acquisition of a single axis cryo tilt series

A low magnification map was taken using SerialEM software at 180 X magnification. Intact cytoskeletons on areas with thin, vitreous ice were marked on the low mag and their stage positions were saved in the navigator file. SerialEM was used to place the microscope into low dose EFTEM mode. Each cytoskeleton was inspected at 5600 X magnification to determine if any part of the overlap zone was located over a 2 μm hole in the carbon support. If the cytoskeleton was correctly oriented over a hole a preview image with a dose of approximately $0.05 e/\text{\AA}^2$ was taken at 27,500 X magnification to ensure the cytoskeleton was in good condition and to see if gold fiducial particles were present on the area of interest.

Before taking a tilt series, SerialEM was used to refine both the rough and fine eucentricity; the defocus was adjusted to $-6 \mu\text{m}$ or $-4 \mu\text{m}$; and image settings were adjusted to that the dose for a record image was set to $1 e/\text{\AA}^2$. An area containing

sufficient features for tracking was defined along the tilt axis so that it was approximately 1 μm from the area to be imaged. The GIF was adjusted to refine the zero loss peak.

A tilt series was acquired automatically using SerialEM. The stage was tilted incrementally from -60° to $+60^\circ$. A record image was acquired and binned by 2 at every 2° of tilt. The dose for each projection image was varied as a function of $1/\cosine$ of the tilt angle, so that a maximum dose of $2 \text{ e}/\text{\AA}^2$ was used at the highest tilt angle and minimum dose of $1 \text{ e}/\text{\AA}^2$ was used at 0° tilt.

Reconstructions of tomograms using IMOD

Building a 4x4 montaged tomogram

The tilt stack was reconstructed computationally into a 3D volume using IMOD. The alignment of the overlapping sections of the montage was corrected automatically and then refined manually using Midas. Patch tracking was used to generate a fiducial model for image stack alignment. A manually defined boundary model, which mapped out the edges of the cytoskeleton, was used to exclude regions of empty formvar from tracking. Tracking of patches was carried out first using a global alignment and then a local alignment. Contours with alignment errors leading to very high residuals were deleted to achieve a better final alignment. After final alignment weighted back projection was used to compute a 3D volume. After 3D volume reconstruction, the volume was flattened computationally if necessary.

Building a cryo tomogram

After tilt series acquisition, a 3D tomogram was computationally reconstructed using IMOD. A fiducial model was seeded manually by placing points on the 0° tilt image at locations where a 10 nm gold fiducial particles were present. Gold particles were chosen on the bases that they did not overlap with other gold particles, were easy to distinguish from the background and as much as possible, were evenly distributed over the image. Contours were created by automatically tracking the gold particles through the image stacks. Points were added manually to fill any gaps. Alignment of the fiducials was computed and then fiducial points with large residual vectors (deviating from ideal) were examined and the positioning of the points was adjusted manually if it was valid to do so. Both global and local alignments were used to optimize final alignment as much as possible.

CTF correction

After the 3D volume was reconstructed the contrast transfer function was used to recover information where they contrast was inverted in the image. ETOMO was used to calculate the CFT correction using estimates of defocus values over small ranges of tilt angles. Calibrations from the F30 microscope, and the calculated changes in defocus for binned angles of tilt were used to computationally recover information where contrast was inverted where the CTF was less than 0.

Erasing gold

The final processing step was removing the gold fiducial particles from the upper and lower X,Y surface of the aligned stack to ensure that no high contrast ray artifacts were present that could obscure sample data. Gold particles were removed by automatically searching for and generating model particle positions within the tilt stack. The model was then manually corrected so that a point was placed in the center of every gold fiducial. The pixels around the central model point, out to a radius of 13 pixels, were then altered to have an average gray value. The final tomogram was computed using weighted back projection.

Modeling using IMOD

Modeling the ventral discs

IMOD was used to create models of the paths of the MTs and MRs in each ventral disc montage. Points were placed along the MRs (as these were more widely spaced and easier to follow) at regular intervals. Each MT/MR was modeled using a single open contour. The color of the contour was changed as the microtubule transitioned into a different disc region using the fine grain tool. The point of each regional transition was judged based on structural criteria and its position in the disc as a whole. The disc MT/MRs were modeled in order from the center edge to the outer periphery. It was possible to follow a single MT/MR as they do not overlap each other except in the dense bands proximal region. Here, every contour was extended to dense band closest to the

basal bodies so that a good estimate of total length could be made. The extended contours were input so that the approximate curvature of the preceding contour was maintained.

The boundaries of the dense bands were modeled using closed contours in a separate object. The distance between the MT ends on the DB was measured at various points so that: distance 1 = distance between DB1 and DB2; distance 2 = distance between DB2 and BD3; and distance 3 = half the distance between DB1 and DB3. An average of distances 1, 2 and 3 was calculated for each disc and subtracted from the length of each contour to get the best estimate of total length.

The boundary of the snMTs was modeled to show their relative position, a third object with closed contours. The contours were then divided at the fine grain boundaries using an IMOD program called “imodchopconts”. The program divided all the contours at each fine grain boundary and inserted all the contours of the same color into a separate object in a new model. The point at the boundary was duplicated so that the contours all start and end at their original position and their lengths were maintained accurately.

In order to assess curvature across the disc, contours of the main disc models were broken along the fine grain boundaries and moved to separate objects. The curvature for each contour and the total curvature of each region was then determined using IMOD.

Modeling for subvolume averaging

IMOD was used to generate a point to define the center of each subvolume. A separate

model of each surface of the overlap zone was generated using a single object with multiple open contours. Points were placed as close as possible to the center of the lumen of each MT, then offset to move the entire contour to the point of the MT/MR interface. Contours started and ended approximately 1 inch from the edge of the volume when viewed at 1X zoom, in X and Y. Any areas of poor definition or containing extraneous material were excluded. All of the contours were constructed with the same directionality. Once completed, the model was offset in the X, Z plane, by approximately 13 pixels, to move the model points to the area where the MT and MR connect.

The program, “AddModPts”, was then used to alter the spacing of the points in each contour. Points were moved or adding along the contour automatically to fit a defined spacing. An 11 pixel spacing was enforced to correspond to an 8nm α/β tubulin repeating unit.

Subvolume averaging using PEET

Generation of a preliminary averaged volume for each overlap zone surface in each tomogram

Sub-volume averaging was carried out in multiple stages to form the final disc region structures. First a preliminary alignment was carried out for each overlap zone surface in each individual tomogram. The tomogram .rec file, the model file, and the tilt log were inserted as the input data. The sub-volume size was defined as a 70x70x70 pixel volume, with a model point at the center. An initial reference was constructed from 32 randomly

selected sub-volumes. The alignment was set so that the directionality of the contour would be used to define the y-axis of each sub-volume. Three stages of alignment were used to iteratively converge on the average structure giving the highest cross correlations scores. After each round of alignment, a new reference was constructed to minimize reference bias. This motive list of rotations and translations for each subvolume was used as a starting alignment for the grand averages.

Production of a grand average volume from the overlap zones from multiple tomograms

After a final average structure was optimized for each surface from each tomogram, a grand average was built using subvolumes from multiple tomograms. The motive lists for each average generated previously were modified manually by rotating the averaged volumes into approximately the same orientation. This large rotation to the motive list was output after the average volume was constructed.

The motive list contains information on the translocation and angular rotations that were used for each sub-volume particle to achieve an alignment to the reference with the highest cross-correlation scores. The result was that each sub-volume could be automatically rotated before alignment refinement to ensure that all of the input sub-volumes, from different tomograms, were in approximately the same orientation. This reduced the required search angles and run time dramatically. Tomograms, models and motive lists from all previous averages were entered into a final PEET run for each surface. The settings are show in Figures 7.1 and Figure 7.2.

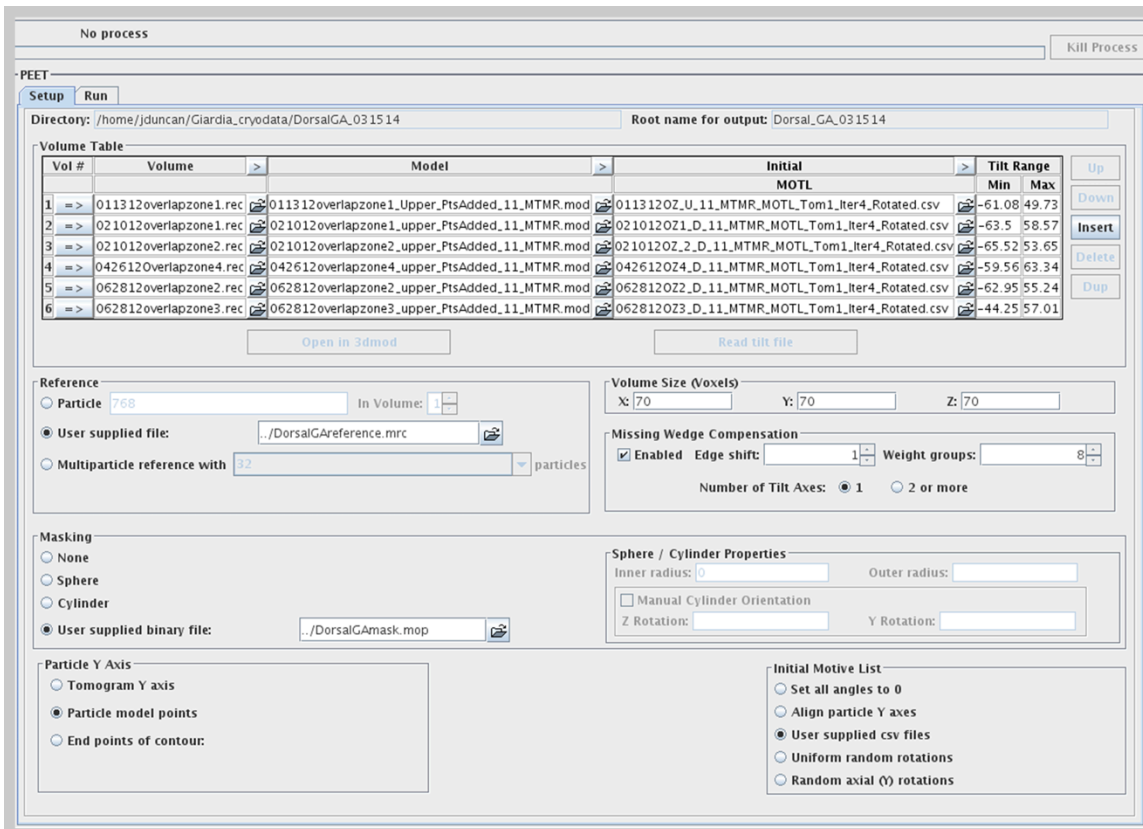


Figure 7.1: PEET setup tab used for the grand average run for each region. The settings used for averaging are shown.

A reference volume was generated from the average volume output with the highest resolution result. A mask was generated and used for all four averages of the ventral disc regions. Contours were placed around the structure in order to exclude areas containing neighboring MTs and noise alone. A mask was then generated using imodmop to color all areas outside of the contours black, thereby removing their contribution to the average.

No process Kill Process

Parallel Processing

Computer	# CPUs		Load Average		CPU Type	Speed GHz	RAM GB	Restarts	Finished Chunks	Failure Reason
	Used	Max.	1 Min.	5 Min.						
<input type="checkbox"/> bigfoot	0	6	0.0	0.0	Core i7	4.0	32			
<input type="checkbox"/> bear	0	8	0.55	0.37	5590	3.3	72			
<input type="checkbox"/> shrek	0	8	0.48	0.36	5590	3.3	48			
<input type="checkbox"/> tubule	0	12	0.25	0.42	5680	3.3	48			
<input type="checkbox"/> eclipse	0	12	0.04	0.2	5680	3.3	48			
<input type="checkbox"/> druid	0	4	0.0	0.02	Xeon	3.4	16			
<input type="checkbox"/> bebop	0	4	0.04	0.02	Core i5	3.3	16			
<input type="checkbox"/> sanguine	0	6	0.06	0.02	Core i7	3.2	12			
<input type="checkbox"/> mustang	0	8	0.21	0.42	5647	2.9	24			
<input type="checkbox"/> wanderer	0	4	0.84	0.78	5540	2.5	24			

CPU: 0 Restart Load Nice: 18 Pause Resume Save As Defaults

PEET

Setup Run

Iteration Table

Run #	Angular Search Range						Search Distance	Hi Freq		Ref Threshold	Duplicate	
	Phi		Theta		Psi			Filter			Shift	Angle
	Max	Step	Max	Step	Max	Step		Cutoff	Sigma			
1 =>	18.0	6.0	0.0	1.0	0.0	1.0	6	0.1	0.1	13390.0	1	1
2 =>	9.0	3.0	9.0	3.0	9.0	3.0	6	0.3	0.05	13390.0	1	1
3 =>	4.5	1.5	4.5	1.5	4.5	1.5	3	0.3	0.05	13390.0	1	1
4 =>	2.25	0.75	2.25	0.75	2.25	3.0	3	0.3	0.05	13390.0	1	1

Remove duplicate particles after each iteration

Spherical Sampling for Theta and Psi
 None Full sphere Half sphere Sample interval (degrees):

Number of Particles to Average
Start: Incr.: End: Additional numbers:

Use Equal Numbers of Particles from All Tomograms
 For average volumes For new references

Optional / Advanced Features

<input type="checkbox"/> Align averages to have their Y axes vertical	Particles per CPU: <input type="text" value="10"/>
<input checked="" type="checkbox"/> Use absolute value of cross-correlation	Debug level: <input type="text" value="3"/>
<input type="checkbox"/> Save individual aligned particles	Low frequency cutoff: <input type="text" value="0.0"/> Sigma: <input type="text" value="0.05"/>
<input checked="" type="checkbox"/> Strict search limit checking	Average only members of classes: <input type="text" value="6"/>
<input type="checkbox"/> No reference refinement	

Figure 7.2: PEET run tab used for the grand average run for each region. Table of angular and translational search ranges used at each iterative step in average construction. Below are additional settings used for subvolume averaging.

A rough averaged volume from a single tomogram with the highest resolution was used to generate a reference for each grand average. The length of each side of the reference volume was doubled to allow for translocations during alignment. A grand average alignment was produced for each region. An extra refinement step was added to ensure a higher quality result. Each average volume was mtf filtered to enhance the sharpness of the edges within the volume.

Calculating the internal resolution of the grand average volumes using Fourier shell correlation.

A program called calcFCS was used to calculate the internal resolution of the grandaverage. plotFSC was used to display the FSC curve for each consecutive average.

Production of the Binary Common Core Structure

In order to generate common core particle, a super average alignment was carried out. The average volumes from each regional grand average were input into PEET. An alignment without refinement run was carried out to align all the averaged volumes in the same orientation. Imoddenismatch was used to scale all the grayscale values so that the means and range of grayscale values was the same for all the average volumes. Matlab was used to determine a threshold value of 1σ below the mean. A binary value of 1 was applied to all voxels in the averaged volumes with a grayscale value below the threshold, producing a binary structure for each region. Matlab was then used to generate a list of

voxels for the binary common core structure. Voxels in all four binary volumes with a value of 1 were assigned a value of 1 in the binary common core structure. Voxels that were not present in all four binary structures were assigned a value of 0.

REFERENCES

1. Elmendorf HG, Dawson SC, McCaffery JM (2003) The cytoskeleton of *Giardia lamblia*. International journal for parasitology 33: 3-28.
2. Wolfe MS (1992) Giardiasis. Clinical microbiology reviews 5: 93-100.
3. Mank TG, Zaat JO (2001) Diagnostic advantages and therapeutic options for giardiasis. Expert opinion on investigational drugs 10: 1513-1519.
4. Dobell C (1960) Antony van Leeuwenhoek and his 'little animals'. New York: Dover Publications.
5. Lambl V (1859) Mikroskopische untersuchungen der Darm-Excrete: Beitrag zur Pathologie des Darms und zur Diagnostik am Krankenbette; vierjahrschrift fur die praktische Heilkunde. Med Fac Prague 1: 440-491.
6. (2002) Clinical Key Giardiasis Information. Elsevier
7. Staff MC (1998-2014) *Giardia* infection (giardiasis) Symptomes. Mayo Foundation for Medical Education and Research
8. Pettoello Mantovani M, Guandalini S, Ecuba P, Corvino C, di Martino L (1989) Lactose malabsorption in children with symptomatic *Giardia lamblia* infection: feasibility of yogurt supplementation. Journal of pediatric gastroenterology and nutrition 9: 295-300.
9. Moya-Camarena SY, Sotelo N, Valencia ME (2002) Effects of asymptomatic *Giardia intestinalis* infection on carbohydrate absorption in well-nourished Mexican children. The American journal of tropical medicine and hygiene 66: 255-259.
10. Vega-Franco L, Meza C, Romero JL, Alanis SE, Meijerink J (1987) Breath hydrogen test in children with giardiasis. Journal of pediatric gastroenterology and nutrition

- 6: 365-368.
11. Solomons NW (1982) Giardiasis: nutritional implications. *Reviews of infectious diseases* 4: 859-869.
 12. Cordingley FT, Crawford GP (1986) *Giardia* infection causes vitamin B12 deficiency. *Australian and New Zealand journal of medicine* 16: 78-79.
 13. Notis WN (1972) Giardiasis and vitamin B-12 malabsorption. *Gastroenterology* 63: 1085.
 14. Stark D, van Hal S, Marriott D, Ellis J, Harkness J (2007) Irritable bowel syndrome: a review on the role of intestinal protozoa and the importance of their detection and diagnosis. *International journal for parasitology* 37: 11-20.
 15. (2014) Centers for Disease Control and Prevention, Parasites - *Giardia*. CDC
 16. Johnston SP, Ballard MM, Beach MJ, Causer L, Wilkins PP (2003) Evaluation of three commercial assays for detection of *Giardia* and *Cryptosporidium* organisms in fecal specimens. *Journal of clinical microbiology* 41: 623-626.
 17. Robertson LJ, Hanevik K, Escobedo AA, Morch K, Langeland N (2010) Giardiasis-- why do the symptoms sometimes never stop? *Trends in parasitology* 26: 75-82.
 18. Gardner TB, Hill DR (2001) Treatment of giardiasis. *Clinical microbiology reviews* 14: 114-128.
 19. Danciger M, Lopez M (1975) Numbers of *Giardia* in the feces of infected children. *The American journal of tropical medicine and hygiene* 24: 237-242.
 20. Kappus KD, Lundgren RG, Jr., Juranek DD, Roberts JM, Spencer HC (1994) Intestinal parasitism in the United States: update on a continuing problem. *The American journal of tropical medicine and hygiene* 50: 705-713.

21. Parasites - *Giardia*, Epidemiology and Risk Factors. Center for Disease Control. pp. Epidemiology and Risk Factors with *Giardia* infection
22. Savioli L, Smith H, Thompson A (2006) *Giardia* and *Cryptosporidium* join the 'Neglected Diseases Initiative'. Trends in parasitology 22: 203-208.
23. Sousa MC, Goncalves CA, Bairos VA, Poiaraes-Da-Silva J (2001) Adherence of *Giardia lamblia* trophozoites to Int-407 human intestinal cells. Clinical and diagnostic laboratory immunology 8: 258-265.
24. Berkman DS, Lescano AG, Gilman RH, Lopez SL, Black MM (2002) Effects of stunting, diarrhoeal disease, and parasitic infection during infancy on cognition in late childhood: a follow-up study. Lancet 359: 564-571.
25. Lofmark S, Edlund C, Nord CE (2010) Metronidazole is still the drug of choice for treatment of anaerobic infections. Clinical infectious diseases: an official publication of the Infectious Diseases Society of America 50 Suppl 1: S16-23.
26. David Leitsch SS, Anita Burgess, Michael Duchene (2012) Nitroimidazole drugs vary in their mode of action in the human parasite *Giardia lamblia*. International Journal for parasitology: Drugs and drug resistance 2: 166-170.
27. (2006) Australian Medicines Handbook; Rossi S, editor: Royal Australian College of General Practitioners, Pharmaceutical Society of Australia, Australasian Society of Clinical and Experimental Pharmacologists and Toxicologists.
28. Sebelius K (2011) Report on Carcinogens. 12th Edition ed: US Department of Health and Human Services, National Toxicology Program.
29. Land KM, Johnson PJ (1999) Molecular basis of metronidazole resistance in pathogenic bacteria and protozoa. Drug resistance updates: reviews and

- commentaries in antimicrobial and anticancer chemotherapy 2: 289-294.
30. Solaymani-Mohammadi S, Genkinger JM, Loffredo CA, Singer SM (2010) A meta-analysis of the effectiveness of albendazole compared with metronidazole as treatments for infections with *Giardia duodenalis*. PLoS neglected tropical diseases 4: e682.
 31. Upcroft JA, Dunn LA, Wright JM, Benakli K, Upcroft P, et al. (2006) 5-Nitroimidazole drugs effective against metronidazole-resistant *Trichomonas vaginalis* and *Giardia duodenalis*. Antimicrobial agents and chemotherapy 50: 344-347.
 32. Upcroft JA, Campbell RW, Benakli K, Upcroft P, Vanelle P (1999) Efficacy of new 5-nitroimidazoles against metronidazole-susceptible and -resistant *Giardia*, *Trichomonas*, and *Entamoeba* spp. Antimicrobial agents and chemotherapy 43: 73-76.
 33. Plutzer J, Ongerth J, Karanis P (2010) *Giardia* taxonomy, phylogeny and epidemiology: Facts and open questions. International journal of hygiene and environmental health 213: 321-333.
 34. Cavalier-Smith T (2003) Protist phylogeny and the high-level classification of Protozoa. Europ J Protistol 39: 338-348.
 35. Adam RD (2001) Biology of *Giardia lamblia*. Clinical microbiology reviews 14: 447-475.
 36. Tovar J, Leon-Avila G, Sanchez LB, Sutak R, Tachezy J, et al. (2003) Mitochondrial remnant organelles of *Giardia* function in iron-sulphur protein maturation. Nature 426: 172-176.

37. Hashimoto T, Sanchez LB, Shirakura T, Muller M, Hasegawa M (1998) Secondary absence of mitochondria in *Giardia lamblia* and *Trichomonas vaginalis* revealed by valyl-tRNA synthetase phylogeny. Proceedings of the National Academy of Sciences of the United States of America 95: 6860-6865.
38. Roger AJ, Svard SG, Tovar J, Clark CG, Smith MW, et al. (1998) A mitochondrial-like chaperonin 60 gene in *Giardia lamblia*: evidence that diplomonads once harbored an endosymbiont related to the progenitor of mitochondria. Proceedings of the National Academy of Sciences of the United States of America 95: 229-234.
39. Dawson SC, Paredez AR (2013) Alternative cytoskeletal landscapes: cytoskeletal novelty and evolution in basal excavate protists. Current opinion in cell biology 25: 134-141.
40. Wittmann T, Hyman A, Desai A (2001) The spindle: a dynamic assembly of microtubules and motors. Nature cell biology 3: E28-34.
41. Kline-Smith SL, Walczak CE (2004) Mitotic spindle assembly and chromosome segregation: refocusing on microtubule dynamics. Molecular cell 15: 317-327.
42. Gatlin JC, Bloom K (2010) Microtubule motors in eukaryotic spindle assembly and maintenance. Seminars in cell & developmental biology 21: 248-254.
43. Nazarova E, O'Toole E, Kaitna S, Francois P, Winey M, et al. (2013) Distinct roles for antiparallel microtubule pairing and overlap during early spindle assembly. Molecular biology of the cell 24: 3238-3250.
44. McIntosh JR, O'Toole E, Zhudenkov K, Mophew M, Schwartz C, et al. (2013) Conserved and divergent features of kinetochores and spindle microtubule ends

- from five species. The Journal of cell biology 200: 459-474.
45. Poole CA, Jensen CG, Snyder JA, Gray CG, Hermanutz VL, et al. (1997) Confocal analysis of primary cilia structure and colocalization with the Golgi apparatus in chondrocytes and aortic smooth muscle cells. Cell biology international 21: 483-494.
 46. O'Toole ET, Giddings TH, Jr., Porter ME, Ostrowski LE (2012) Computer-assisted image analysis of human cilia and *Chlamydomonas* flagella reveals both similarities and differences in axoneme structure. Cytoskeleton 69: 577-590.
 47. Fisch C, Dupuis-Williams P (2011) [The rebirth of the ultrastructure of cilia and flagella]. Biologie aujourd'hui 205: 245-267.
 48. Fisch C, Dupuis-Williams P (2011) Ultrastructure of cilia and flagella - back to the future! Biology of the cell / under the auspices of the European Cell Biology Organization 103: 249-270.
 49. Letunic I, Bork P (2007) Interactive Tree Of Life (iTOL): an online tool for phylogenetic tree display and annotation. Bioinformatics 23: 127-128.
 50. Hampl V, Hug L, Leigh JW, Dacks JB, Lang BF, et al. (2009) Phylogenomic analyses support the monophyly of Excavata and resolve relationships among eukaryotic "supergroups". Proceedings of the National Academy of Sciences of the United States of America 106: 3859-3864.
 51. McIntosh JR, Ogata ES, Landis SC (1973) The axostyle of *Saccinobaculus*. I. Structure of the organism and its microtubule bundle. The Journal of cell biology 56: 304-323.
 52. McIntosh JR (1973) The axostyle of *Saccinobaculus*. II. Motion of the microtubule

- bundle and a structural comparison of straight and bent axostyles. *The Journal of cell biology* 56: 324-339.
53. de Andrade Rosa I, de Souza W, Benchimol M (2013) High-resolution scanning electron microscopy of the cytoskeleton of *Tritrichomonas foetus*. *Journal of structural biology* 183: 412-418.
54. Cheon SH, Kim SR, Song HO, Ahn MH, Ryu JS (2013) The dimension of *Trichomonas vaginalis* as measured by scanning electron microscopy. *The Korean journal of parasitology* 51: 243-246.
55. Mielewczik M, Mehlhorn H, Al-Quraishy S, Grabensteiner E, Hess M (2008) Transmission electron microscopic studies of stages of *Histomonas meleagridis* from clonal cultures. *Parasitology research* 103: 745-750.
56. Tamm SL (2008) Unsolved motility looking for answer. *Cell motility and the cytoskeleton* 65: 435-440.
57. Vedrenne C, Giroud C, Robinson DR, Besteiro S, Bosc C, et al. (2002) Two related subpellicular cytoskeleton-associated proteins in *Trypanosoma brucei* stabilize microtubules. *Molecular biology of the cell* 13: 1058-1070.
58. Daniels JP, Gull K, Wickstead B (2010) Cell biology of the trypanosome genome. *Microbiology and molecular biology reviews* : MMBR 74: 552-569.
59. Kohl L, Gull K (1998) Molecular architecture of the trypanosome cytoskeleton. *Molecular and biochemical parasitology* 93: 1-9.
60. Hoog JL, Bouchet-Marquis C, McIntosh JR, Hoenger A, Gull K (2012) Cryo-electron tomography and 3-D analysis of the intact flagellum in *Trypanosoma brucei*. *Journal of structural biology* 178: 189-198.

61. Holberton DV, Ward AP (1981) Isolation of the cytoskeleton from *Giardia*. Tubulin and a low-molecular-weight protein associated with microribbon structures. *Journal of cell science* 47: 139-166.
62. Holberton DV (1973) Fine structure of the ventral disk apparatus and the mechanism of attachment in the flagellate *Giardia muris*. *Journal of cell science* 13: 11-41.
63. Holberton DV (1981) Arrangement of subunits in microribbons from *Giardia*. *Journal of cell science* 47: 167-185.
64. Holberton DV (1973) Mechanism of attachment of *Giardia* to the wall of the small intestine. *Transactions of the Royal Society of Tropical Medicine and Hygiene* 67: 29-30.
65. Holberton DV (1974) Attachment of *Giardia*-a hydrodynamic model based on flagellar activity. *The Journal of experimental biology* 60: 207-221.
66. Nash TE, Herrington DA, Losonsky GA, Levine MM (1987) Experimental human infections with *Giardia lamblia*. *The Journal of infectious diseases* 156: 974-984.
67. Caccio SM, Ryan U (2008) Molecular epidemiology of giardiasis. *Molecular and biochemical parasitology* 160: 75-80.
68. Xu F, Jerlstrom-Hultqvist J, Andersson JO (2012) Genome-wide analyses of recombination suggest that *Giardia intestinalis* assemblages represent different species. *Molecular biology and evolution* 29: 2895-2898.
69. Franzen O, Jerlstrom-Hultqvist J, Castro E, Sherwood E, Ankarklev J, et al. (2009) Draft genome sequencing of *Giardia intestinalis* assemblage B isolate GS: is human giardiasis caused by two different species? *PLoS pathogens* 5: e1000560.
70. Morrison HG, McArthur AG, Gillin FD, Aley SB, Adam RD, et al. (2007) Genomic

- minimalism in the early diverging intestinal parasite *Giardia lamblia*. *Science* 317: 1921-1926.
71. Dujon B (1996) The yeast genome project: what did we learn? *Trends in genetics: TIG* 12: 263-270.
72. Lukjancenko O, Wassenaar TM, Ussery DW (2010) Comparison of 61 sequenced *Escherichia coli* genomes. *Microbial ecology* 60: 708-720.
73. Bernander R, Palm JE, Svard SG (2001) Genome ploidy in different stages of the *Giardia lamblia* life cycle. *Cellular microbiology* 3: 55-62.
74. Yu LZ, Birky CW, Jr., Adam RD (2002) The two nuclei of *Giardia* each have complete copies of the genome and are partitioned equationally at cytokinesis. *Eukaryotic cell* 1: 191-199.
75. Wieseahn GP, Jarroll EL, Lindmark DG, Meyer EA, Hallick LM (1984) *Giardia lamblia*: autoradiographic analysis of nuclear replication. *Experimental parasitology* 58: 94-100.
76. Tumova P, Kulda J, Nohynkova E (2007) Cell division of *Giardia intestinalis*: assembly and disassembly of the adhesive disc, and the cytokinesis. *Cell motility and the cytoskeleton* 64: 288-298.
77. Kabnick KS, Peattie DA (1990) In situ analyses reveal that the two nuclei of *Giardia lamblia* are equivalent. *Journal of cell science* 95 (Pt 3): 353-360.
78. Adam RD (1991) The biology of *Giardia* spp. *Microbiological reviews* 55: 706-732.
79. Boucher SE, Gillin FD (1990) Excystation of in vitro-derived *Giardia lamblia* cysts. *Infection and immunity* 58: 3516-3522.
80. House SA, Richter DJ, Pham JK, Dawson SC (2011) *Giardia* flagellar motility is not

- directly required to maintain attachment to surfaces. PLoS pathogens 7: e1002167.
81. Lindmark DG (1980) Energy metabolism of the anaerobic protozoon *Giardia lamblia*. Molecular and biochemical parasitology 1: 1-12.
 82. Brown DM, Upcroft JA, Edwards MR, Upcroft P (1998) Anaerobic bacterial metabolism in the ancient eukaryote *Giardia duodenalis*. International journal for parasitology 28: 149-164.
 83. Tachezy J, Sanchez LB, Muller M (2001) Mitochondrial type iron-sulfur cluster assembly in the amitochondriate eukaryotes *Trichomonas vaginalis* and *Giardia intestinalis*, as indicated by the phylogeny of IscS. Molecular biology and evolution 18: 1919-1928.
 84. Schwartz CL, Heumann JM, Dawson SC, Hoenger A (2012) A detailed, hierarchical study of *Giardia lamblia*'s ventral disc reveals novel microtubule-associated protein complexes. PloS one 7: e43783.
 85. Dawson SC, House SA (2010) Life with eight flagella: flagellar assembly and division in *Giardia*. Current opinion in microbiology 13: 480-490.
 86. Hoeng JC, Dawson SC, House SA, Sagolla MS, Pham JK, et al. (2008) High-resolution crystal structure and in vivo function of a kinesin-2 homologue in *Giardia intestinalis*. Molecular biology of the cell 19: 3124-3137.
 87. Szymanska K, Johnson CA (2012) The transition zone: an essential functional compartment of cilia. Cilia 1: 10.
 88. Lenaghan SC, Chen J, Zhang M (2013) Modeling and analysis of propulsion in the multiflagellated microorganism *Giardia lamblia*. Physical review E, Statistical,

- nonlinear, and soft matter physics 88: 012726.
89. Benchimol M, Piva B, Campanati L, de Souza W (2004) Visualization of the funis of *Giardia lamblia* by high-resolution field emission scanning electron microscopy-- new insights. *Journal of structural biology* 147: 102-115.
 90. Piva B, Benchimol M (2004) The median body of *Giardia lamblia*: an ultrastructural study. *Biology of the cell / under the auspices of the European Cell Biology Organization* 96: 735-746.
 91. Crossley R, Holberton DV (1983) Selective extraction with Sarkosyl and repolymerization in vitro of cytoskeleton proteins from *Giardia*. *Journal of cell science* 62: 419-438.
 92. Clark JT, Holberton DV (1988) Triton-labile antigens in flagella isolated from *Giardia lamblia*. *Parasitology research* 74: 415-423.
 93. Holberton D, Baker DA, Marshall J (1988) Segmented alpha-helical coiled-coil structure of the protein giardin from the *Giardia* cytoskeleton. *Journal of molecular biology* 204: 789-795.
 94. Crossley R, Holberton DV (1983) Characterization of proteins from the cytoskeleton of *Giardia lamblia*. *Journal of cell science* 59: 81-103.
 95. Crossley R, Holberton D (1985) Assembly of 2.5 nm filaments from giardin, a protein associated with cytoskeletal microtubules in *Giardia*. *Journal of cell science* 78: 205-231.
 96. Peattie DA, Alonso RA, Hein A, Caulfield JP (1989) Ultrastructural localization of giardins to the edges of disk microribbons of *Giarida lamblia* and the nucleotide and deduced protein sequence of alpha giardin. *The Journal of cell biology* 109:

- 2323-2335.
97. O'Toole ET, Winey M, McIntosh JR (1999) High-voltage electron tomography of spindle pole bodies and early mitotic spindles in the yeast *Saccharomyces cerevisiae*. *Molecular biology of the cell* 10: 2017-2031.
 98. Kizilyaprak C, Bittermann AG, Daraspe J, Humbel BM (2014) FIB-SEM tomography in biology. *Methods in molecular biology* 1117: 541-558.
 99. Villinger C, Gregorius H, Kranz C, Hohn K, Munzberg C, et al. (2012) FIB/SEM tomography with TEM-like resolution for 3D imaging of high-pressure frozen cells. *Histochemistry and cell biology* 138: 549-556.
 100. Gatan (2014) 3D Serial Block Face Scanning Electron Microscopy Imaging. Gatan.
 101. Terra LL, Campanati L, De Souza W (2010) Heterogeneity in the sensitivity of microtubules of *Giardia lamblia* to the herbicide oryzalin. *Parasitology research* 107: 47-54.
 102. Correa G, Benchimol M (2006) *Giardia lamblia* behavior under cytochalasins treatment. *Parasitology research* 98: 250-256.
 103. Nicastro D, Schwartz C, Pierson J, Gaudette R, Porter ME, et al. (2006) The molecular architecture of axonemes revealed by cryoelectron tomography. *Science* 313: 944-948.
 104. Sui H, Downing KH (2006) Molecular architecture of axonemal microtubule doublets revealed by cryo-electron tomography. *Nature* 442: 475-478.
 105. Nicastro D, Fu X, Heuser T, Tso A, Porter ME, et al. (2011) Cryo-electron tomography reveals conserved features of doublet microtubules in flagella. *Proceedings of the National Academy of Sciences of the United States of America*

- 108: E845-853.
106. Hansen WR, Fletcher DA (2008) Tonic shock induces detachment of *Giardia lamblia*. PLoS neglected tropical diseases 2: e169.
107. Inge PM, Edson CM, Farthing MJ (1988) Attachment of *Giardia lamblia* to rat intestinal epithelial cells. Gut 29: 795-801.
108. Gillin FD, Reiner DS (1982) Attachment of the flagellate *Giardia lamblia*: role of reducing agents, serum, temperature, and ionic composition. Molecular and cellular biology 2: 369-377.
109. Hansen WR, Tulyathan O, Dawson SC, Cande WZ, Fletcher DA (2006) *Giardia lamblia* attachment force is insensitive to surface treatments. Eukaryotic cell 5: 781-783.
110. Weiland ME, McArthur AG, Morrison HG, Sogin ML, Svard SG (2005) Annexin-like alpha giardins: a new cytoskeletal gene family in *Giardia lamblia*. International journal for parasitology 35: 617-626.
111. Weiland ME, Palm JE, Griffiths WJ, McCaffery JM, Svard SG (2003) Characterisation of alpha-1 giardin: an immunodominant *Giardia lamblia* annexin with glycosaminoglycan-binding activity. International journal for parasitology 33: 1341-1351.
112. Bauer B, Engelbrecht S, Bakker-Grunwald T, Scholze H (1999) Functional identification of alpha 1-giardin as an annexin of *Giardia lamblia*. FEMS microbiology letters 173: 147-153.
113. Peattie DA (1990) The giardins of *Giardia lamblia*: genes and proteins with promise. Parasitology today 6: 52-56.

114. Palm JE, Weiland ME, Griffiths WJ, Ljungstrom I, Svard SG (2003) Identification of immunoreactive proteins during acute human giardiasis. *The Journal of infectious diseases* 187: 1849-1859.
115. Nohria A, Alonso RA, Peattie DA (1992) Identification and characterization of gamma-giardin and the gamma-giardin gene from *Giardia lamblia*. *Molecular and biochemical parasitology* 56: 27-37.
116. Ellis JGt, Davila M, Chakrabarti R (2003) Potential involvement of extracellular signal-regulated kinase 1 and 2 in encystation of a primitive eukaryote, *Giardia lamblia*. Stage-specific activation and intracellular localization. *The Journal of biological chemistry* 278: 1936-1945.
117. Davids BJ, Williams S, Lauwaet T, Palanca T, Gillin FD (2008) *Giardia lamblia* aurora kinase: a regulator of mitosis in a binucleate parasite. *International journal for parasitology* 38: 353-369.
118. Lauwaet T, Smith AJ, Reiner DS, Romijn EP, Wong CC, et al. (2011) Mining the *Giardia* genome and proteome for conserved and unique basal body proteins. *International journal for parasitology* 41: 1079-1092.
119. Moniz L, Dutt P, Haider N, Stambolic V (2011) Nek family of kinases in cell cycle, checkpoint control and cancer. *Cell division* 6: 18.
120. Roskoski R, Jr. (2012) ERK1/2 MAP kinases: structure, function, and regulation. *Pharmacological research: the official journal of the Italian Pharmacological Society* 66: 105-143.
121. Hagen KD, Hirakawa MP, House SA, Schwartz CL, Pham JK, et al. (2011) Novel structural components of the ventral disc and lateral crest in *Giardia intestinalis*.

- PLoS neglected tropical diseases 5: e1442.
122. Liang X, Peng L, Baek CH, Katzen F (2013) Single step BP/LR combined Gateway reactions. *BioTechniques* 55: 265-268.
 123. Woessner DJ, Dawson SC (2012) The *Giardia* median body protein is a ventral disc protein that is critical for maintaining a domed disc conformation during attachment. *Eukaryotic cell* 11: 292-301.
 124. Clark JT, Holberton DV (1986) Plasma membrane isolated from *Giardia lamblia*: identification of membrane proteins. *European journal of cell biology* 42: 200-206.
 125. Crossley R, Marshall J, Clark JT, Holberton DV (1986) Immunocytochemical differentiation of microtubules in the cytoskeleton of *Giardia lamblia* using monoclonal antibodies to alpha-tubulin and polyclonal antibodies to associated low molecular weight proteins. *Journal of cell science* 80: 233-252.
 126. Baker DA, Holberton DV, Marshall J (1988) Sequence of a giardin subunit cDNA from *Giardia lamblia*. *Nucleic acids research* 16: 7177.
 127. John J. Bozzola LDR (1999) *Electron Microscopy: Principles and Techniques for Biologists*: Jones & Bartlett Learning.
 128. de Bruijn WC, Sorber CW, Gelsema ES, Beckers AL, Jongkind JF (1993) Energy-filtering transmission electron microscopy of biological specimens. *Scanning microscopy* 7: 693-708; discussion 709.
 129. B. WD (1996) *Transmission Electron Microscopy: A Textbook for Material Science*: Kluwer Academic/ Plenum Publishers
 130. P.A. TPJM (2002) *An introduction to energy-filtered transmission electron*

- microscopy. *Topics in Catalysis* 21.
131. Marco S, Boudier T, Messaoudi C, Rigaud JL (2004) Electron tomography of biological samples. *Biochemistry Biokhimiia* 69: 1219-1225.
 132. Faruqi AR, Subramaniam S (2000) CCD detectors in high-resolution biological electron microscopy. *Quarterly reviews of biophysics* 33: 1-27.
 133. Koster AJ, Grimm R, Typke D, Hegerl R, Stoschek A, et al. (1997) Perspectives of molecular and cellular electron tomography. *Journal of structural biology* 120: 276-308.
 134. (2014) Gatan pre-announces advanced 2nd generation direct detection camera. Gatan.
 135. Yahav T, Maimon T, Grossman E, Dahan I, Medalia O (2011) Cryo-electron tomography: gaining insight into cellular processes by structural approaches. *Current opinion in structural biology* 21: 670-677.
 136. Lucic V, Forster F, Baumeister W (2005) Structural studies by electron tomography: from cells to molecules. *Annual review of biochemistry* 74: 833-865.
 137. Lengyel JS, Milne JL, Subramaniam S (2008) Electron tomography in nanoparticle imaging and analysis. *Nanomedicine* 3: 125-131.
 138. McIntosh R, Nicastro D, Mastronarde D (2005) New views of cells in 3D: an introduction to electron tomography. *Trends in cell biology* 15: 43-51.
 139. Mastronarde DN (2005) Automated electron microscope tomography using robust prediction of specimen movements. *Journal of structural biology* 152: 36-51.
 140. Frank J (1992) *Electron Tomography: Three Dimensional Imaging with the Transmission Electron Microscope*: Plenum Press.

141. Fessler J (2009) Analytical Tomographic Image Reconstruction Methods.
web.eecs.umich.edu/~fessler/course/516/l/c-tomo.pdf
142. Radermacher M (2009) Electron Tomography; Frank J, editor. New York Springer
[Link](#)
143. Briegel A, Pilhofer M, Mastronarde DN, Jensen GJ (2013) The challenge of determining handedness in electron tomography and the use of DNA origami gold nanoparticle helices as molecular standards. *Journal of structural biology* 183: 95-98.
144. Gan L, Jensen GJ (2012) Electron tomography of cells. *Quarterly reviews of biophysics* 45: 27-56.
145. Briegel A, Li X, Bilwes AM, Hughes KT, Jensen GJ, et al. (2012) Bacterial chemoreceptor arrays are hexagonally packed trimers of receptor dimers networked by rings of kinase and coupling proteins. *Proceedings of the National Academy of Sciences of the United States of America* 109: 3766-3771.
146. Bartesaghi A, Lecumberry F, Sapiro G, Subramaniam S (2012) Protein secondary structure determination by constrained single-particle cryo-electron tomography. *Structure* 20: 2003-2013.
147. Lawrence A, Bouwer JC, Perkins G, Ellisman MH (2006) Transform-based backprojection for volume reconstruction of large format electron microscope tilt series. *Journal of structural biology* 154: 144-167.
148. L. Reimer HK (2008) Transmission Electron Microscopy In: Rhodes WT, editor. *Physics of Image Formation*. 5th ed: Springer Science+Business Media, LLC.
149. Sorzano CO, Jonic S, Cottevaille M, Larquet E, Boisset N, et al. (2007) 3D electron

- microscopy of biological nanomachines: principles and applications. European biophysics journal : EBJ 36: 995-1013.
150. Frank J, Radermacher M, Penczek P, Zhu J, Li Y, et al. (1996) SPIDER and WEB: processing and visualization of images in 3D electron microscopy and related fields. *Journal of structural biology* 116: 190-199.
 151. J Frank PP (1995) On the correction of the contrast transfer function in biological electron microscopy. *Optik* 98: 125-129.
 152. Frank J (2006) Three-dimensional electron microscopy of macromolecular assemblies: visualization of biological molecules in their native state. . New York: Oxford University Press.
 153. Xiong Q, Morphew MK, Schwartz CL, Hoenger AH, Mastronarde DN (2009) CTF determination and correction for low dose tomographic tilt series. *Journal of structural biology* 168: 378-387.
 154. Briggs JA (2013) Structural biology in situ--the potential of subtomogram averaging. *Current opinion in structural biology* 23: 261-267.
 155. Cope J, Heumann J, Hoenger A (2011) Cryo-electron tomography for structural characterization of macromolecular complexes. *Current protocols in protein science / editorial board, John E Coligan [et al] Chapter 17: Unit17 13.*
 156. Bartesaghi A, Sprechmann P, Liu J, Randall G, Sapiro G, et al. (2008) Classification and 3D averaging with missing wedge correction in biological electron tomography. *Journal of structural biology* 162: 436-450.
 157. Winkler H, Zhu P, Liu J, Ye F, Roux KH, et al. (2009) Tomographic subvolume alignment and subvolume classification applied to myosin V and SIV envelope

- spikes. *Journal of structural biology* 165: 64-77.
158. Marshall J, Holberton DV (1993) Sequence and structure of a new coiled coil protein from a microtubule bundle in *Giardia*. *Journal of molecular biology* 231: 521-530.
159. Hoppe W (1974) Towards three-dimensional "electron microscopy" at atomic resolution. *Die Naturwissenschaften* 61: 239-249.
160. Phan S, Lawrence A, Molina T, Lanman J, Berlanga M, et al. (2012) TxBR montage reconstruction for large field electron tomography. *Journal of structural biology* 180: 154-164.
161. Phan S, Terada M, Lawrence A (2009) Serial reconstruction and montaging from large-field electron microscope tomograms. Conference proceedings : Annual International Conference of the IEEE Engineering in Medicine and Biology Society IEEE Engineering in Medicine and Biology Society Conference 2009: 5772-5776.
162. Gillin FD, Reiner DS, McCaffery JM (1996) Cell biology of the primitive eukaryote *Giardia lamblia*. *Annual review of microbiology* 50: 679-705.
163. Dye RB, Fink SP, Williams RC, Jr. (1993) Taxol-induced flexibility of microtubules and its reversal by MAP-2 and Tau. *The Journal of biological chemistry* 268: 6847-6850.
164. McIntosh JR (1974) Bridges between microtubules. *The Journal of cell biology* 61: 166-187.
165. van Heel M, Schatz M (2005) Fourier shell correlation threshold criteria. *Journal of structural biology* 151: 250-262.

166. van Heel M, Harauz G (1988) Biological macromolecules explored by pattern recognition. Scanning microscopy Supplement 2: 295-301.
167. Frank J (2006) Three-Dimensional Electron Microscopy of Macromolecular Assemblies: Visualization of Biological Molecules in Their Native State: Oxford University Press.
168. P. Draber ED (2012) Microtubules. In: Kavallaris M, editor. Cytoskeleton and Human Disease: Springer Science+Business Media LLC.
169. Nogales E, Wolf SG, Downing KH (1998) Structure of the alpha beta tubulin dimer by electron crystallography. Nature 391: 199-203.
170. Borisy GG, Taylor EW (1967) The mechanism of action of colchicine. Binding of colchicine-3H to cellular protein. The Journal of cell biology 34: 525-533.
171. Borisy GG, Taylor EW (1967) The mechanism of action of colchicine. Colchicine binding to sea urchin eggs and the mitotic apparatus. The Journal of cell biology 34: 535-548.
172. Jenkins MC, O'Brien CN, Murphy C, Schwarz R, Miska K, et al. (2009) Antibodies to the ventral disc protein delta-giardin prevent in vitro binding of *Giardia lamblia* trophozoites. The Journal of parasitology 95: 895-899.
173. Weisbrich A, Honnappa S, Jaussi R, Okhrimenko O, Frey D, et al. (2007) Structure-function relationship of CAP-Gly domains. Nature structural & molecular biology 14: 959-967.
174. Bosson A, Soleilhac JM, Valiron O, Job D, Andrieux A, et al. (2012) Cap-Gly proteins at microtubule plus ends: is EB1 detyrosination involved? PloS one 7: e33490.

175. Gerke V, Moss SE (2002) Annexins: from structure to function. *Physiological reviews* 82: 331-371.
176. Jernigan KK, Bordenstein SR (2014) Ankyrin domains across the Tree of Life. *PeerJ* 2: e264.
177. Mosavi LK, Cammett TJ, Desrosiers DC, Peng ZY (2004) The ankyrin repeat as molecular architecture for protein recognition. *Protein science: a publication of the Protein Society* 13: 1435-1448.
178. Contreras-Moreira B, Bates PA (2002) Domain fishing: a first step in protein comparative modelling. *Bioinformatics* 18: 1141-1142.
179. Bates PA, Sternberg MJ (1999) Model building by comparison at CASP3: using expert knowledge and computer automation. *Proteins Suppl* 3: 47-54.
180. Bates PA, Kelley LA, MacCallum RM, Sternberg MJ (2001) Enhancement of protein modeling by human intervention in applying the automatic programs 3D-JIGSAW and 3D-PSSM. *Proteins Suppl* 5: 39-46.
181. Gonzalez MA, Cope J, Rank KC, Chen CJ, Tittmann P, et al. (2013) Common mechanistic themes for the powerstroke of kinesin-14 motors. *Journal of structural biology* 184: 335-344.
182. Cope J, Rank KC, Gilbert SP, Rayment I, Hoenger A (2013) Kar3Vik1 uses a minus-end directed powerstroke for movement along microtubules. *PloS one* 8: e53792.